DEFORMATION MICROSTRUCTURES, MECHANISMS, AND HISTORY OF A SHEAR ZONE WITHIN THE CHUGACH ACCRETIONARY COMPLEX IN THE NELCHINA AREA, SOUTH-CENTRAL ALASKA

By

Veselina T. Yakimova, B.S.

A Thesis Submitted in Partial Fulfillment of the Requirements

for the Degree of

Master of Science

in

Geology

University of Alaska Fairbanks

May 2020

APPROVED:

Elisabeth Nadin, Committee Chair
Jochen Mezger, Committee Member
Sean Regan, Committee Member
Paul McCarthy, Chair
Department of Geosciences
Kinchel C. Doerner, Dean
College of Natural Science and Mathematics
Michael Castellini, Dean
UAF Graduate School

Abstract

Ductile-to-brittle fault zones reveal mineralogical processes that are thought to be responsible for the mechanical behavior of faults. I examined a pervasively deformed zone within the Jurassic to Cretaceous accretionary complex of southern Alaska that preserves hydrothermal alteration, dissolution precipitation, carbonaceous material (CM), clay minerals, and intracrystalline plasticity, all of which influence the strength of a fault. I characterized microstructures by SEM and EBSD, determined compositions by XRD, XRF, and Raman spectroscopy for one carbon-rich sample, and dated whole rock, rotated K-feldspar, and metamorphic muscovite by $^{40}Ar/^{39}Ar$ thermochronology to constrain the timing and conditions of accretion, uplift, and deformation recorded by this fault zone.

I interpret the specific mineralogy and complex network of deformation microstructures as a result of multiple deformation events. Highest-temperature deformation recorded within the shear zone is lower greenschist facies (400–450°C). Quartz-rich clasts preserve deformation lamellae, grain bulges, sweeping undulose extinction, pressure solution, and brittle fractures characteristic of low grade (300–400°C) at the brittle–ductile transition. Brittle overprint is expressed by fractures cross-cutting the stretched quartz phacoids, and black fault rock that has entrained stretched quartz grains. Raman spectroscopy places precipitation of the CM at ~300°C. I therefore associate the fault-rock fabrics with progressive down-temperature deformation as the fault was exhumed. I suggest that pressure solution and mineral alteration in all fault-zone samples, as well as quartz and phyllosilicate preferred orientation in a subset of the samples, indicate aseismic slip. Growth of clay and precipitation of CM reduced the friction coefficient, lowering the frictional strength and influencing the dynamic behavior of this fault zone. Constraining the relative timing of the different slip behaviors is hard to determine. It is possible

they were active at the same time, especially with the increase of width and complexity at the deeper part of the fault. What is preferentially preserved in the rock record is the latest stage of slip. Pseudotachylite structures generated during earthquakes, however, are rarely preserved due to their susceptibility to alteration. In my field area, consequent exhumation and cooling lead to progressive down-temperature brittle deformation and strong hydrothermal alteration, which could have eradicated any evidence for frictional melting.

Using $^{40}Ar/^{39}Ar$ thermochronometry alongside regional and local age constraints, I was able to provide some insight on timing of fault-zone and local tectonic activity. The fault lies between the McHugh Complex and Valdez Group, the two main components of the Jurassic to Cretaceous Chugach accretionary prism whose development and disruption is still debated. I interpret that fault activity lasted from ca. 120 Ma to ca. 60 Ma., and was followed by two stages of accelerated uplift and cooling during ca. 40 Ma and ca. 20 Ma. The cease of major fault activity after ca. 60 Ma, the lack of pervasive strike-slip motion indicators, and the presence of undeformed Eocene dikes as well as Eocene sediments deposited on top of both the McHugh Complex and Valdez Group, suggest they were deposited in proximity and were in place in Southern Alaska at the start of the Eocene epoch.

Table of Contents

Page

List of Figures

Page

List of Tables

Page

Acknowledgements

I would like to express my sincere gratitude to my advisor Elisabeth Nadin for the continuous support of my Master's study, related research and professional growth, for her patience, motivation and invaluable knowledge. I would also like to thank my committee members: Jochen Mezger, Sean Regan, and Catherine Hanks, for offering their time, support, guidance and good will throughout the extent of this project. The work presented here was supported by grants from the Geological Society of America, the Alaska Geological Society, and the University of Alaska Fairbanks. Meekin's Air Service flew us to the remote field area. Help in the field from Alan Rodriguez, John Barefoot and Seth Hooper is gratefully acknowledged. I thank Tom Trainor, Ken Severin, and all the staff at UAF's Advanced Instrumentation Laboratory for help in acquiring and interpreting XRD and XRF data. I also thank Elena Miranda and Lonnie Hufford who guided me in acquiring and interpreting the EBSD data, Jonathan Caine for acquiring the Raman data, and Laura Webb for acquiring and helping with interpretation of the $^{40}Ar/^{39}Ar$ thermochronometry data. Discussions with Sarah Roeke, Tim Little, Sue Karl, and Gar Pessel greatly contributed to my understanding of the general geologic background.

Chapter 1: Introduction

Microstructures of brittle and brittle-to-ductile fault zones reveal mineralogical processes that are thought to be responsible for the mechanical behavior of faults. My study focuses on a pervasively cataclasized zone within the Jurassic to Cretaceous accretionary complex of southern Alaska. The ~200m-wide zone preserves evidence of dissolution precipitation, carbonatization, clay mineral growth, intracrystalline plasticity, and pervasive hydrothermal alteration, all of which influence the strength of a fault. I describe the microstructural development of this fault, as well as the geochemistry and an array of $^{40}Ar/^{39}Ar$ dates of different parts of the fault zone, and synthesize a history of the immediate region based on my field and structural observations and regional constraints.

The fault I analyzed is located within the Jurassic–Cretaceous Chugach accretionary prism, at the boundary between the shallow-water mélange portion known as the McHugh Complex and the deep-water flysch section known as the Valdez Group (Figure 1). The fault is located near the Nelchina Glacier, and in this location, it appears on the state geological map (Wilson et al., 2015) as the Glacier Creek strand of the Border Ranges fault system. However, a recent mapping and petrological study (Barefoot et al., 2020) indicates that the Border Ranges fault was mismapped in this particular location (after MacKevett and Plafker, 1974; Pessel et al., 1981; Burns et al., 1991). My mapping and structural analyses suggest the fault I studied is the eastward continuation of the Eagle River thrust, which forms the contact between the McHugh and Valdez sections of the Chugach terrane west of the study area (Figure 1; Pavlis, 1982; Little and Naeser, 1989; Winkler, 1992). I refer to it here as the Eagle River fault (ERF). This study documents and characterizes the fabrics and microstructures within this section of the exhumed ERF, and contrasts them to the fabrics of the neighboring McHugh Complex and Valdez Group

exposures (Figure 2), to examine the nature of the McHugh–Valdez contact near the Nelchina Glacier. I offer a structural and temporal evolution of fault-zone rocks and provide insights into how their petrography, mineralogy, and chemistry controlled the slip properties of the fault.

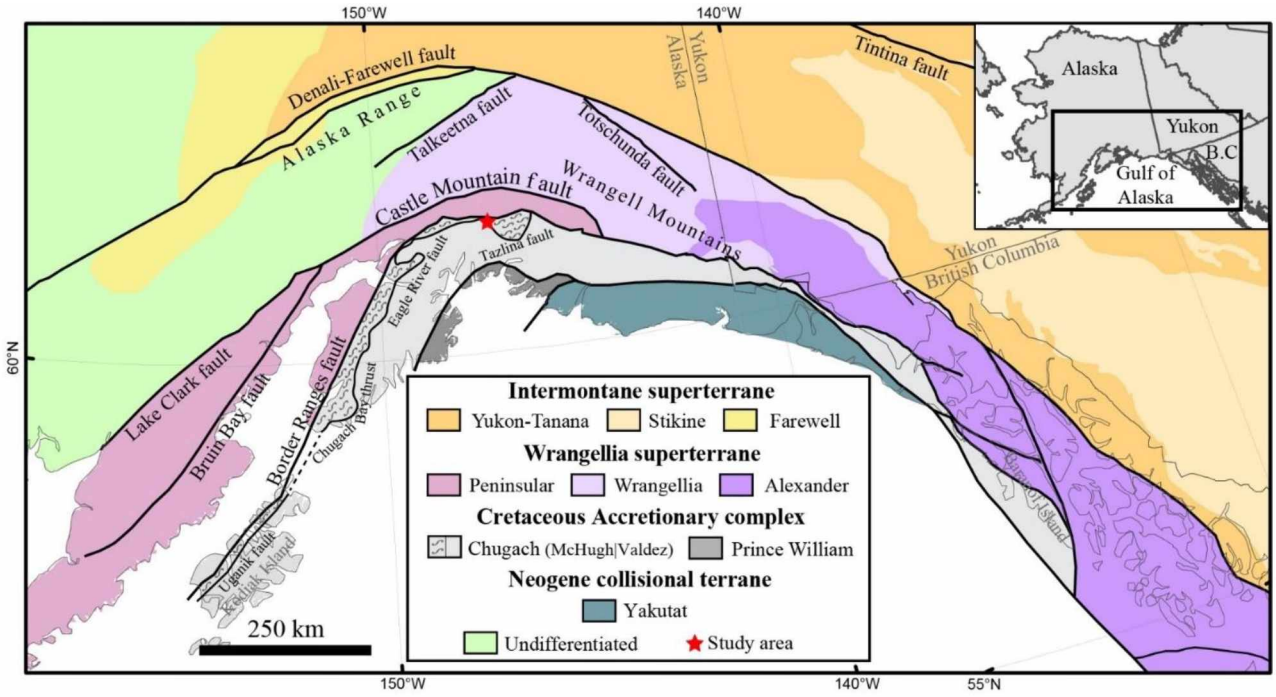

***Figure 1**: Regional map showing the general terrane configuration of south-central Alaska. The location of the Eagle River fault and its along-strike equivalents is from Kusky et al. (1997). Modified from Goldfarb et al. (2013).*

The field site provides an opportunity to study the rock record of fault behavior at brittle-ductile transition conditions that can only be observed at Earth's surface after exhumation. Features formed during earthquake rupture under these stress conditions used to be associated with the presence of pseudotachylite (Cowan, 1999), however, preservation of pseudotachylite in the rock record is extremely limited due to its susceptibility to erosion and alteration. New studies (e.g., Rowe and Griffith, 2015) expanded the list of rock features indicating seismic slip to include injection veins and clasts, mirror fault surfaces, amorphous silica and carbon aggregates, pulverized material, shock lamellae in quartz, branching fractures, and microfractures in crystals. I observe and document some of these features – pulverization and propagating thin carbonaceous veins—in the ERF at my field site. In experimental studies,

carbonaceous materials have a very low friction coefficient and are an important material controlling the frictional strength and rupture of fault zones (eg., Oohashi et al., 2011; Rutter et al., 2013; Nakamura et al., 2015). At the same time, pressure solution and mineral alteration, which are found in all fault-zone samples at my field site, as well as quartz and phyllosilicate preferred orientation in a subset of the samples, indicate primarily aseismic deformation during interseismic periods (Labaume et al., 2004; Janssen et al., 2014; Janssen et al., 2016). However, the 120-m width of shattered rock across the damage zone attests to intermittent seismic slip. Seismic slip occurs at the instant of an earthquake, while aseismic slip is the steady creep along the fault plane, varying from continuous to episodic with a single creep event lasting minutes to days (Bakun et al., 1986). A notable example of fault creep is at the San Andreas Fault Observatory at Depth (SAFOD), where drilling into the creeping section of the San Andreas fault provided a wealth of new information about the mineralogical features produced by such fault movement (e.g., Solum and Van Der Pluijm, 2004; Schleicher et al., 2009; Janssen et al., 2012). I refer to SAFOD gouge studies that describe rocks with similar microstructures and composition as those from the ERF (Holdsworth et al., 2011; Janssen et al., 2012; Janssen et al., 2014; Janssen et al., 2016). By studying this assemblage of microstructures, we gain a deeper understanding of the processes influencing the geomechanical behavior and strength evolution of exhumed faults in subduction zones, where the highest-magnitude earthquakes typically occur.

In addition to insights into rock strength in a subduction zone fault, I will discuss the phases of fault-zone evolution and tectonic events recorded in material dated by $^{40}Ar/^{39}Ar$. Variability observed within the range of dates from the $^{40}Ar/^{39}Ar$ plateaus attests to multiple phases of deformation in the region.

In order to constrain the timing and nature of deformation within this major subduction complex, this study combines field work, optical and electron microscopy and geochemical and

geochronological analyses of the ERF and adjacent rocks. Microstructures were characterized by petrographic microscope, scanning electron microscope (SEM), and electron back-scatter diffraction (EBSD) to determine the crystallographic orientation of quartz. Compositions of most rocks were determined by X-ray diffraction (XRD), X-ray fluorescence (XRF), energy dispersive X-ray spectroscopy (EDS), and for one carbon-rich sample by Raman spectroscopy. $^{40}Ar/^{39}Ar$ thermochronology on powdered whole-rock, stretched and rotated K-feldspar, and metamorphic muscovite constrains the age of faulting, as well as the episodes of accretion, uplift, and deformation in southern Alaska.

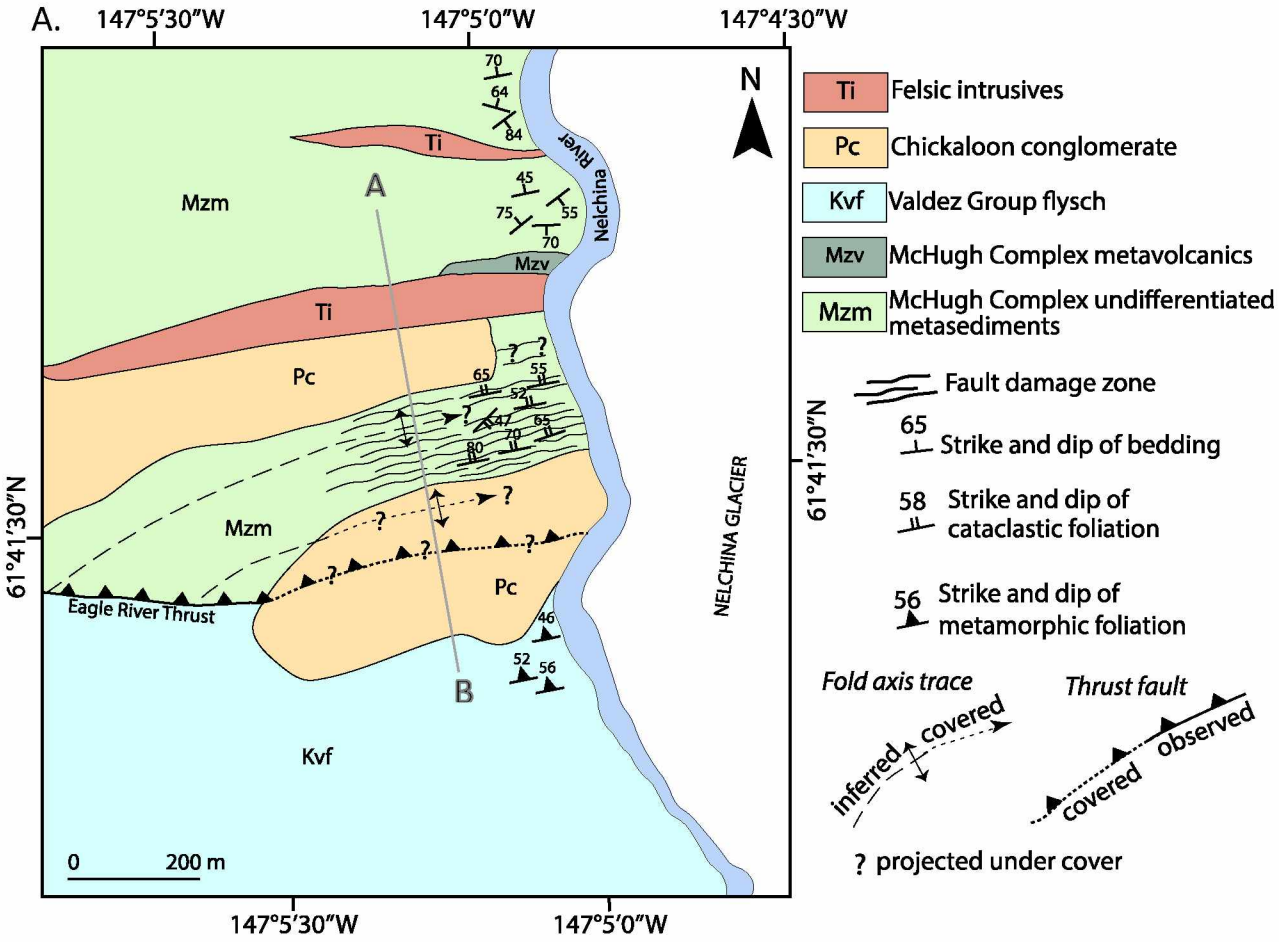

***Figure 2**: (A) Bedrock map of the Nelchina area showing the extent of the units and structural features outlined in the study. The western half of the map is adopted from Little (1992). Modified from an outcrop exposure map of Barefoot et al. (2020).*

B.

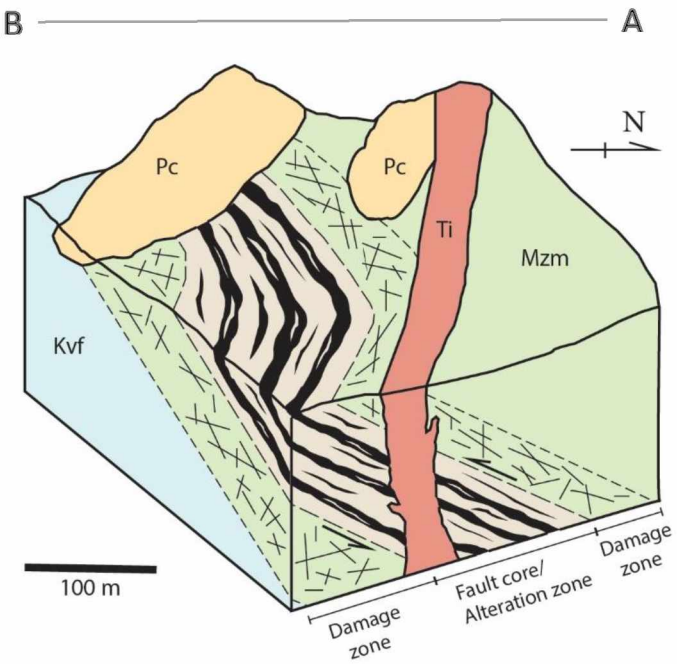

Figure 2 (continued): *(B) Block cross section across the fault zone from A to B.*

Chapter 2: Geologic Setting

Alaska consists of a complex collage of exhumed sedimentary basins, accreted terranes, magmatic belts, and subduction-complex strata that were added to the ancient western North American continental margin during Mesozoic and Cenozoic time (e.g., Jones et al., 1987; Nokleberg et al., 1994). Three composite terranes make up most of south-central Alaska: the Intermontane superterrane, the Wrangellia superterrane and the Cretaceous Accretionary Complex (Figure 1). The Wrangellia superterrane, which stretches discontinuously from western Alaska to southern British Columbia, consists of the allochthonous Peninsular, Alexander, and Wrangelia terranes. (Plafker and Berg, 1994; Nokleberg et al., 1994). Of relevance to this study are the Peninsular and Chugach terrane, which formed a subduction-accretionary complex in the late Mesozoic. The Peninsular terrane is synonymous with the Talkeetna arc, a Jurassic intra-oceanic island arc that was accreted to southern Alaska during Late Jurassic time (e.g., Roeske et al., 1989; Rioux et al., 2007). The Chugach terrane to the south developed during Jurassic to Cretaceous time as trench-fill, trench-slope, and ocean-basin deposits (MacKevett and Plafker, 1974; Plafker et al. 1994). The contact between the Chugach and Peninsular terranes is marked by the Border Ranges Fault (BRF; Figure 1). MacKevett and Plafker (1974) identified it as a plate boundary thrust contact that was heavily overprinted by mid-Eocene dextral slip (Pavlis, 1982). Burns et al. (1991) suggested BRF strands cut both terranes latitudinally within a 5-10 km wide zone, forming the BRF System (BRFS). The BRFS can be summarized as a complex ductile to brittle, thrust to dextral-slip system (Plafker et al., 1994; Pavlis and Roeske, 2007).

In my field site, the major rock units include: an olistostromal mélange, a fault zone deforming mélange rocks and a flysch unit to the south of the fault zone (Figure 2). The fault zone is the focus of this study. It represents the boundary between the two main components of

the Chugach terrane, the McHugh Complex and the Valdez Group. Just south of the Talkeetna Arc, the BRF is the subduction megathrust contact with the Jurassic McHugh Complex, a mélange of variably metamorphosed trench-slope sediments and volcaniclastics laced with a complex network of low- to moderate-angle faults (Kusky and Bradley, 1999; Amato and Pavlis, 2010; Labrado et al., 2015; Karl et al., 2015). South of the McHugh Complex lies the vast Cretaceous to Paleocene Valdez Group flysch, which has different proposed origins (Cowan, 2003; Pavlis and Roeske, 2007; Amato and Pavlis, 2010). Alluvial-fan sediments of the Eocene Chickaloon Formation (depositional age range ~60-40 Ma) sit astride both McHugh and Valdez exposures in the study area and elsewhere in southern Alaska (Little and Naeser, 1989). Finally, undeformed felsic dikes (ca. 55 Ma) crosscut both assemblages in the area (Little, 1988; Little and Naeser, 1989; Barefoot et al., 2020). They are thought to be part of the Sanak-Baranof suite of subducting ridge-related near-trench melts which migrated eastward during Paleocene to Eocene time (Bradley et al. 1993, Bradley et al. 2000).

One of the outstanding questions of southern Alaska geology is whether or not the entire package of the Chugach terrane was deposited in its current configuration. The shallow-water mélange section (the McHugh Complex) was likely deposited adjacent to the Talkeetna Arc/continental margin during Late Jurassic to Early Cretaceous time (e.g. Bradley and Kusky, 1992; Amato and Pavlis, 2010; Barefoot et al., 2020). In contrast, several studies suggest that the deep-marine turbidites of the Valdez Group were deposited adjacent to the Coast Plutonic Complex in British Columbia (e.g. Cowan, 2003; Pavlis and Roeske, 2007; Amato et al., 2013; Garver and Davidson, 2015). In order to bring the Valdez Group alongside the McHugh Complex, significant lateral displacement should have occurred between the two. Thus, mapping faults between these sections of the accretionary prism is important to understanding southern Alaska tectonics.

A recent detailed field, petrographic, geochemical, and geochronological studies (Barefoot et al., 2020) has refined our understanding of the accreted Talkeetna arc–mélange relationships in the Nelchina Glacier area. What was previously mapped as metaplutonics of the Talkeetna arc/Peninsular terrane (MacKevett and Plafker, 1974; Pessel et al., 1981; Burns et al., 1991) was reidentified as mélange of the McHugh Complex, and the Border Ranges fault was reassigned to its defined placement between the arc and the accretionary wedge. This study focuses on a well-exposed fault zone ~1km south from the BRF, at the covered contact between the McHugh Complex and the Valdez Group. This contact is correlative with others that connect semi-continuously across more than 2000 km of southern Alaska in an arcuate shape (Figure 1). On Kodiak Island the contact is the Uganik thrust (Connelly, 1978; Sample and Moore, 1987; Sample and Fisher, 1986); on the Kenai Peninsula it is the Chugach Bay thrust (Cowan and Boss, 1978; Kusky et al., 1993); in the northern Kenai Peninsula and western Chugach Mountains it is the Eagle River thrust (Magoon et al., 1976; Pavlis, 1982; Winkler et al., 1992); and east of the Nelchina study area through the northern Chugach mountains it is mapped as the Tazlina fault (Winkler et al., 1981; Nokleberg et al., 1989; Plafker et al., 1989). The fault in my field area is most correlative to the Eagle River Thrust (ERT), because it lies along strike and matches the description of this fault as it was mapped west of the Matanuska Glacier (Little and Naeser, 1989).

Barefoot et al. (2020) mapped, sampled, and analyzed new exposures of the gabbroic mid-crustal section of the Border Ranges Ultramafic and Mafic Complex (BRUMC), as well as the inboard section of the McHugh Complex in this study area. Two primary assemblages are recognized within the McHugh Complex: the inboard Potter Creek Assemblage and the outboard McHugh Creek Assemblage (Clark, 1973; Amato and Pavlis, 2010: Amato et al., 2013). The Potter Creek assemblage accreted from Late Jurassic to Early Cretaceous with sediments sourced

from the Chitina and Talkeetna arcs, both of which are part of the Wrangellia composite terrane situated immediately north of the Chugach terrane (Figure 1; Amato and Pavlis, 2010). Complexly deformed mélange and meso-mélange blocks made of chert, argillite, basalt, metavolcanic rocks, rare limestone, and pillow basalts are well-exposed in my study area as well as along the whole inboard mélange assemblage. The outboard McHugh Creek section has only been described along the north side of the Turnagain arm, south of Anchorage (see location in Figure 1). It is more massive than the Potter Creek assemblage and composed only of metaclastic greywacke and conglomerate. Based on detrital zircon age arrays, it is likely sourced from the Jurassic Talkeetna Arc (Amato and Pavlis, 2010). The variable exposure of the McHugh complex is explained by intermittent episodes of subduction erosion and accretion from the Late Jurassic to Late Cretaceous (e.g., Haeussler et al. 2006; Bradley et al. 2007; Amato and Pavlis 2010). The larger part of the Chugach accretionary complex is the younger and more coherent flysch assemblage of the Valdez Group (Plafker et al., 1994). Its accretion age is well established from the Cretaceous to Eocene (Plafker et al., 1994; Amato and Pavlis, 2010). There was either a very brief or no age gap in deposition but a significant change in style of accretion between the McHugh Complex mélange and the Valdez Group flysch. The southern edge of the Valdez Group is bound by the outboard turbidite sediments of the Cenozoic Prince William terrane along the Contact fault (Figure 1; Plafker et al. 1994). Felsic hypabyssal dikes which cross-cut the accretionary complex record an episode of near-trench magmatism from Paleocene to Eocene time (Bradley et al. 1993; Bradley et al. 2003; Barefoot et al., 2020). Near the Nelchina Glacier, isolated exposures of Chickaloon Formation polymictic conglomerate, lithic sandstone, and mudstone, all of nonmarine origin, record rapid Paleocene uplift of the accretionary prism soon after emplacement of the Valdez Group (Little, 1988; Little and Naeser, 1989).

In this study, I examine the sheared equivalents of the metasediment mélange component which has been interpreted as the Potter Creek Section of the McHugh Complex (Barefoot et al., 2020), the Valdez Group exposures closest to the fault, and the Chickaloon Formation, which lies stratigraphically and physically above all units in the area.

Chapter 3: Methods

3.1 Field Data Acquisition

The main objectives of field work at the Nelchina glacier area were to document the stratigraphic and crosscutting nature of relationships between the different rock types, collect samples of sheared rocks and their undeformed counterparts, and make systematic measurements of structures including fault planes, slicken lines, joints, fold axes, crenulation cleavage, and veins. I collected 27 oriented samples, 11 of which were from within the fault zone, 9 from undeformed McHugh Complex rocks north of the fault, and 7 from Valdez Group exposures south of the fault (Table 1). I took structural measurements at every ~3m within the fault core.

3.2 Optical Microscopy

Standard light microscopy techniques were used on all samples to identify minerals in thin section, establish the nature of contacts between matrix and clasts, characterize the deformation microstructures, determine relationships among cross-cutting features, and select areas for Electron Backscatter Diffraction (EBSD) analysis.

3.3 X-Ray Diffraction (XRD)

Due to the fine grain size and high degree of alteration of the fault-rock samples, I used powder XRD analysis to constrain their mineralogy. I selected four samples, two from black fault rocks and two from lighter layers within the damage zone. Samples were crushed into small fragments (typically <0.5cm), milled in a Spex 8000D Mixer/Mill for three to five minutes, and then micronized for 10 minutes. The micronized materials were analyzed in a PANalytical X'Pert MRD X-Ray diffractometer, and PANalytical HighScore software was used for spectra

Table 1: *Sample list showing sample locations and types of analyses performed on each sample.*

Sample	Rock Type	Northing (m)	Easting (m)	Analyses*
Fault zone				
170801-1	black fault rock	6840308	495579	XRD
170801-2	black fault rock	6840307	495582	XRD, $^{40}Ar/^{39}Ar$ (WR)
170801-3	light fault rock	6840293	495586	TS, XRD, XRF, EBSD, $^{40}Ar/^{39}Ar$ (Ms)
170801-4	black fault rock	6840272	495587	TS, XRD, XRF, SEM, EBSD, Raman, $^{40}Ar/^{39}Ar$ (WR, Fld, Ms)
170801-5	black/light fault rock	6839715	495587	TS, XRD, XRF, SEM
170801-6A	light fault rock	6839659	495579	TS
170801-6B	light fault rock	6839659	495579	TS
170801-7	black fault rock	6839612	495575	TS
170801-8	black fault rock	6839584	495582	TS, XRD, $^{40}Ar/^{39}Ar$ (WR)
170801-9	qtz-rich cataclasite	6839526	495580	TS, EBSD
170801-10	light fault rock	6839496	495578	TS
Valdez Group				
170802-1	phyllite	6839367	495584	TS, EBSD
170802-2	phyllite	6839364	495589	TS
170802-3	phyllite	6839362	495590	TS
170802-4	phyllite	6839360	495592	TS
170802-5	quartzite	6839577	495559	TS
170802-6	argillite	6839577	495559	TS
170802-7	argillite	6839587	495560	
McHugh Complex				
170915-1	mudstone with qtz clasts	6840439	495568	-
170915-1A	mudstone with qtz clasts	6840439	495568	TS
170915-2	mudstone	6840282	495563	TS, EBSD
170915-2A	mudstone	6840282	495563	TS
170915-3	chert	6840150	495535	TS
170915-3A	chert	6840150	495535	TS
170915-4	carbonate	6840235	495485	TS
170915-4A	carbonate	6840235	495485	TS
170915-5	sheared basalt	6840599	495574	TS

* TS – Thin section examination; XRF – X-ray fluorescence; XRD – X-ray diffractometry; SEM – Scanning Electron Microscopy; Raman - Raman spectroscopy; EBSD - Electron Backscatter Diffraction; $^{40}Ar/^{39}Ar$ (WR, Fld, Ms) - $^{40}Ar/^{39}Ar$ dating (Whole-rock, K-feldspar, Metamorphic muscovite/Illite)

interpretation. To characterize the phyllosilicates present in the fault rocks, I separated them using a centrifuge and conducted an XRD analysis on the clay separates. XRD on an intermingled black and light fault rock slab was used to measure the crystallographic orientations of phyllosilicates. Orientation distribution function calculations and contoured pole figures from this analysis were generated with the MTEX toolbox for Matlab (Bachmann et al., 2010).

3.4 Wavelength Dispersive X-Ray Fluorescence (WD-XRF)

Major-oxide compositions of the four milled fault rock samples were determined using WD-XRF at the University Alaska Fairbanks–Advanced Instrumentation Laboratory (UAF–AIL). Powder samples were mixed and diluted at 1:10 with $Li_2B_4O_7$ and $LiBO_2$ flux and melted into glass beads. I analyzed the samples using a routine designed for major oxide analysis of glass beads on the WD-XRF.

3.5 Loss on Ignition (LOI)

To determine the amount and type of volatiles lost during glass bead preparation, I conducted a separate LOI study. LOI was determined from weight lost after ignition at 65°C, 440°C, and 1000°C for 12 hours at each temperature. These steps distinguished the weight percentages of water, organic carbon, and all other volatiles.

3.6 Scanning Electron Microscopy (SEM)

I used SEM to investigate the differences in textures, microstructures, and compositions between the lighter and darker fault rocks. Thin sections were carbon coated and examined with a Jeol 5600 SEM equipped with an energy-dispersive X-Ray spectroscopy (EDS) detector at UAF–AIL, as well as a FEI Scios DualBeam FIB/SEM equipped with a field-emission gun and

EDS at University of California, Davis. SEM micrographs were collected in both secondary electron and backscatter electron modes.

3.7 Electron Backscatter Diffraction (EBSD)

EBSD is an important tool for understanding crystalline structures, and can be used to identify phases and measure crystallographic axis orientations. I used EBSD measurements to identify crystallographic preferred orientations and to generate maps for grain size and shape analysis. EBSD and EDS data were collected at California State University Northridge, on their FEI Quanta 600 SEM equipped with Oxford Instruments Nordlys EBSD detector and INCA x-sight EDS detector. Orientations and maps were generated by Oxford Instruments Aztec EBSD acquisition software. Critical to quality EBSD data acquisition, each thin section was polished for an hour in a colloidal silica solution. The analysis was performed on uncoated samples under low vacuum (20 Ps H_2O) to minimize charging. A conventional beam-mapping technique was used to generate fifteen maps from five quartz-rich samples: three fault rocks, one McHugh argillite sample, and one Valdez Group flysch sample.

The Oxford Instruments Channel 5 Tango program was used to display and reduce noise in the EBSD map data. Noise reduction removed wild spikes—single pixels with a different orientation from eight neighboring pixels—as well as erroneously indexed pixels and those analyzed as zero solutions. The applied minimum size requirement for a grain was 5 pixels. Following convention, grains are defined by adjacent boundaries with ≥10 degrees of misorientation (e.g., Trimby et al., 1998; Halfpenny et al., 2012), and subgrain boundaries are between adjacent grains with misorientation of more than 10 degrees.

Crystallographic orientation data was displayed in pole figures and their contoured variations created with the MTEX toolbox for MATLAB (Bachmann et al., 2010). All pole

figures shown are lower-hemisphere, equal-area projections as well as in the kinematic reference frame. I quantified fabric strength using the M-index calculation of Skemer et al. (2005). Shape preferred orientation (SPO) was determined with the 'principalComponents()' function of MTEX, which calculates the axis lengths and orientations of the elliptical fits for all grains in a single map. I also applied the image-processing tools ImageSXM and ImajeJ to confirm the SPO analysis results from the EBSD maps.

3.8 $^{40}Ar/^{39}Ar$ thermochronology

Four fault-rock samples—three black fault rocks (samples 170801 -2, -4 and -8) and one light-colored fault rock (sample 170801-3) were selected for $^{40}Ar/^{39}Ar$ thermochronology based on their concentration of Potassium as measured by hand-held XRF. Jeff Benowitz, director of the Geochronology Lab at UAF, crushed the rock and prepared the mineral separates. All samples were dated by Laura Webb at the University of Vermont. Ages from the three black fault rocks were determined from whole-rock, feldspar, and illite extracted from sample 170801-2, 170801-4, and 170801-8. Ages for the lighter rock came from illite from sample 170801-3.

3.9. Raman spectroscopy

Raman spectra were obtained on one probe-polished petrographic thin section (sample 170801-4) of the black fault rock, in order to determine the thermal maturity of the opaque carbonaceous material. The in-situ analysis was completed by Jonathan Caine (USGS) at the University of Colorado Boulder using a Horiba LabRAM HR Evolution high-resolution 800 mm spectrometer equipped with confocal optics. Peak position, integrated band area, and half maximum band width were determined using Matlab. Peak fitting and deconvolution were

performed in order to calculate the peak area ratio (R2) used to determine peak metamorphic temperature for the sample (after Beyssac et al., 2002).

Chapter 4: Results

4.1 Field observations

The McHugh Complex can be divided in three lithologically distinct sections: metasedimentary, metavolcanic, and mesomélange, all of which have been metamorphosed to greenschist facies. Black argillite which weathers to orange comprises most of the rock volume in the metasedimentary section. Locally it includes chert ribbon and green tuff layers of a few centimeters to 1-meter thickness. The ribbon chert is also found as a separate block of ~10 m width. The metavolcanic section consists of a ~250-m wide block of pillow lava. Well-developed pillow structures are found in the core of the block, away from which they become progressively obscure until completely absent. South of this exposure, there is a smaller volcaniclastic block with a more massive appearance and no notable structures. The mesomélange is made up of complexly intermingled metasediments and metavolcanics in blocks less than 10-m wide.

Shear planes with slicken lines are commonly found at contacts between the metasedimentary and metavolcanic sections (Figure 3A). There is no consistency amongst the measured shear plane and slickenline orientations (Figure 3B). The chert unit of the McHugh Complex retains original bedding in the form of ribbons which are stretched and folded (Figure 3C). The fold axes from across different chert blocks show no strong preferred orientation (Figure 3D).

The majority of the deformation features are concentrated in the ~120 m wide shear zone at the southernmost part of the McHugh complex. There a dominating population of shear planes strike east–west and dip on average 50 degrees north (Figure 3F). A small number of antithetic fault planes, striking north-south and dipping ~90 degrees, are also present. The mineralogy of the rocks in the fault zone is hard to determine in the field as the majority consists of a fine

cataclasite. I distinguish between light and black fault rock, which alternate in layers from 20 cm up to 1 m (Figure 3E). Quartz rich clasts are abundant in both the light and black layers. The clasts vary in size from 1 to 10 cm and commonly appear ductilely deformed in outcrop, as rounded porphyroclasts with recrystallized tails aligned in an orientation consistent with the main fault fabric, striking east-west (Figure 3G). The foliation in the fault rocks is defined by the shear planes and the compositional layering (black vs light fault rock). Lineation orientations were hard to find in the field, with the exception slicken lines preserved along shear planes. Predominant jointing cross-cuts the shear planes close to perpendicular.

Lithology of the Valdez Group, south of the shear zone, consists of medium- to thinly-interbedded graywacke turbidites, black argillite, sandstone and rare chert. The sandstone layers are rich in moderately sorted quartz and feldspar grains, and minor volcanic fragments. There are pervasive bedding-parallel quartz veins. Both the chert layers and the quartz veins have been widely boudinaged. Slaty cleavage which has the same general orientation as the fault zone foliation is observed in the greywacke-argillite sections (Figure 3H and 3I). Another pervasive deformation feature in the whole Valdez Group exposure is small-scale folding. Crenulation lineation parallels the orientation of the fold axes (Figure 3J). No evidence of shearing along fracture planes was observed.

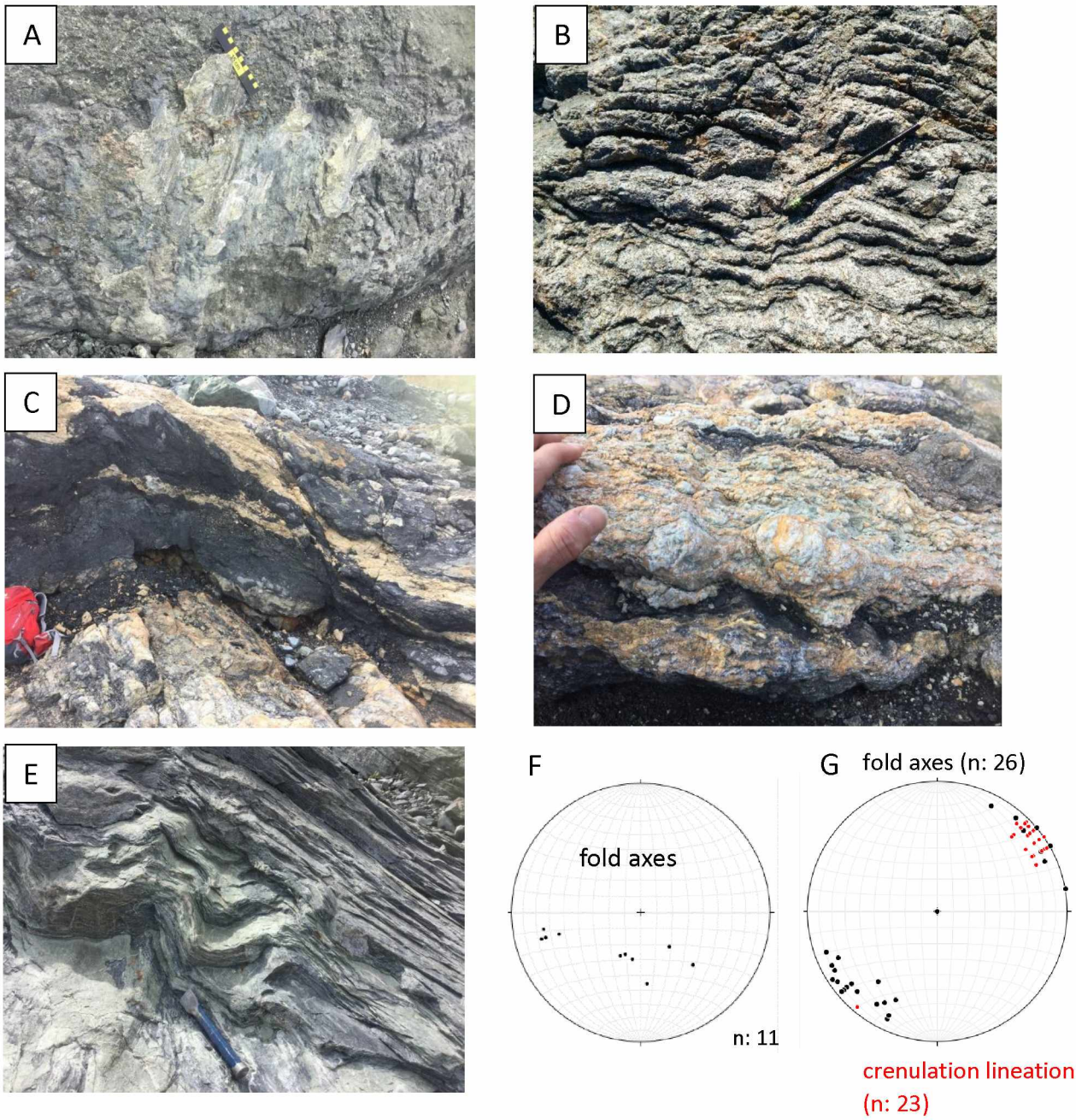

***Figure 3**: Outcrop photos of structures and stereonet plots of measurements of deformation features; n = number of measurements. (A) Fault plane with slicken lines within the McHugh volcaniclastic unit; 15-cm ruler for scale. (B) Folded ribbon chert in McHugh Complex; pencil for scale. (C) Folded layers of black and light fault rock; backpack for scale. (D) Light fault rock with boudinaged quartz-rich clasts; hand for scale. (E) Folded remnant bedding with crenulation cleavage in the Valdez flysch; chisel for scale. (F) Stereonet plot of fold axes from the ribbon chert folds. (G) Stereonet plot of fold axes and crenulation cleavage orientations in the Valdez flysch.*

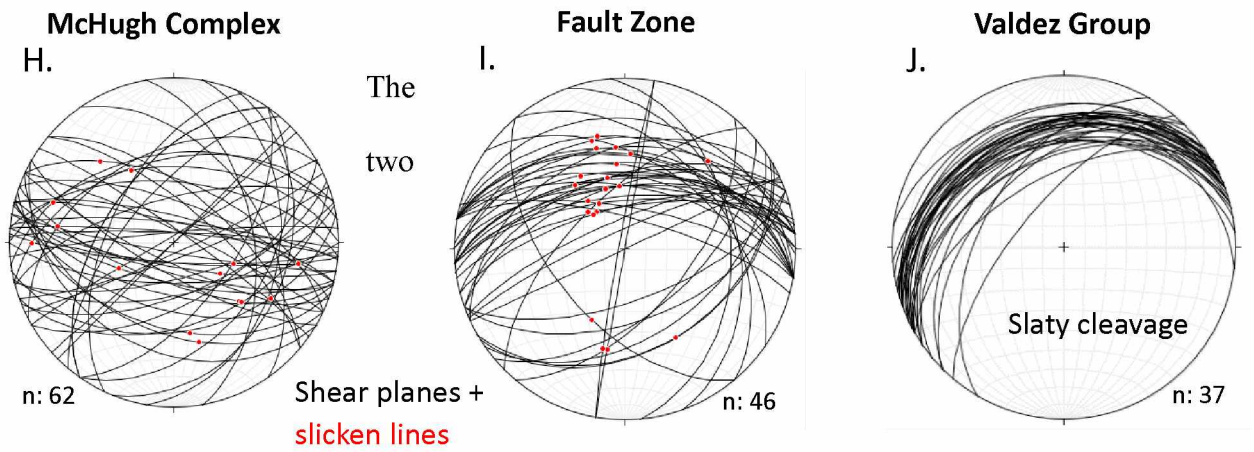

***Figure 3 (continued)**: (H) Stereonet plot of shear planes and slickelines (red dots) in McHugh Complex. (I) Stereonet plot of orientations of fault planes and slicken lines in the shear zone. (J) Stereonet plot of orientation of remnant bedding/slaty cleavage in the Valdez flysch.*

Eocene-aged units in the area, provide useful age constraints for deformation. The Chickaloon Formation, a matrix-supported conglomerate, unconformably overlies the shear zone. It is largely undeformed, but localized shearing within 1-2m of the base includes slickenlines, rotated and aligned clasts, conjugate jointing, and some fault gouge (Figure 4). The Eocene felsic dikes cross-cutting the McHugh mélange, vary in width from 2m to 50m. Plagioclase phenocrysts make up ~10% of the rock, and are surrounded by fine-grained gray groundmass that weathers to orange-pink. These dikes, which parallel the northern edge of the shear zone, are pervasively altered but show no evidence of deformation or offset (Figure 5).

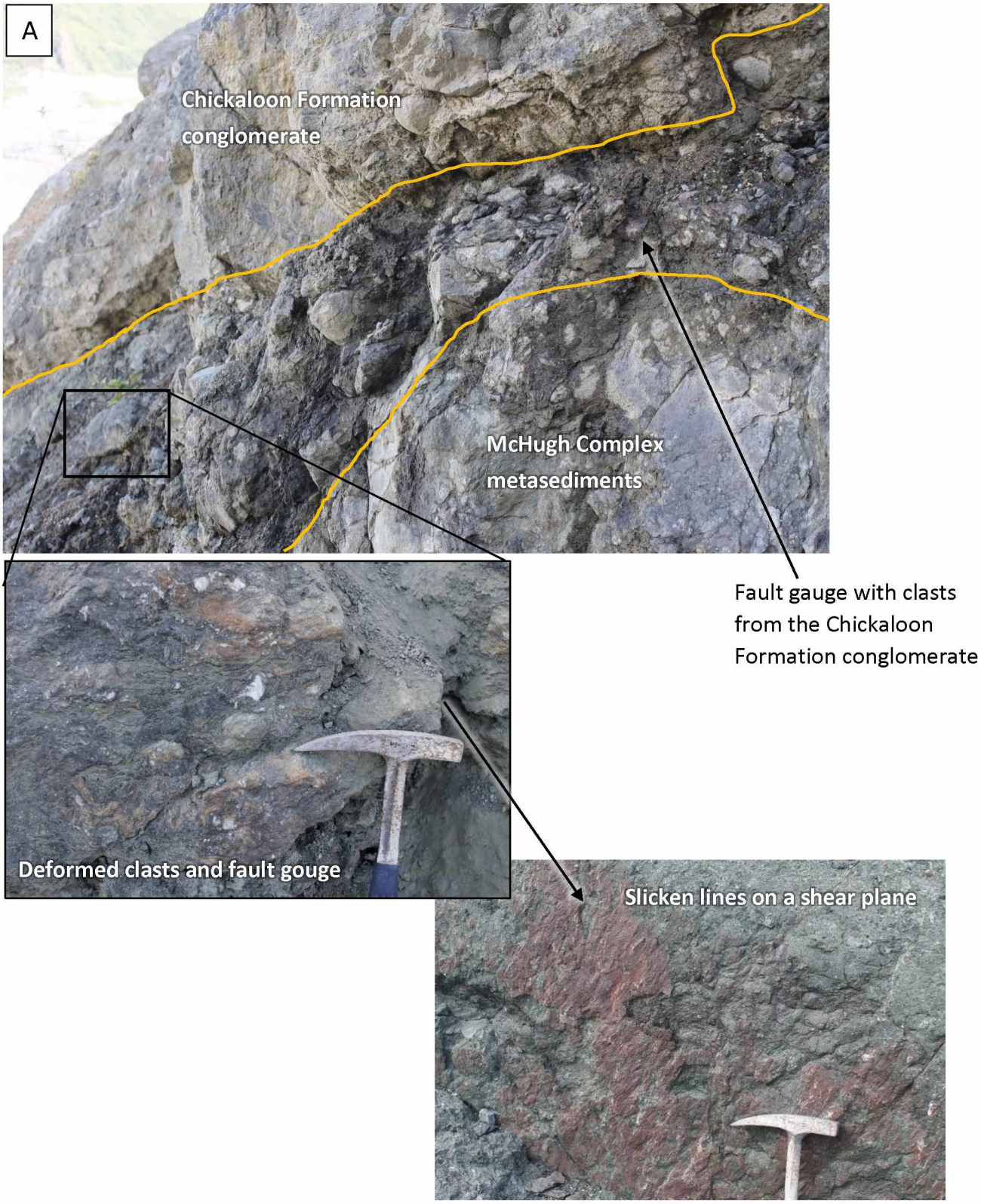

***Figure 4**: Outcrop photos of the deformed base of the Chickaloon Formation with brecciated conglomerate, fault gouge, and shear planes.*

***Figure 5**: Outcrop photos of the undeformed Eocene felsic dike, situated between north edge of the shear zone and the southern extent of the McHugh metasediments.*

4.1.1 Fault Zone Architecture

I divide the fault zone in two distinct sections: fault core and damage zone (Figure 6A, B). The fault core extends about 100m within the center of the fault zone. It consists of the alternating black and light fault rocks. The damage zone borders the fault core to south and to north along its strike. It consists of alternating green and black layers. The green layers resemble the metavolcanic tuff layers within the undeformed McHugh complex, and the black layers resemble the black mudstone interlayered with the tuff. In the damage zone, however, there are preferentially oriented chlorite minerals defining a fabric, as well as a higher degree of folding, fracturing and pyrite mineralization. Pyrite mineralization increases with proximity to the fault core. The damage zone/fault core boundary is not a clear-cut line, instead it is expressed as a progressive change in color from green to light yellow towards the fault core. Within a 2-3m range the quartz-calcite vein network density increases towards the fault core. Showing a lot more fluids moved through the fault core and altered the rock in that zone. A schematic representation of the fault zonation is illustrated in Figure 6A.

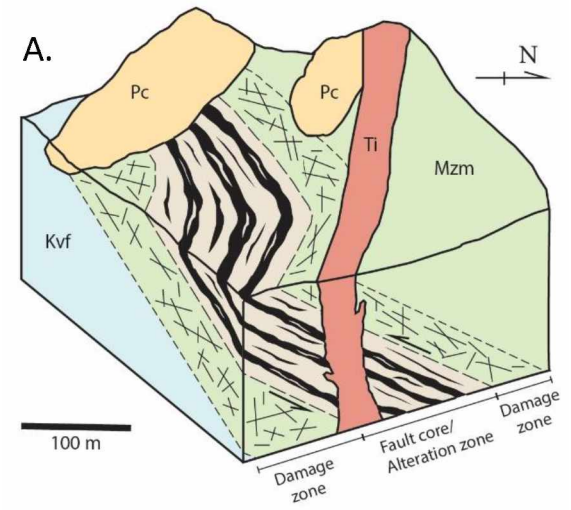

***Figure 6**: Fault zone architecture. (A) Block cross-section with fault zonation.*

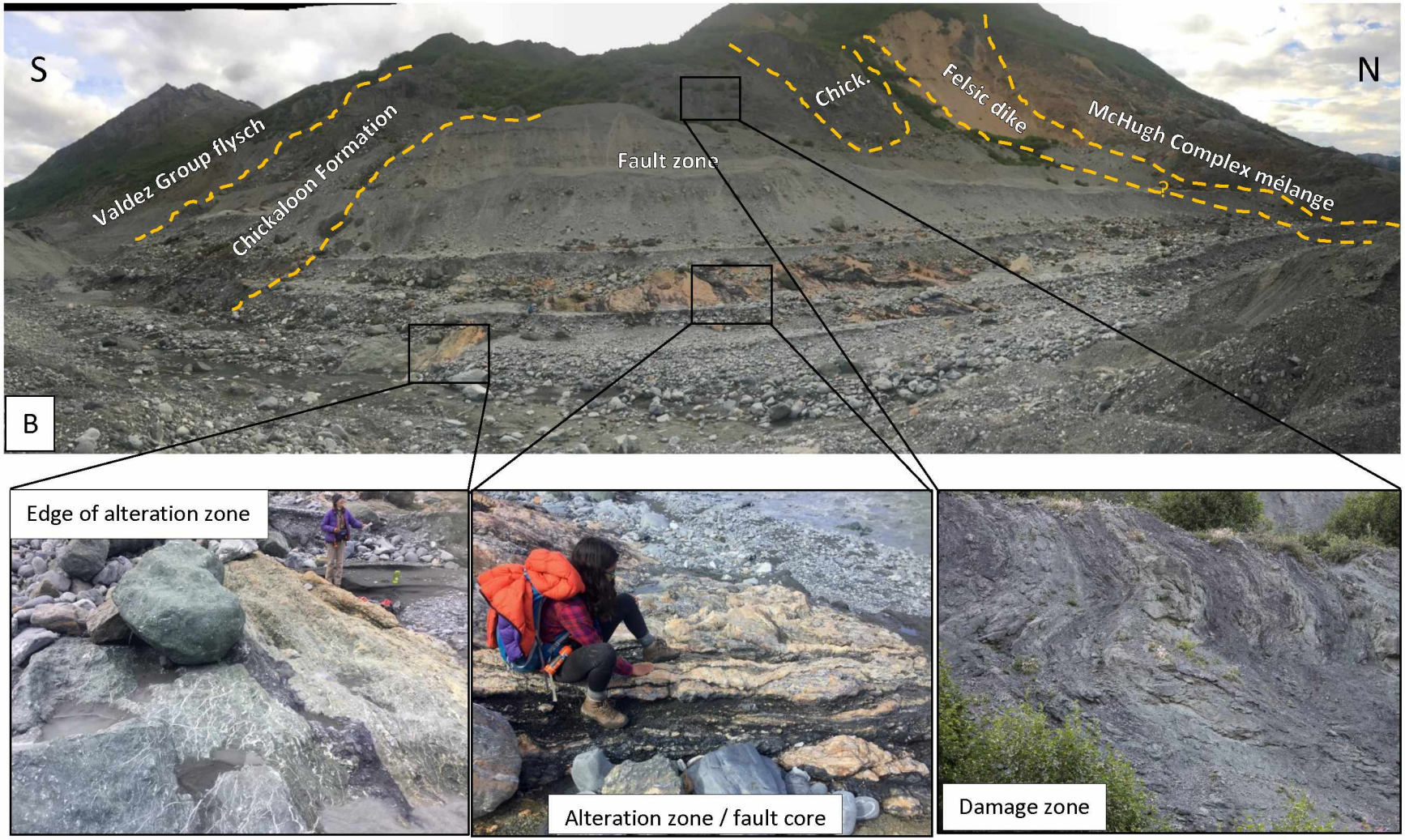

***Figure 6 (continued)**: (B) Panoramic view of the project field area with outlined sections. Insets show the different zones within of the fault.*

4.2 Microstructures with Light Microscopy

4.2.1 McHugh Complex

The chert layer is primarily composed of microcrystalline quartz matrix (Figure 7A). Coarser-grained quartz (0.05-0.5 mm diameter) forms a complex network of monomineralic veins with widths ranging from 0.1 mm to 1 mm (Figure 7A). The majority of the vein quartz grains are blocky and slightly elongate. Graphite is concentrated along pressure solution seams between layers of quartz that have different grain sizes (Figure 7B). There are two generations of calcite veins (Figure 7B), with coarser-grained (up to 0.2mm diameter) calcite veins cross-cutting the finer-grained ones (up to 0.01mm diameter), as well as the quartz veins and pressure solution seams (Figure 7B).

The black argillaceous metasediment section within the McHugh Complex consists of quartz-rich clasts (0.5-5mm) surrounded by fine-grained black matrix with a weak fabric (Figure 7C). Both the quartz clasts and the matrix are cross-cut by a network of carbonate veins. The grain size in the quartz clasts ranges from 10-100 μm and the crystal shapes are irregular, embayed, sub-rounded, and pervasively fractured. The fractures are filled with a mixture of fine-grained quartz and carbonate. The matrix is very fine grained (< 1 μm) and, due to its dark color, no microstructures can be observed optically. It generally wraps around the quartz clasts. Pre-existing quartz veins up to 2 mm thick appear fractured and sheared (Figure 7D).

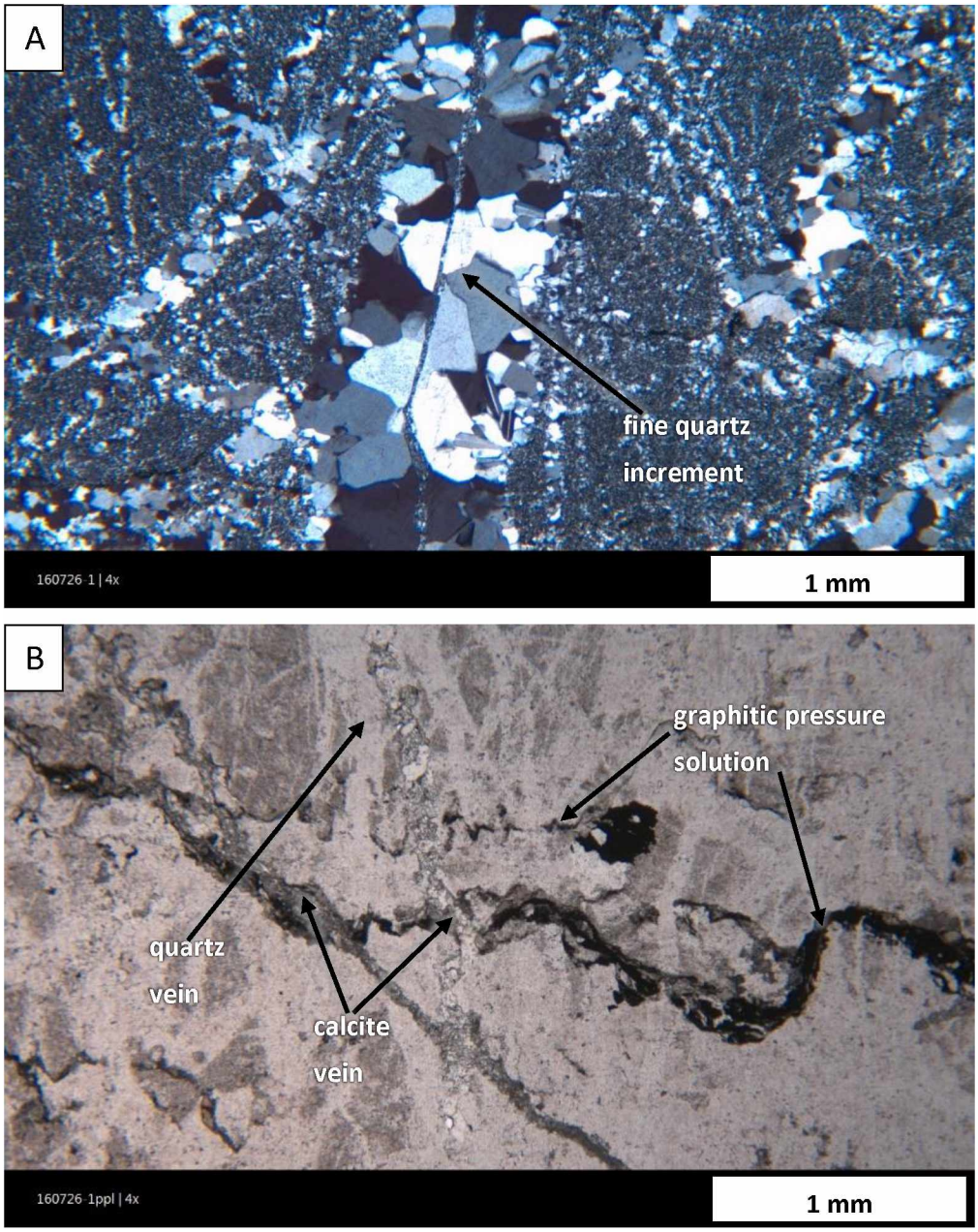

***Figure** 7: Photomicrographs of McHugh Complex samples. Sample numbers indicated on lower left corner of the figures. (A) Monomineralic quartz vein with blocky crystals and a tracking running through the middle - evidence for two opening increments. (B) Pressure solutions concentrating graphite (opaque) with calcite veins cutting across them (plain polarized light).*

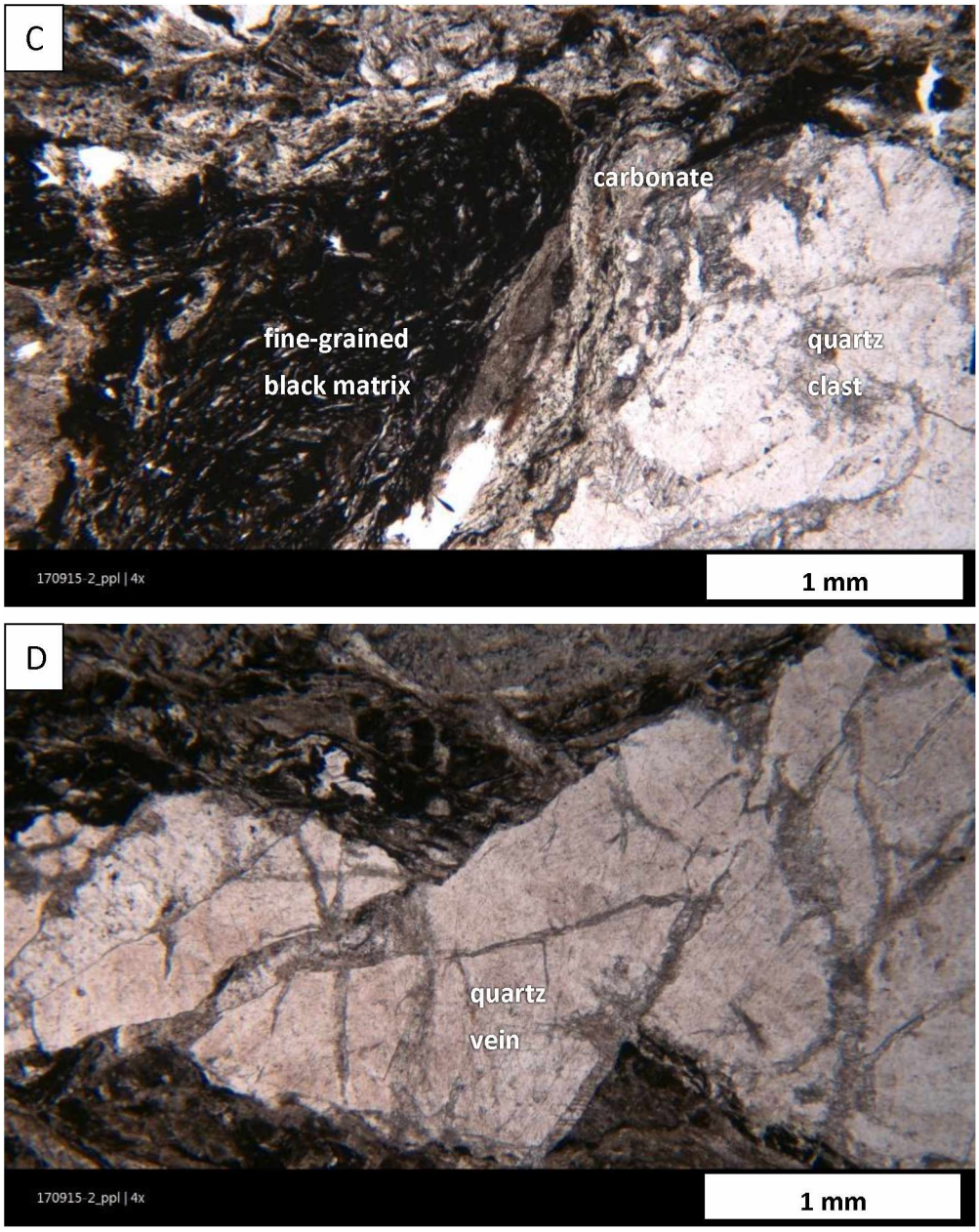

Figure 7 (continued): *(C) Quartz-rich clasts surrounded by fine-grained black matrix with a weak fabric wrapping around the clasts. (D) Thick quartz vein which has been stretched, fractured and sheared.*

4.2.2 Fault Rock

4.2.2.1 Lighter fault rock

In this section it is evident that the quartz clasts of the lighter fault rock, which appear stretched in the field, are actually brittlely deformed. Quartz clasts are elongated through stretching and fracturing. Fractures are regularly spaced and have an even width (Figure 8A). Carbonate veins cut the quartz clasts and fill the complex network of fractures. The carbonate veins are so pervasive, they resemble a very fine-grained matrix (< 1 μm) surrounding the quartz clasts. The grain size of the quartz making up the clasts ranges from 10-200 μm. The finer of these grains (< 50 μm) have regular boundaries and are equant. The coarser crystals (> 50 μm) have more irregular boundaries than the fine-grained quartz. They show some subgrain formation and sweeping extinction (Figure 8B), and are elongate in a preferred orientation similar to that of the overall clast orientation which defines the fabric in the samples.

4.2.2.2 Black fault rock

Under the microscope the five black fault rocks samples show well-developed foliation with fine-grained (< 1 μm) carbonate mixed with opaque carbonaceous material that wraps around quartz clasts. The boundaries between matrix and clasts are sharp, with the matrix rarely cross-cutting the clasts (Figure 8C). Over 90% of the clasts from all samples are elongated and rounded. The stretched clasts consist of carbonate and clays. Individual grains of quartz-rich clasts range from 1 to 1000 μm in diameter. The smallest quartz grains (<10 μm) have straight grain boundaries and are euhedral. The medium-sized grains (10-500 μm) have bands of smaller grains and exhibit sweeping extinction (Figure 8D). The coarsest quartz grains (>500 μm) display undulose extinction and brittle fracturing, as well as local deformation lamellae (Figure

8E). The fractures are filled with fine quartz grains (<10 μm) which grew with a different orientation from the coarse grains.

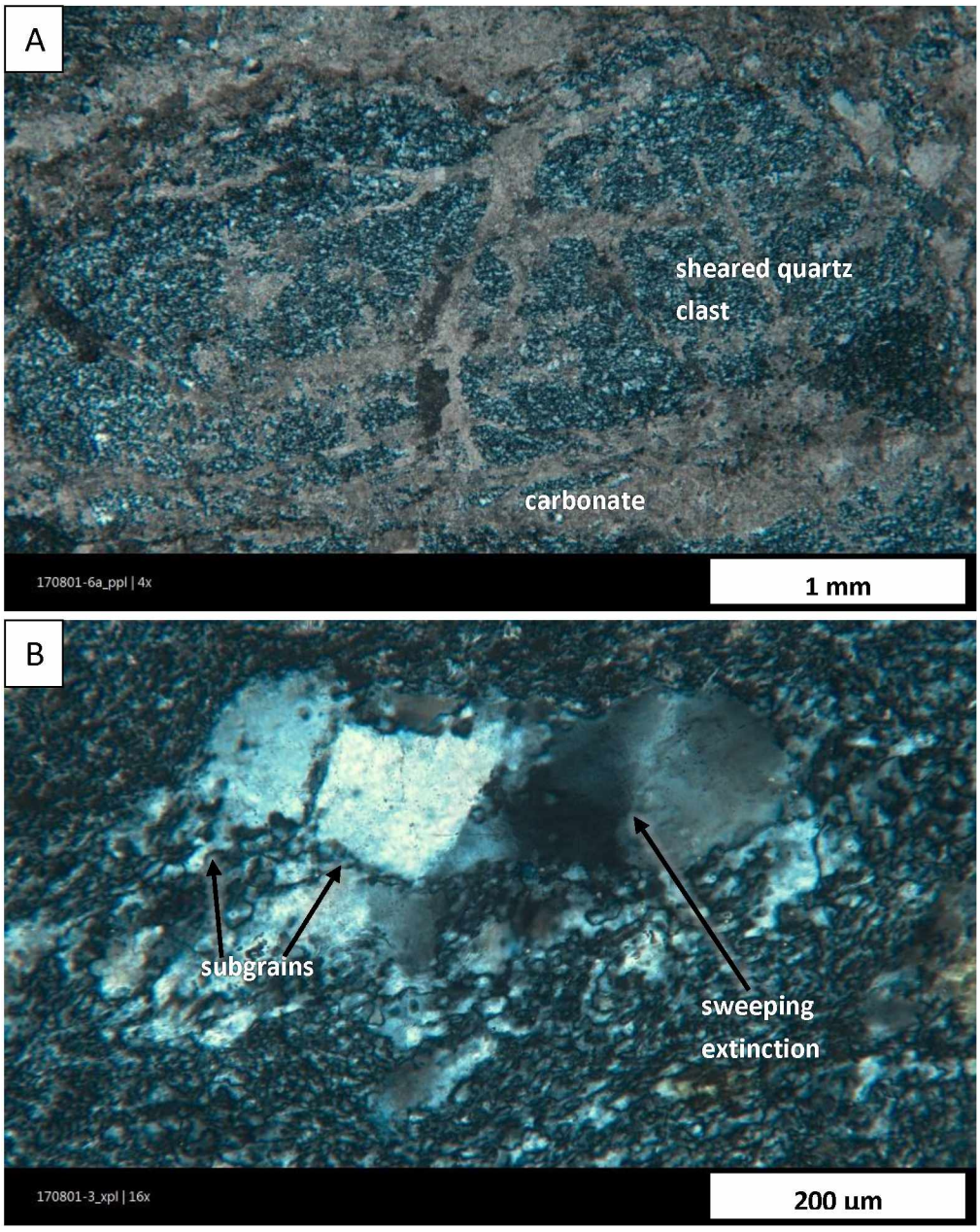

***Figure 8**: Photomicrographs of fault rock samples all shown in cross-polarized light. Sample numbers indicated on lower left corner of the figures. (A) Light fault rock with fractured quartz clast in a network of carbonate veins. (B) Light fault rock with bulging, subgrain development and sweeping extinction in coarser quartz crystals.*

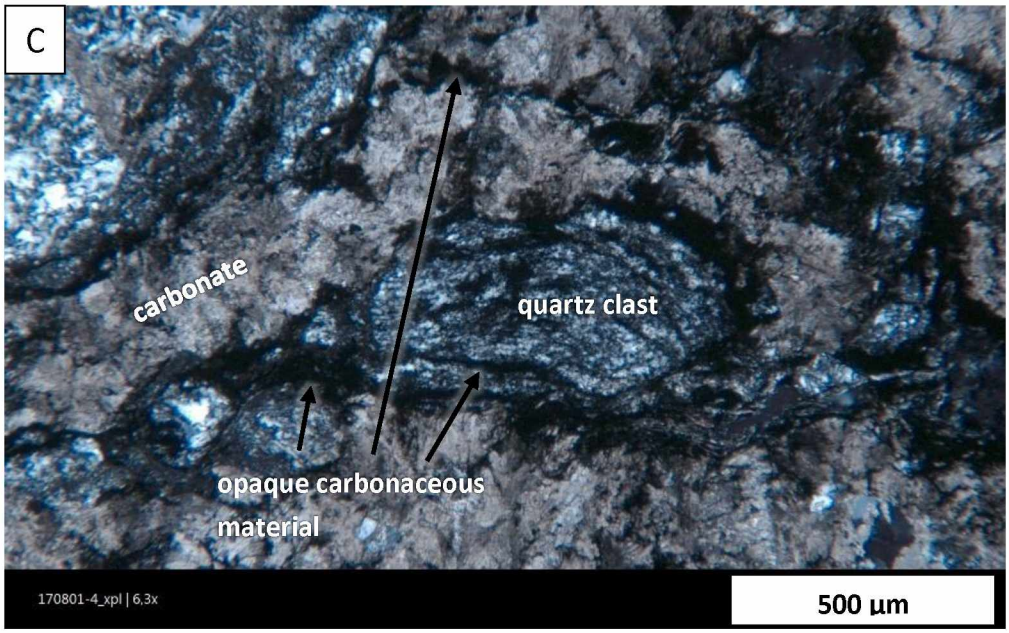

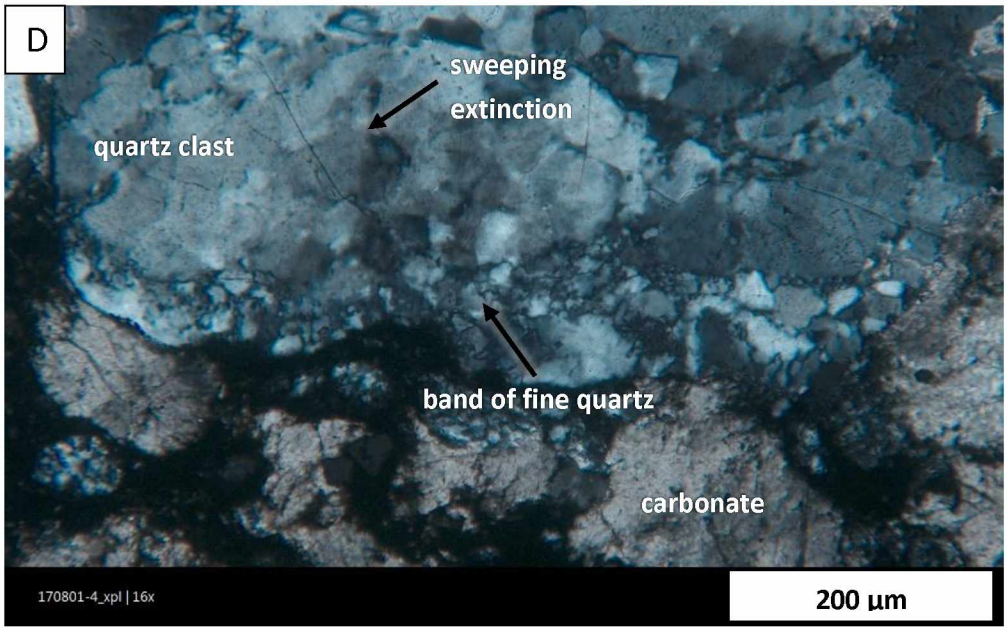

***Figure 8 (continued)**: (C) Black fault rock with opaque carbonaceous material with a flow-like texture wrapping around and intruding into quartz clasts. (D) Subgrains developing along coarser quartz grain boundaries with sweeping extinction in the coarser crystals of black fault rock.*

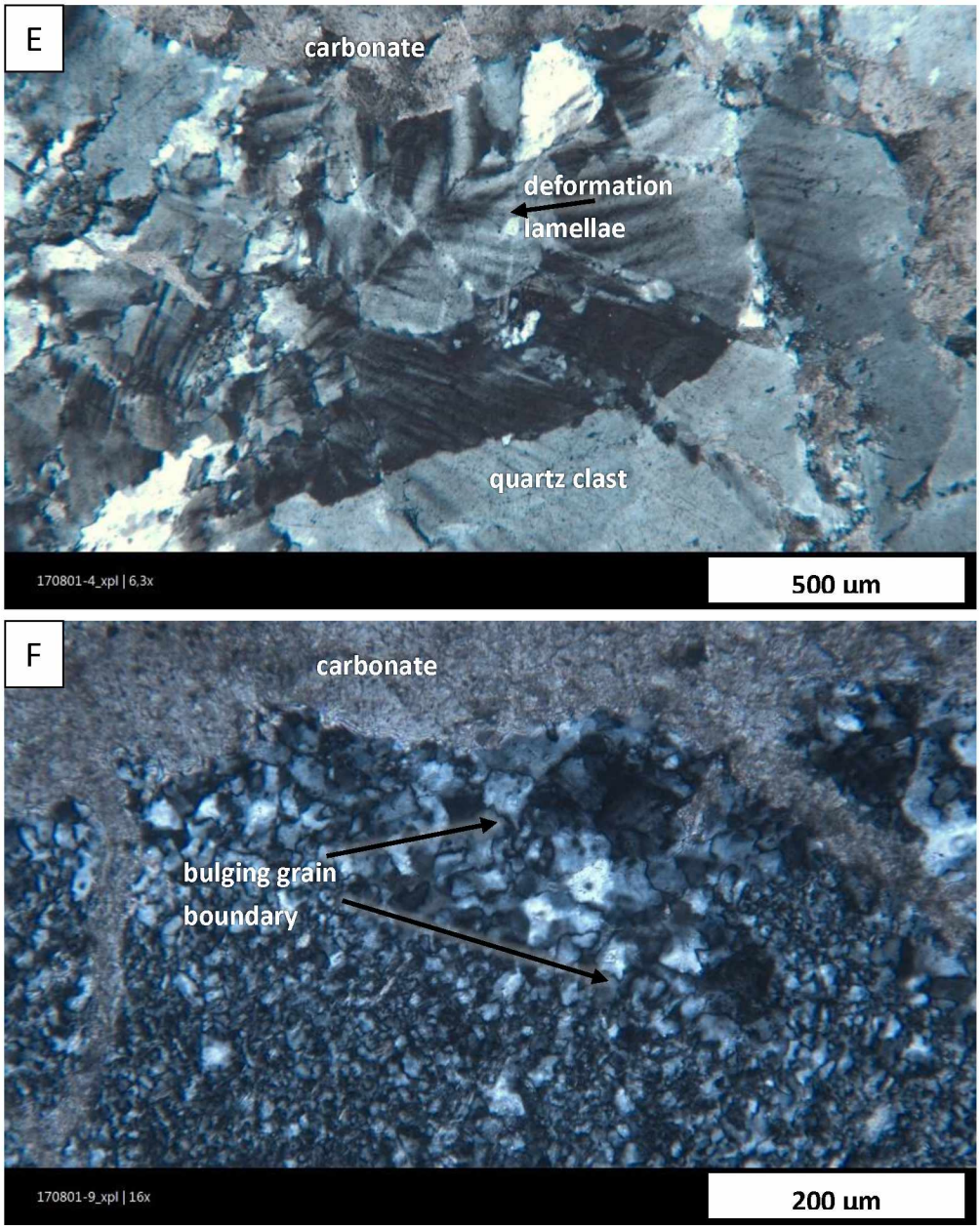

***Figure 8 (continued)**: (E) Black fault rock with deformation lamellae in quartz. (F) Quartz-rich fault rock with bulging grain boundaries, subgrain formation and undulose extinction.*

4.2.2.3 Quartz-rich fault rock

Microscopic observation reveals quartz is the most abundant mineral phase (>90%) in the northernmost exposure of the shear zone. The quartz is interconnected in domains and clasts are absent. Quartz grain sizes range from 10-100 μm (Figure 8F). The majority of the crystals are fine grained (<20 μm), slightly elongated, and with mostly straight grain boundaries surrounded by fine quartz grains. The coarser-grained quartz (>20 μm) has irregular and at places bulging grain boundaries, distinct subgrains, as well as undulose extinction (Figure 8F). Brittle fractures with carbonate infill cut the quartz grains. Very thin veins of black material (10-100 μm thickness) inject into both the quartz crystals and carbonate veins.

4.2.3 Valdez Group flysch section

The Valdez flysch is characterized by its rhythmic/turbiditic bedding. Under optical microscope, quartz-rich stretched clasts are aligned parallel to the slaty cleavage (Figure 9A). Individual quartz grains are small (<15 μm), equant, with straight grain boundaries. The matrix defining the slaty cleavage is very fine grained (< 1 μm) so I determined its mineralogy by EBSD. Quartz veins cross-cut the samples in three different orientations (Figure 9B). In places, the veins have been stretched and rotated in a direction indicating dextral shear (Figure 9C). In the veins perpendicular to foliation, the quartz grains are elongate with their long axes parallel to foliation (Figure 9D).

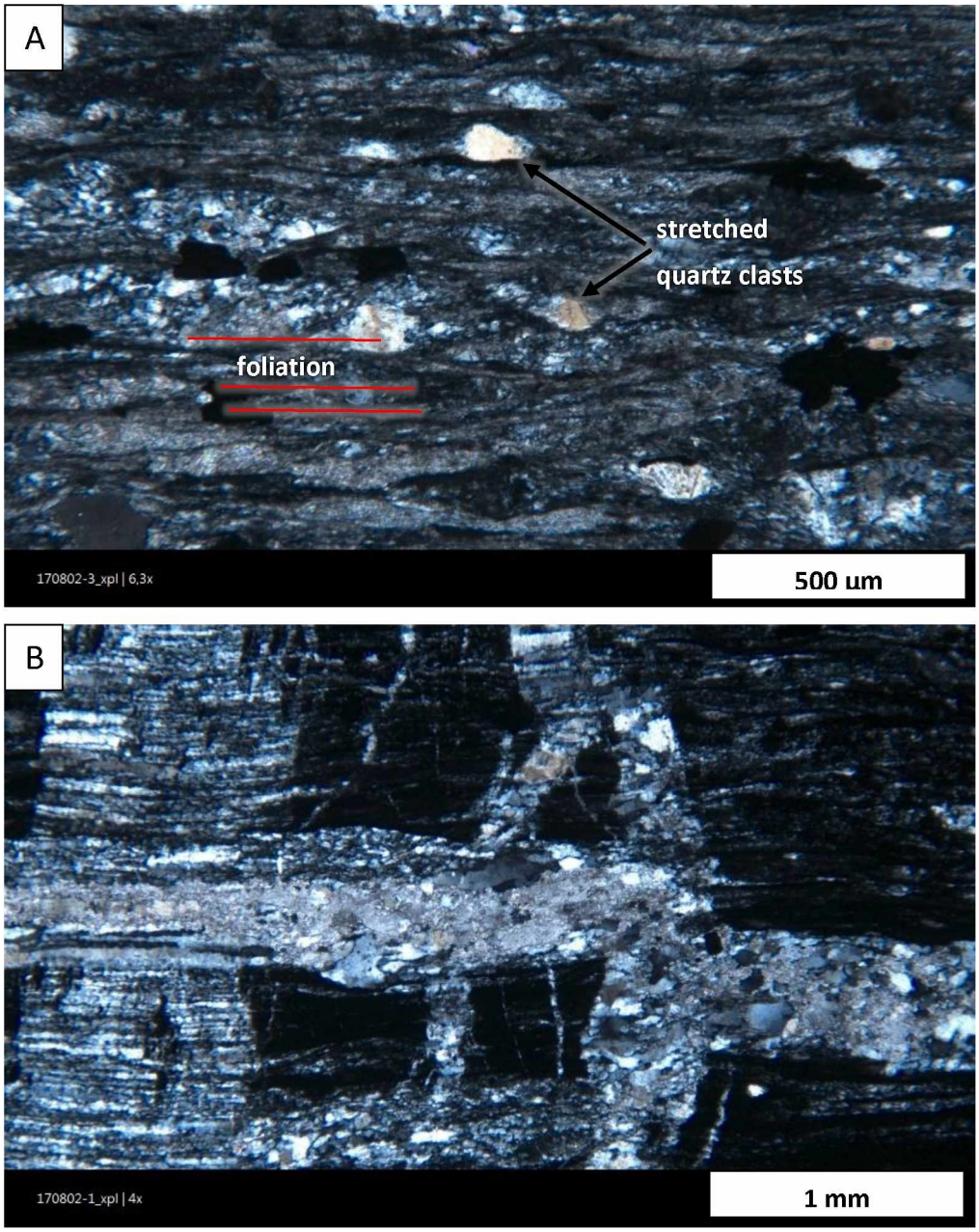

Figure 9: *Photomicrographs of Valdez Group samples in cross-polarized light. Sample numbers indicated on lower left corner of the figures. (A) Stretched quartz clasts parallel to foliation. (B) Quartz veins cross cutting the sample in three prominent orientations.*

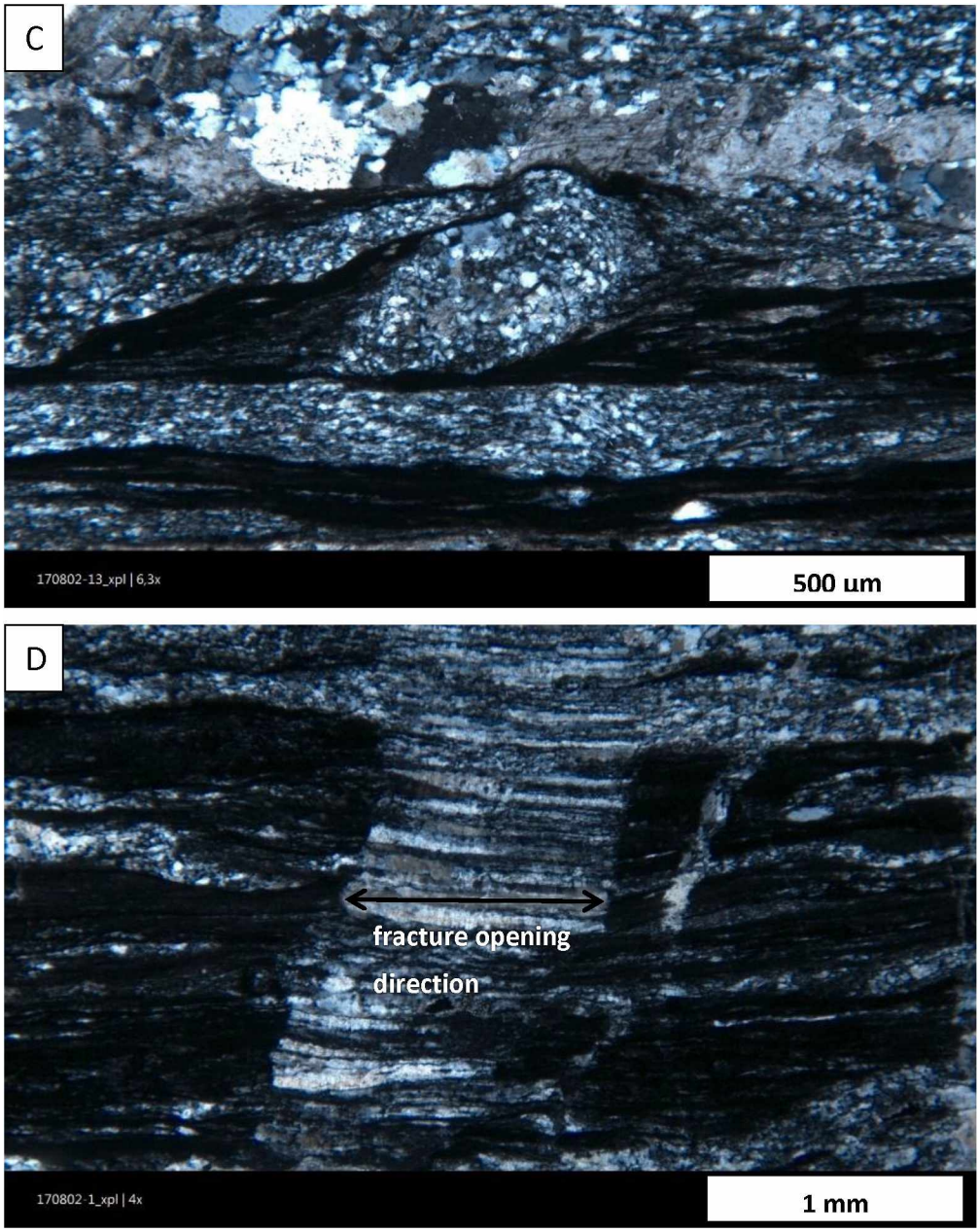

Figure 9 (continued): *(C) Stretched and rotated quartz vein with a dextral shear sense. (D) Fine elongate quartz crystals growing parallel to fracture opening direction.*

4.3 Microstructures with SEM

4.3.1 Lighter fault rock

The lighter fault-rock contains grains of subrounded quartz, feldspar (albite) and ferrous dolomite (10-100 μm), with interstitial, randomly oriented, platy Al-rich clay (<5 μm). The grains-to-matrix ratio is 2:1. Most of the coarser quartz and plagioclase appear to be intergrown, with phyllosilicates surrounding their margins (Figure 10A). The dolomite grains have an irregular shape and are intergrown with the albite (Figure 10A). Fractures nucleate in the interstitial space, without affecting the grains. The lighter fault rock contains angular grains of rutile commonly associated with the carbonate (Figure 10A and 10B). Rutile has two distinct forms: as interconnected domains with dolomite (50-200 μm in length, Figure 10A) within the coarser carbonate; and as scattered individual grains in the matrix (Figure 10B). The matrix phyllosilicates "card-deck" stacking of clay (Figure 10F).

4.3.2 Black fault rock

In contrast to the lighter fault rock, the black fault-rock contains grains of subrounded ferrous dolomite and quartz. Grain size varies from 10-500 μm in diameter. The matrix is characterized by preferentially oriented illite crystals <5 μm in diameter (Figure 10D and 10G). The increase in phyllosilicate abundance is significant compared to the lighter fault rock. The grain-to-matrix ratio in the black fault rock is 1:2. The carbonate and quartz grains have irregular shapes and appear as individual grains with phyllosilicates surrounding their margins (Figure 10 D). Dolomite is commonly mantled with the rims rich in Fe (Figure 10C), and appears as individual grains scattered throughout the rock. The quartz crystals are typically fractured. Fractures propagate through interstitial space, and clays are preferentially oriented along the fractures in two distinct ways: either parallel (Figure 10D) or perpendicular (Figure 10G) to the

orientation of fractures. The matrix phyllosilicates display flow-like foliation, wrapped around bigger clasts (Figure 10D). The black fault rock contains fine angular grains of pyrite (1-20 μm), disseminated within the matrix (Figure 10D and 10E).

Mutual crosscutting relationships occur between the two variations of fault rock. They are separated by planar boundaries with black matrix veins injecting into the lighter layers. There are also clasts from the lighter fault rock indenting into or completely encompassed by the darker fault-rock matrix (Figure 10E). Pyrite is present only in black fault rock, so its presence (or absence) was used to distinguish the two fault-rock variations.

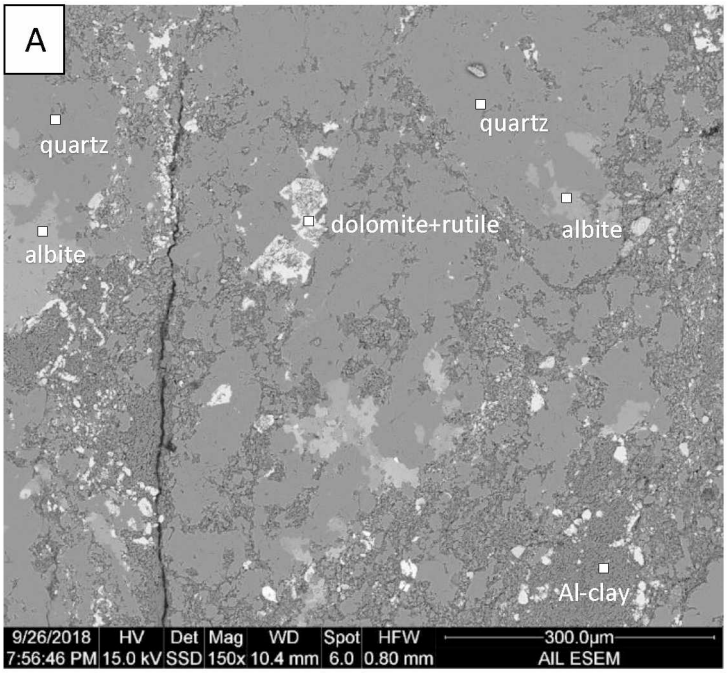

Figure 10: *SEM images of fault rock samples showing compositional differences between the lighter fault rock and the black fault rock. White squares indicate spots of EDS analysis. (A) Minerals in the light fault rock; sample 170801-5.*

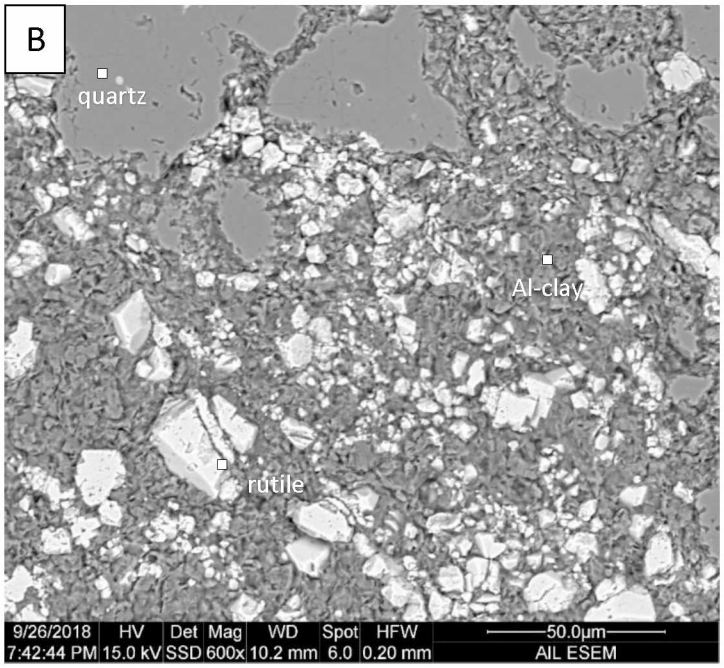

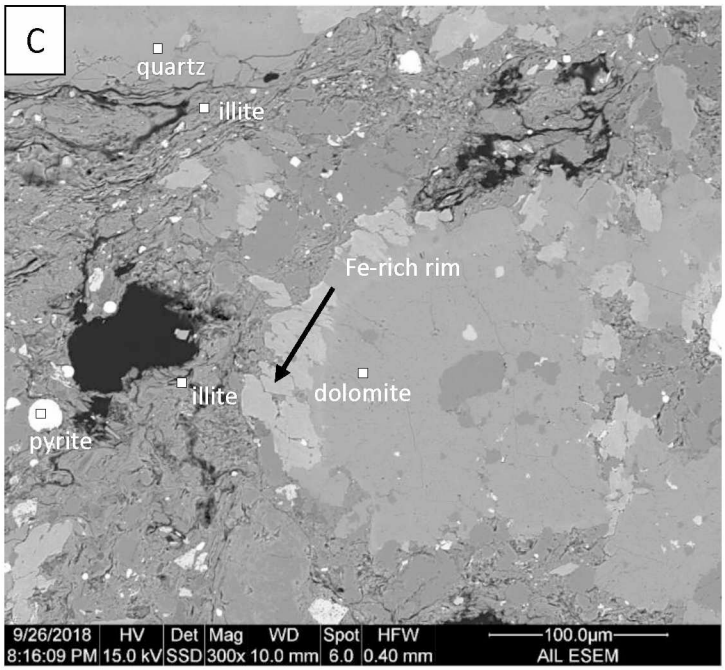

Figure 10 (continued): *(B) Scattered rutile in light fault rock matrix; sample 170801-5. (C) Compositionally zoned dolomite and quartz in black fault rock in an illite-rich matrix; sample 170801-4.*

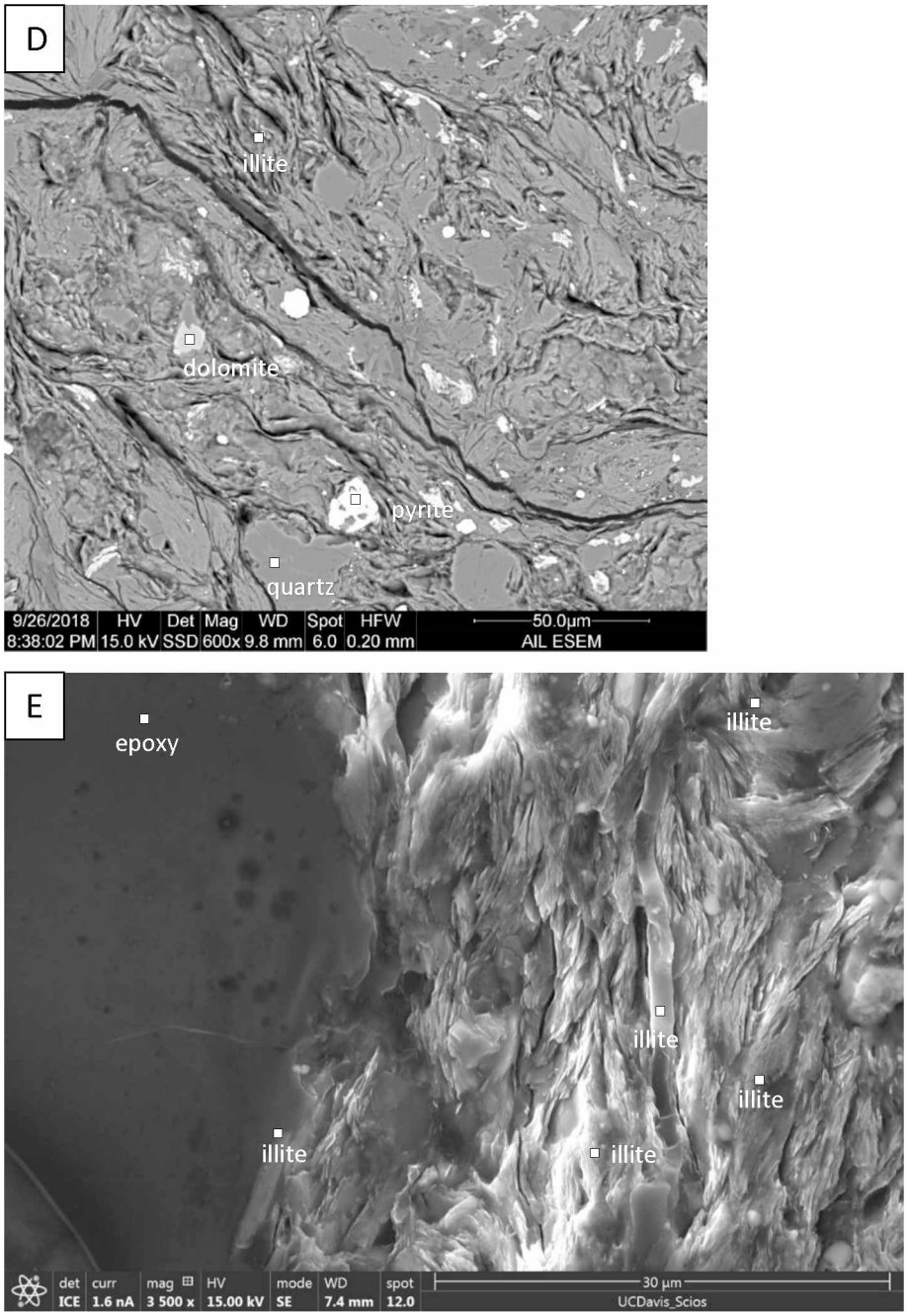

Figure 10 (continued): *(D) Flow-like texture of illite and nucleating fractures in black fault rock; sample 170801-4.* (E) "Card-deck" stacking of clays in light fault rock; sample *170801-5*.

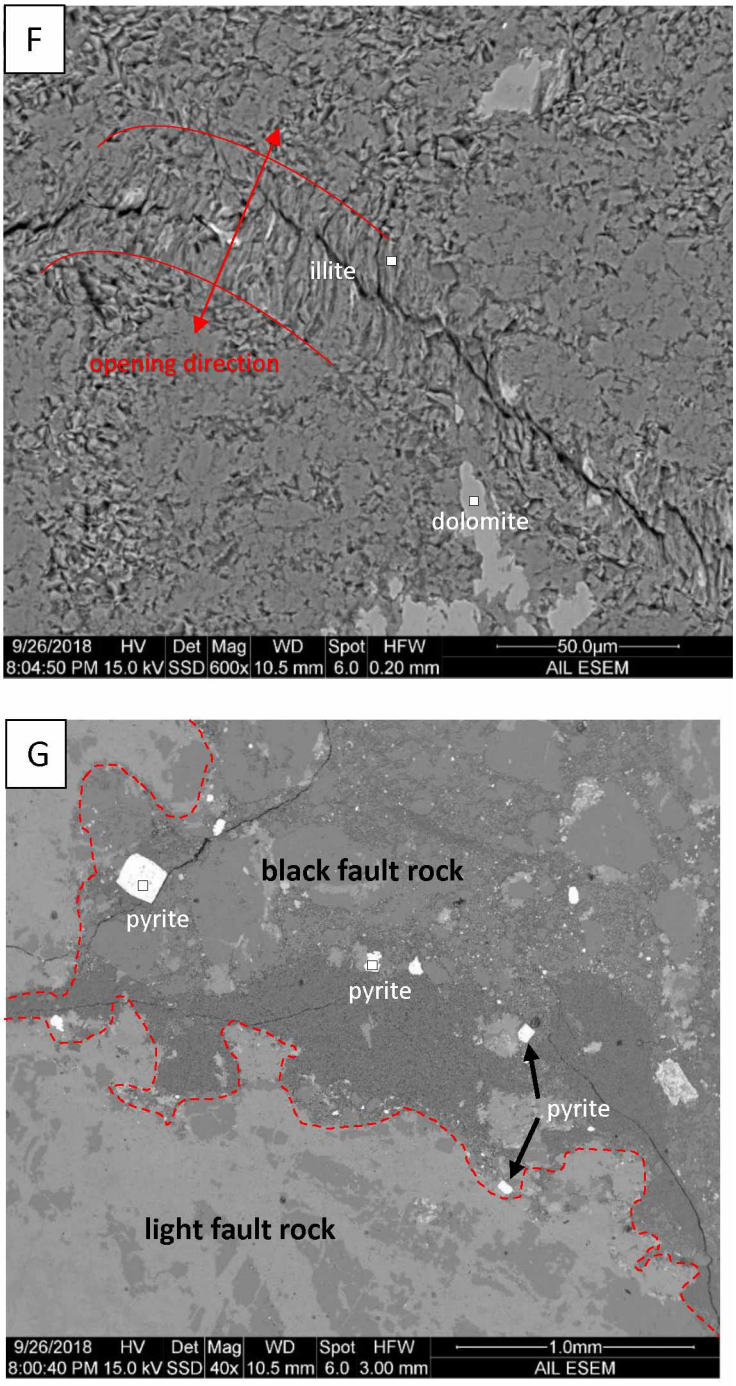

Figure 10 (continued): *(F) Preferentially oriented illite crystals along a fracture opening in black fault rock; extent of illite growth and fracture opening directions are outlined in red; sample 170801-5. (G) Cross-cutting relationship between the light and black fault rock. Red dashed line represents approximate contact between black and light fault-rock; sample 170801-5.*

4.4 Crystallographic Characterization with EBSD

4.4.1 McHugh Complex chert (sample 170915-2)

EBSD software indexed quartz as the most abundant phase in the areas I preselected for potential ductile deformation (Figure 11A). The dominant grain size is <10 μm. Grain shape is rounded and equant and the grain boundaries are slightly irregular. The fine quartz grains are crosscut by linear domains of larger elongate quartz (>15 μm diameter) with irregular boundaries. The orientation of these domains is oblique to the long side of the map (which is parallel to the foliation). The coarser-grained quartz exhibits well-developed subgrains, but they are nearly absent in the finer quartz. The average intragrain misorientation EBSD maps (Figure 9B) show that there is little crystal distortion in this sample, with more of it in the coarser-grained than in the fine-grained quartz. Quartz grain orientations (Figure 11C and 11D) show effectively no crystallographic preferred orientation (CPO), again indicating strain is absent in this sample.

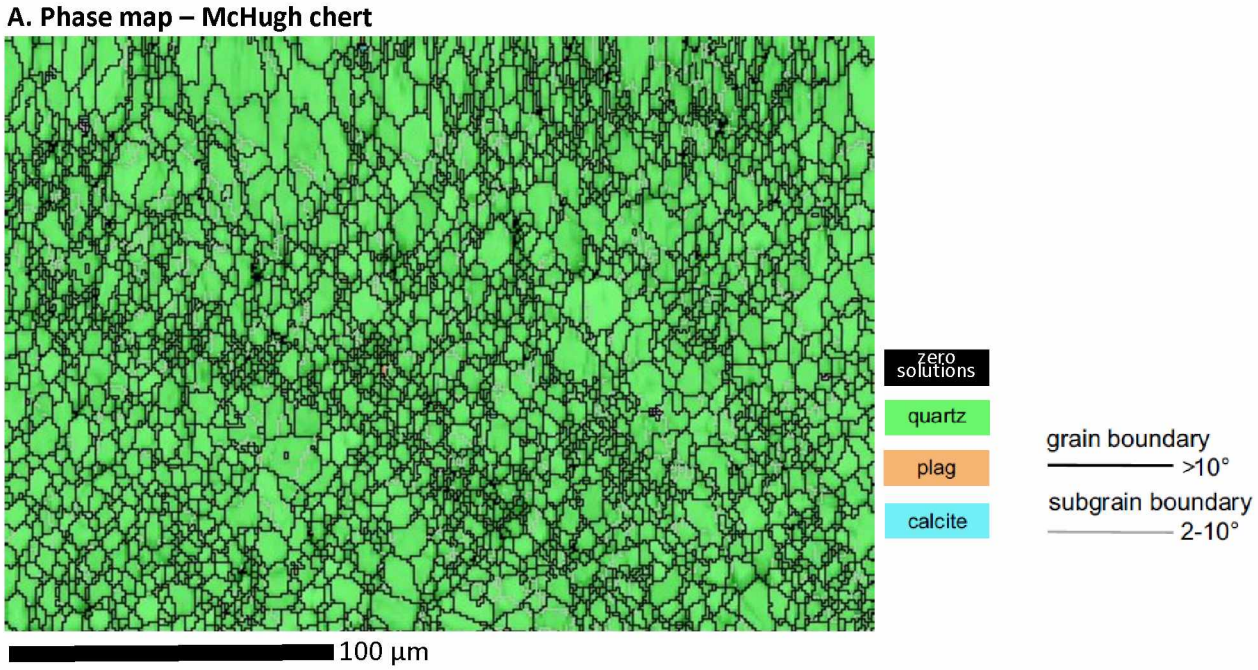

Figure 11: *EBSD maps and pole figures from sample 170915-2 from McHugh Complex chert. All maps are layered on band contrast maps. (A) Phase map showing minerals present.*

B. Quartz average intragrain misorientation map

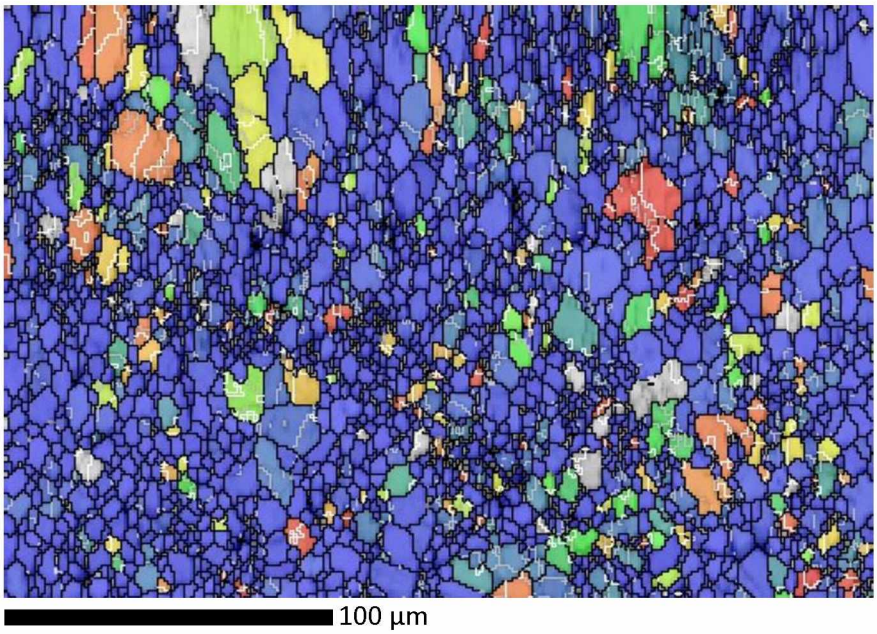

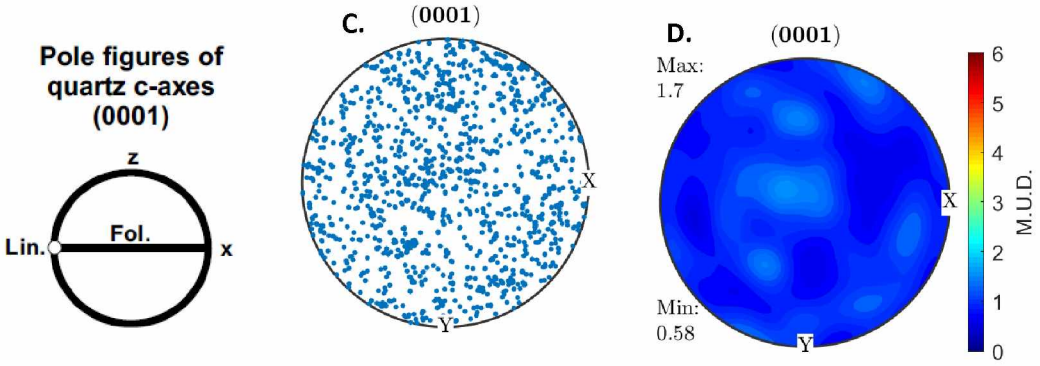

Figure 11 (continued): *(B) Average internal misorientation map of quartz grains. (C) Scatter plot pole figure of quartz c-axes. (D) Contoured pole figure; M.U.D. = multiples of uniform distribution. All pole figures are in lower hemisphere projection.*

4.4.2 Lighter fault rock (sample 170801-3)

The EBSD phase maps show that quartz is the most abundant phase in the selected clasts (Figure 12A). The clasts are surrounded by fine matrix (<10 µm diameter) consisting mostly of plagioclase, with a plagioclase to quartz ratio of 3:1. The quartz clasts are fractured, with matrix filling in the fracture spaces. The quartz grain size in clasts ranges from 5-30 µm diameter, with predominant grain size <15 µm diameter. Most quartz grains have a subrounded and equant shape, with slightly irregular boundaries. The coarser-grained quartz (>15 µm diameter) exhibits weak elongation and well developed subgrains, which are nearly absent in the finer quartz grains. The average matrix grain size is ~5 µm diameter, with lesser grains reaching 15 µm diameter. The grain shape is rounded and equant, with straight grain boundaries and nearly absent subgrains. The average intragrain misorientation EBSD maps (Figure 12B) show that there is little internal distortion in both the crystal and the matrix. The quartz grain orientations show a weak CPO (Figure 12C and 12D), indicating strain is absent in this sample.

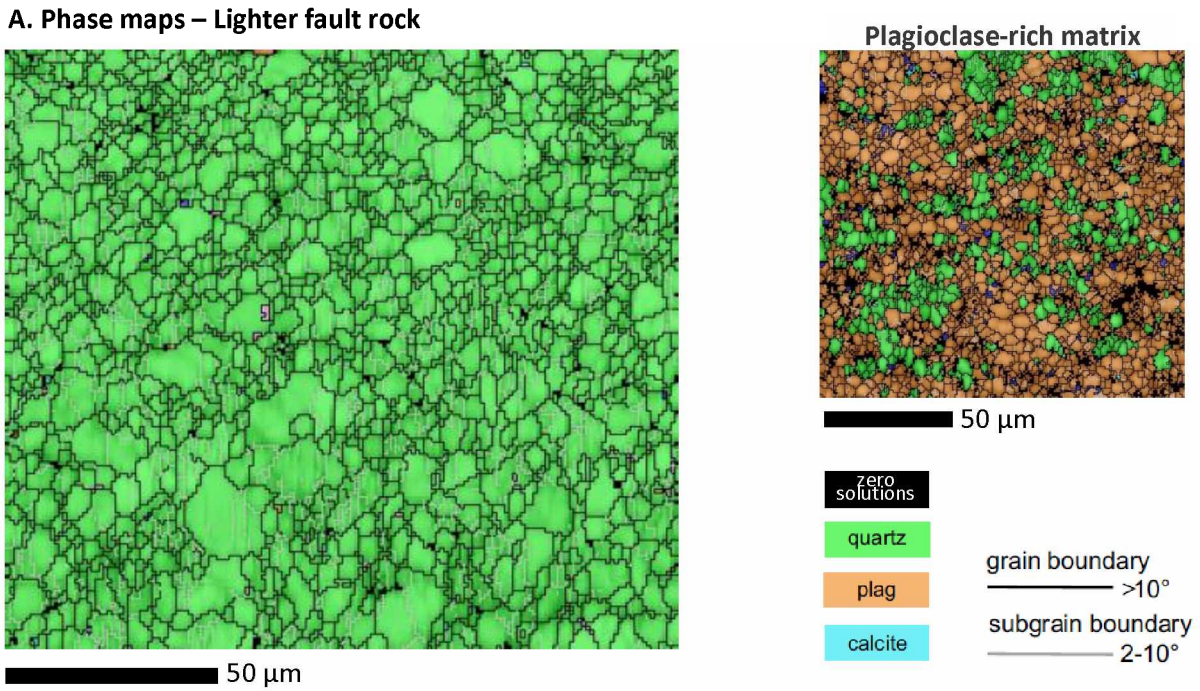

Figure 12: *EBSD maps and pole figures from sample 170801-3 from the fault zone. All maps are layered on band contrast maps. (A) Phase map showing minerals present.*

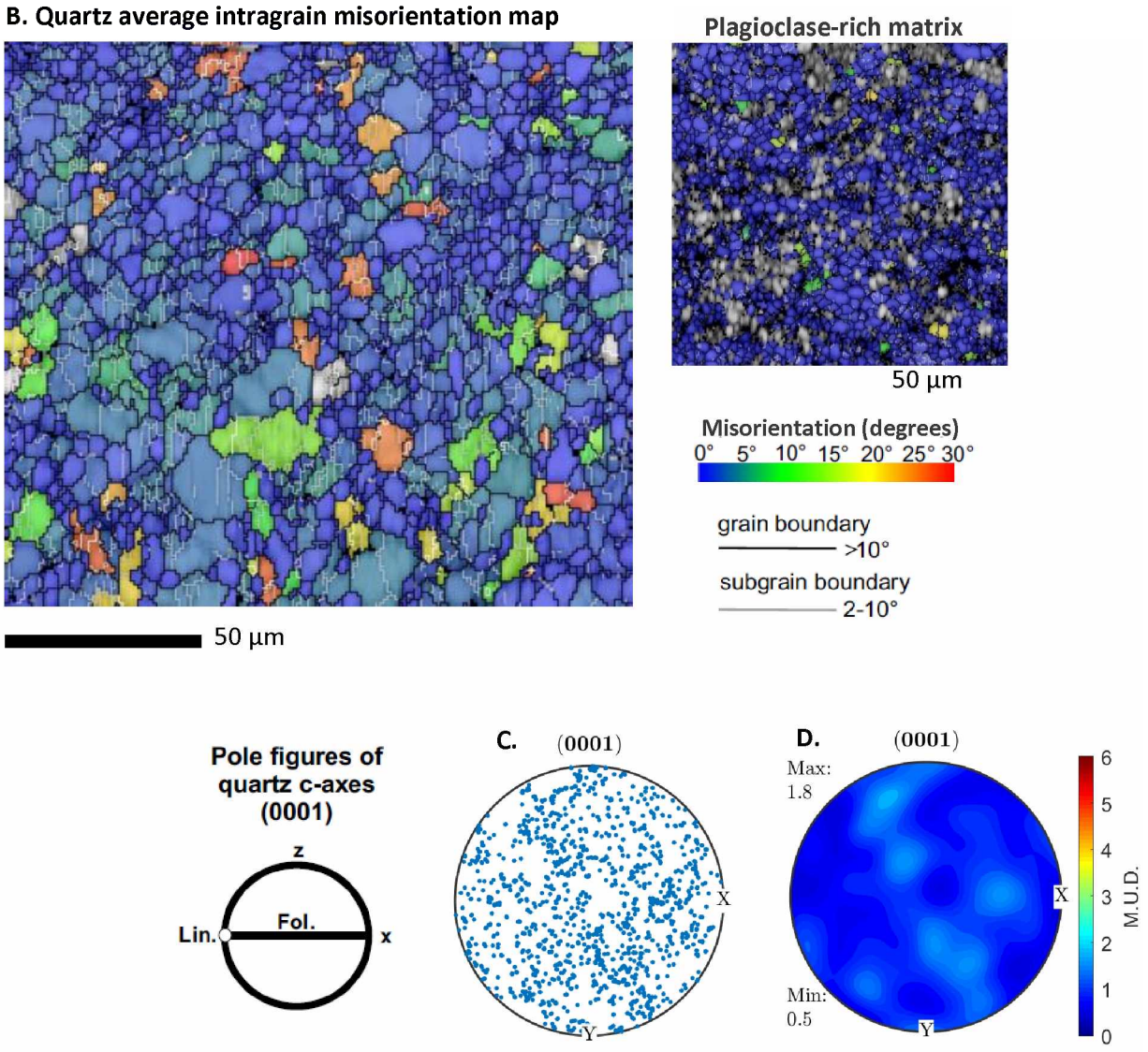

Figure 12 (continued): *(B) Average internal misorientation map of quartz grains. (C) Scatter plot pole figure of quartz c-axes. (D) Contoured pole figure; M.U.D. = multiples of uniform distribution. All pole figures are in lower hemisphere projection.*

4.4.3 Black fault rock (sample 170801-4)

The EBSD phase maps show that quartz is the most abundant phase in the selected clasts which are surrounded by fine dark matrix (Figure 13A). Maps in the matrix detected a limited amount of quartz grains and all other grain pixels were misindexed pixels, which is common when the dominant grain size is less than 1 micron. The quartz grain size in the clasts is predominantly <10 µm diameter. Their shape is rounded and equant with straight grain boundaries. The coarser quartz grains (>15 µm diameter) are arranged in interconnected domains. Their shape is elongate with irregular grain boundaries. The coarser grained quartz exhibits well-developed subgrains, but they are nearly absent in finer quartz. The average intragrain misorientation EBSD maps (Figure 13B) show that there is little crystal distortion in this sample, concentrated in the coarser grained quartz. The quartz clasts are crosscut by carbonate veins and brittle fractures filled with misindexed pixels, characteristic of the dark matrix. The quartz grain orientations (Figure 13C and 13D) show a weak CPO, indicating strain is absent in this sample.

A. Phase map – black fault rock

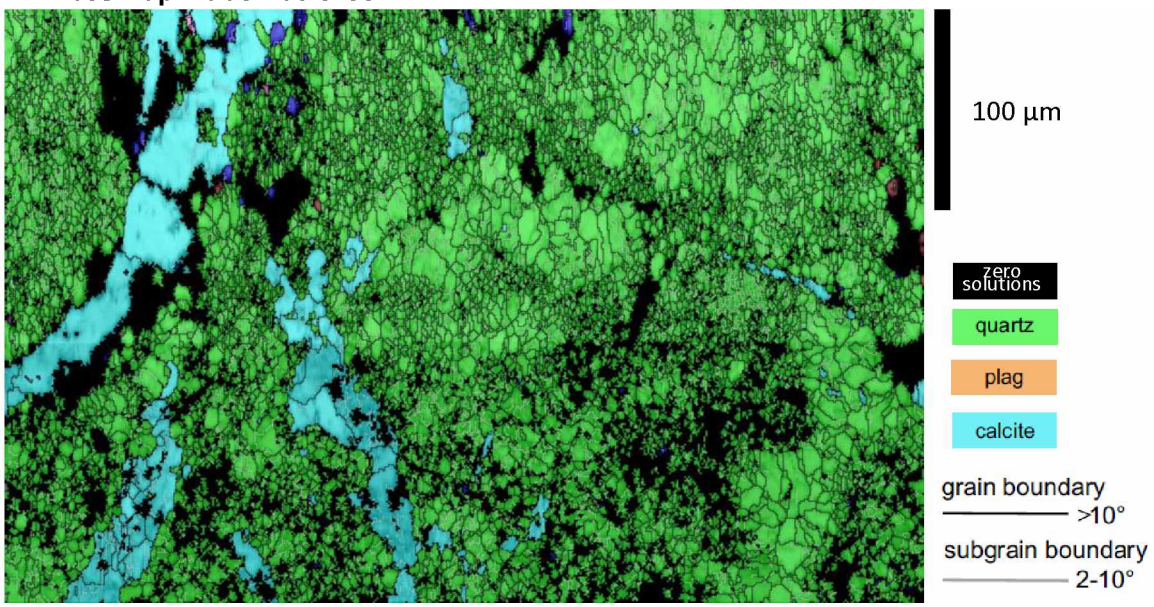

Figure 13: *EBSD maps and pole figures from sample 170801-4 from the fault zone. All maps are layered on band contrast maps. (A) Phase map showing minerals present.*

B. Quartz average intragrain misorientation map

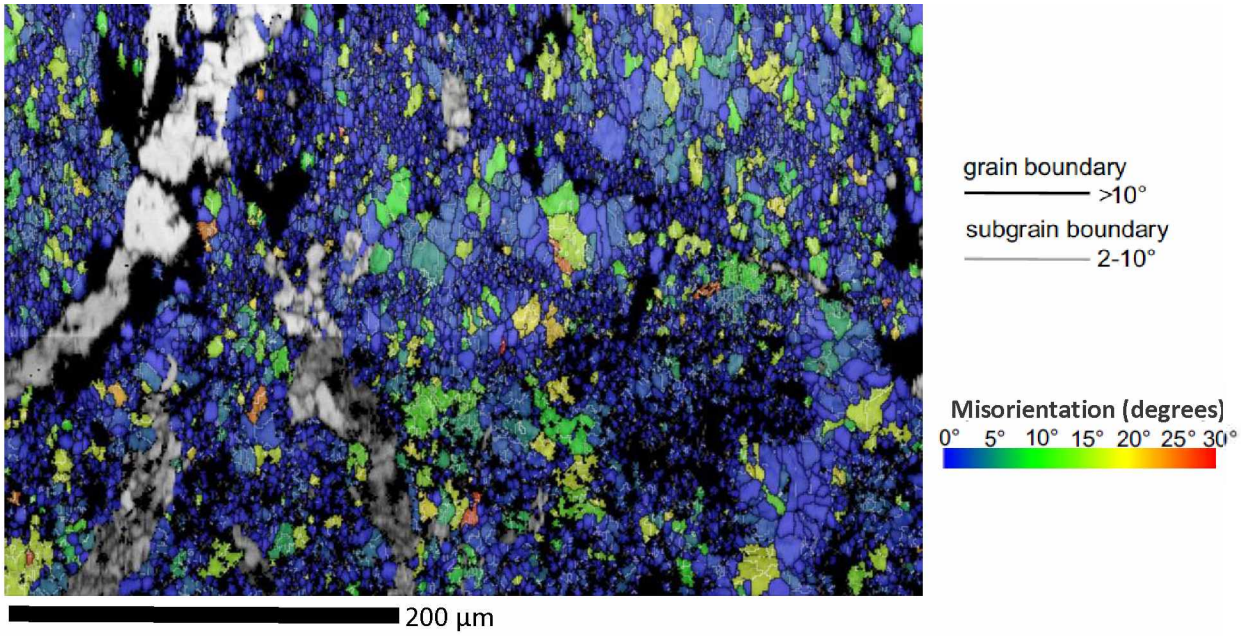

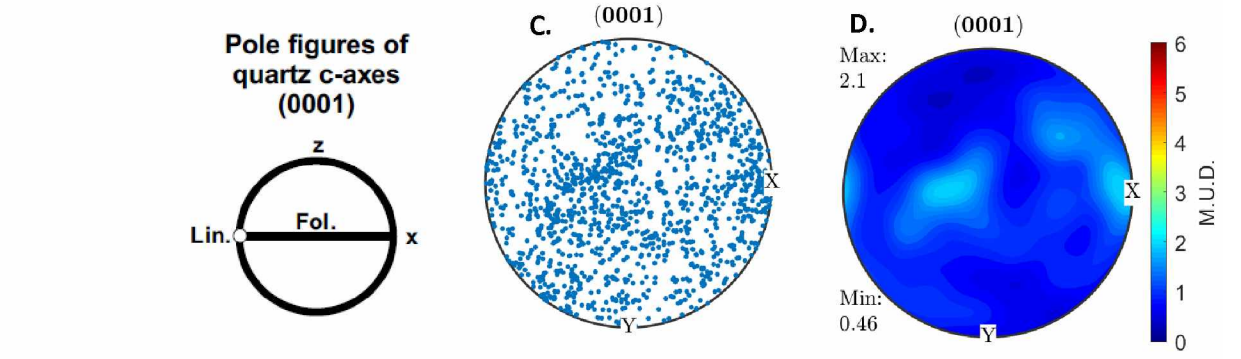

Figure 13 (continued): *(B) Average internal misorientation map of quartz grains. (C) Scatter plot pole figure of quartz c-axes. (D) Contoured pole figure; M.U.D. = multiples of uniform distribution. All pole figures are in lower hemisphere projection.*

4.4.4 Quartz-rich fault rock (sample 170801-9)

The EBSD phase maps show that quartz is the most abundant phase in the selected areas (Figure 14A). The dominant grain size is <15 µm, with localized grains of up to 100 µm diameter which are associated with remnants of quartz veins. The finer quartz grains are rounded and equant with slightly irregular grain boundaries. The coarser quartz grains (>15 µm diameter) are irregular in shape, contain subgrains, and exhibit local bulging grain boundaries as well as newly formed fine grains bounding them. The average intragrain misorientation EBSD maps (Figure 14B) show that there is significantly more crystal lattice distortion in coarse-grained quartz compared to fine-grained quartz. The coarse quartz grains are weakly interconnected, with finer quartz grains and subgrains forming along the rim of the coarse crystals. Four-grain junctions are present in the fine-grained quartz as well as between quartz grains and subgrains. The quartz grain orientations in the quartz-rich fault rock define a moderate CPO (Figure 14C and 14D), indicating the presence of strain in this sample. There is one distorted girdle with maximum of c axes (plotted as [0001]) oriented ~30° clockwise from the pole to foliation.

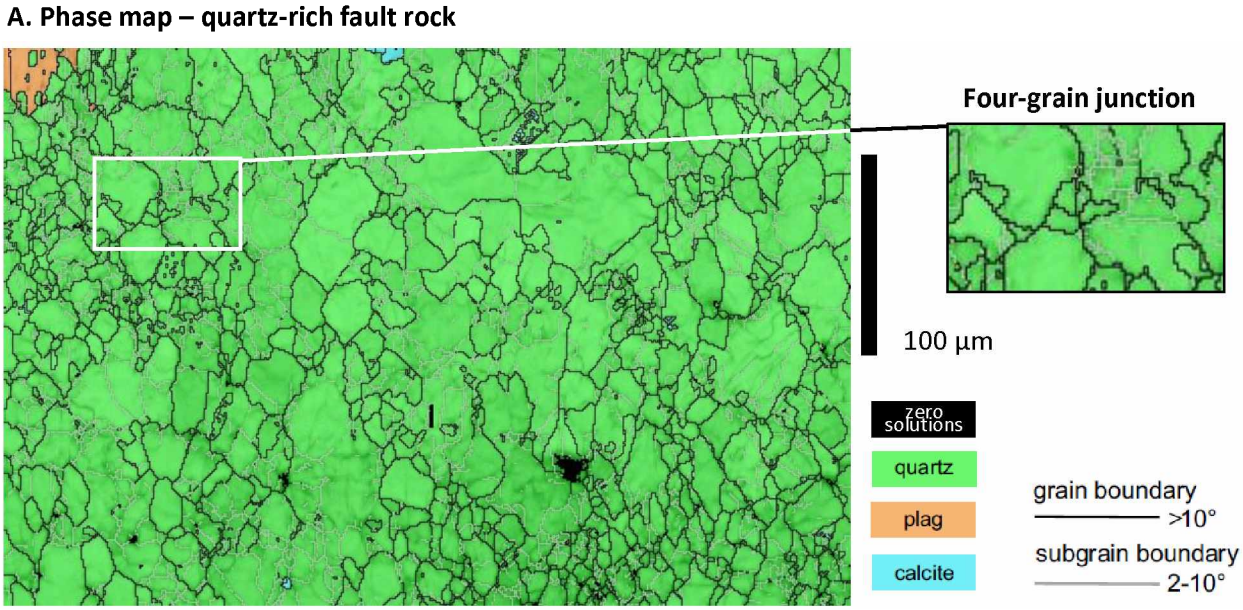

Figure 14: *EBSD maps and pole figures from sample 170801-9 from the fault zone. All maps are layered on band contrast maps. (A) Phase map showing minerals present.*

B. Quartz average intragrain misorientation map

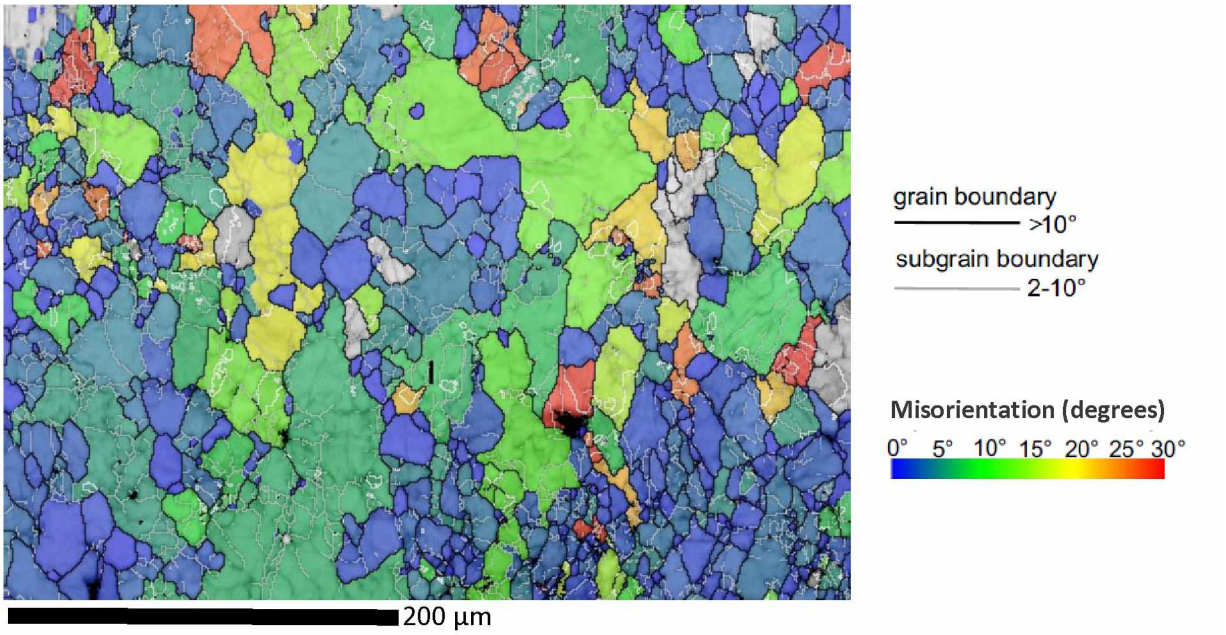

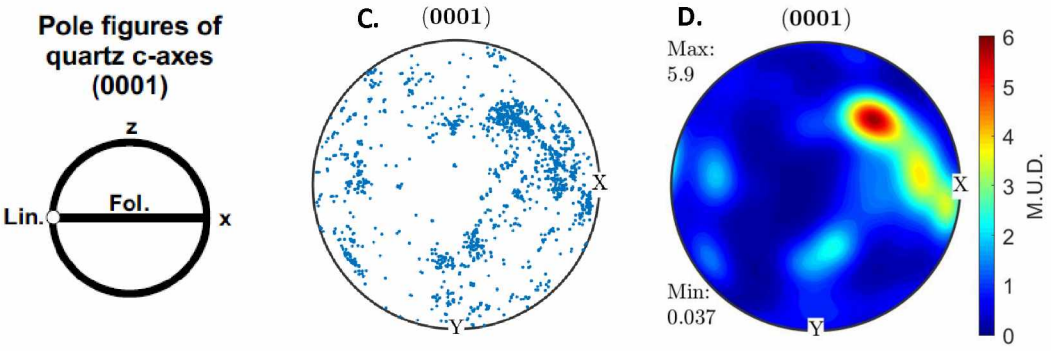

Figure 14 (continued): *(B) Average internal misorientation map of quartz grains. (C) Scatter plot pole figure of quartz c-axes. (D) Contoured pole figure; M.U.D. = multiples of uniform distribution. All pole figures are in lower hemisphere projection.*

4.4.5 Valdez Group (sample 170802-1)

The EBSD phase maps show that quartz is the most abundant phase in the veins cross cutting a matrix rich in plagioclase (Figure 15A). The grain size of the vein quartz ranges from 20 – 100 μm diameter. Their shape is elongate with a preferred orientation parallel to vein opening direction. They have irregular grain boundaries and well developed subgrains. Plagioclase grains in the matrix are finer than the vein quartz, with a predominant diameter of <20 μm. They have a strong elongate shape with a preferred orientation parallel to the foliation. Their grain boundaries are straight and subgrains are almost absent. The average intragrain misorientation EBSD maps (Figure 15B) show that there is little crystal distortion in the plagioclase grains, with more of it in the coarser-grained vein quartz. The plagioclase-rich matrix exhibits domains of misindexed pixels, most likely due to interlayering with crystals smaller than 1 μm diameter. The quartz grain orientations in the quartz-rich veins define a strong CPO (Figure 15C and 15D). There are two girdles with maximum of c axes (plotted as [0001]) oriented ~90° and 45° counterclockwise from the pole to foliation. This reflects the geometry of crystal growth during the continuous opening of a vein.

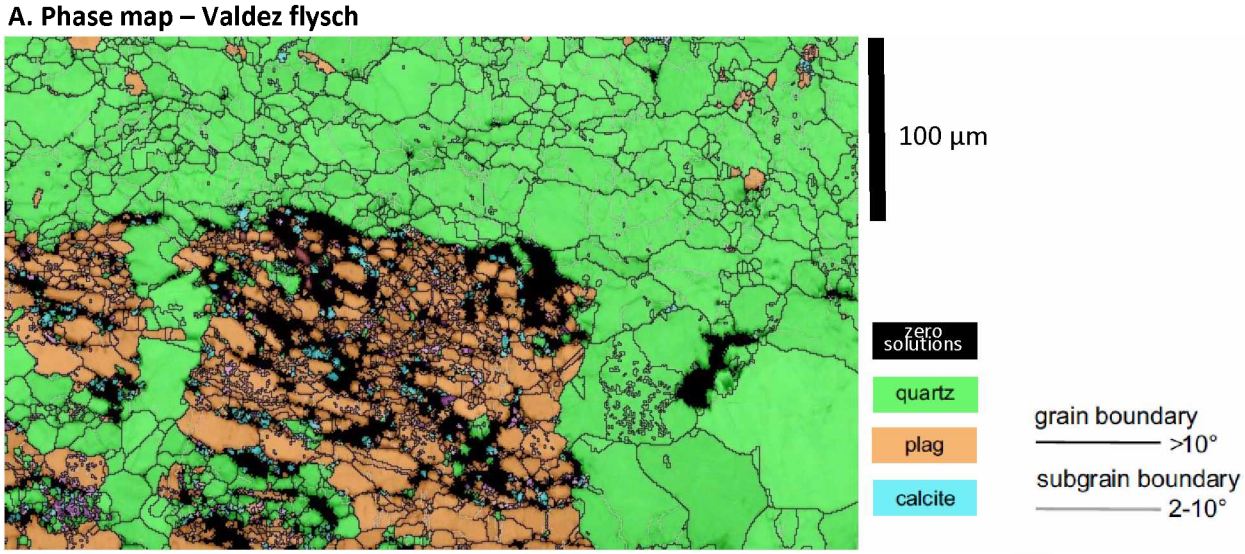

Figure 15: *EBSD maps and pole figures from sample 170802-1 from Valdez Group. All maps are layered on band contrast maps. (A) Phase map showing minerals present.*

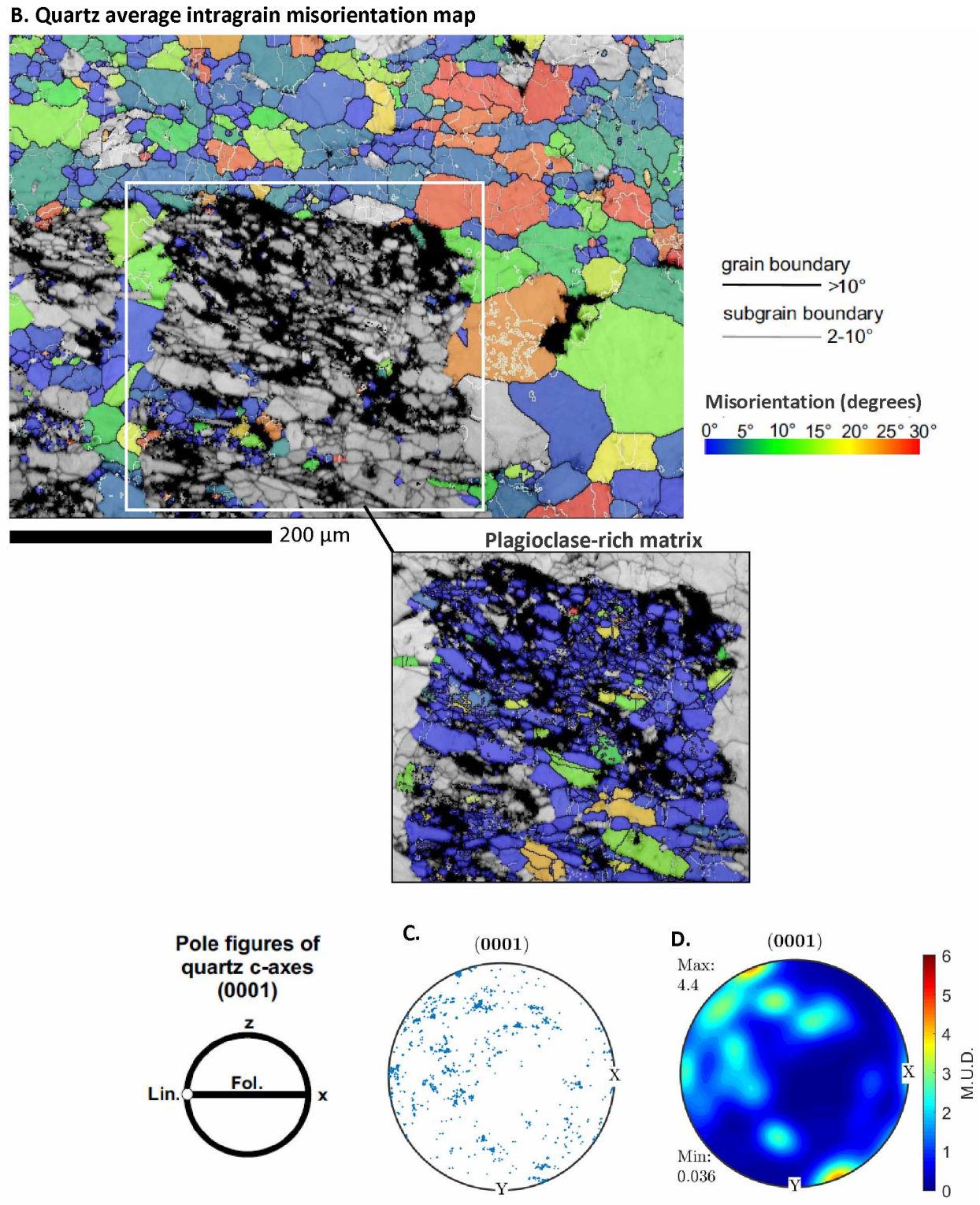

Figure 15 (continued): *(B) Average internal misorientation map of quartz grains. (C) Scatter plot pole figure of quartz c-axes. (D) Contoured pole figure; M.U.D. = multiples of uniform distribution. All pole figures are in lower hemisphere projection.*

4.5 SPO Analysis

The SPO analysis, showed a consistent trend of 80-100 degrees between the long axis of the grain ellipses and the foliation on all maps. A similar trend in orientation is observed after the maps were indexed and analyzed with the image processing software. The results from the MTEX calculations and the image processing can be compared in Figure 16.

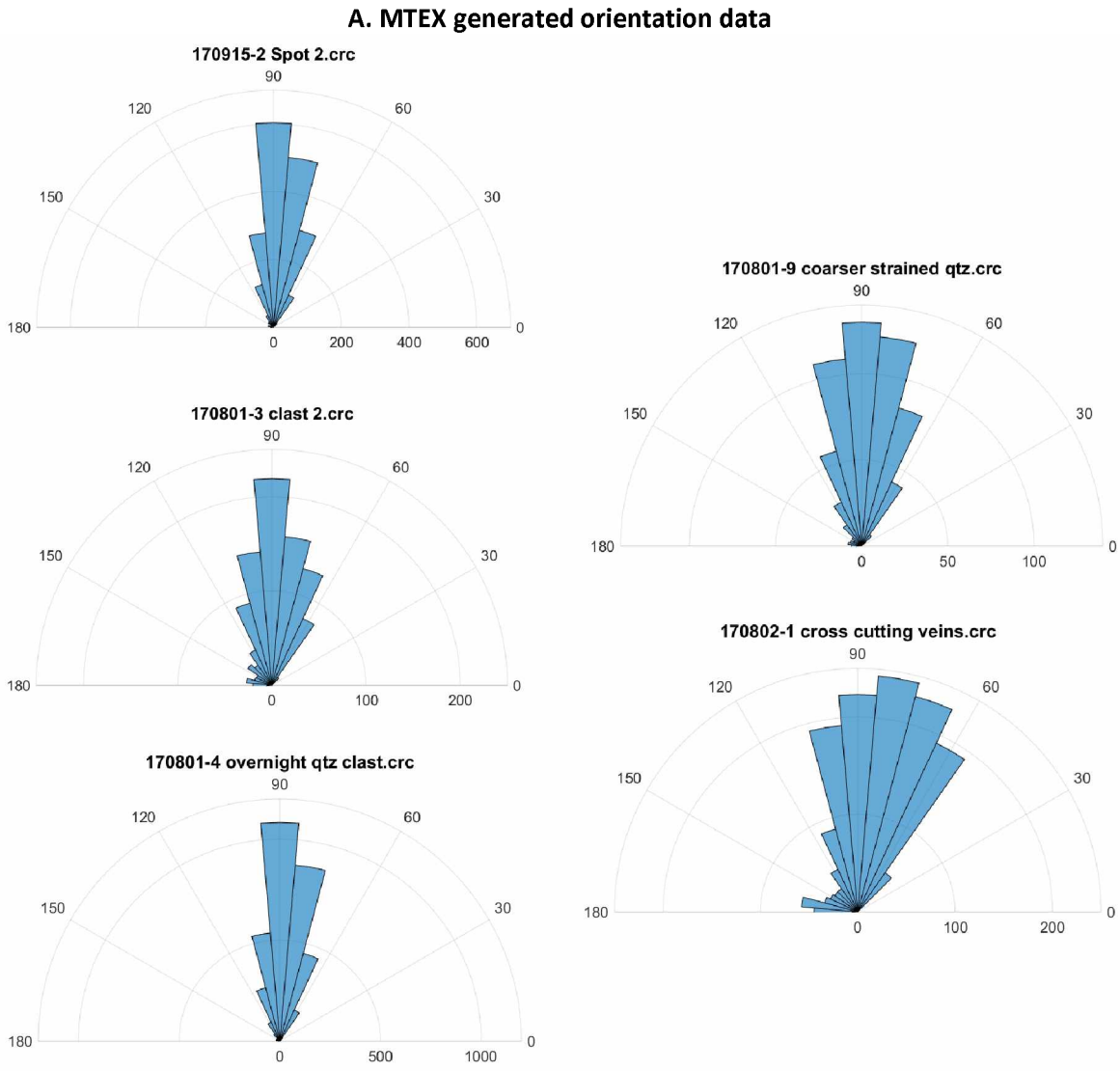

Figure 16: *Orientation plots of long axes of quartz clast ellipses. Titles correspond to the EBSD map used to generate the plots. (A) Rose diagram generated in Matlab; number of orientations on x-axis.*

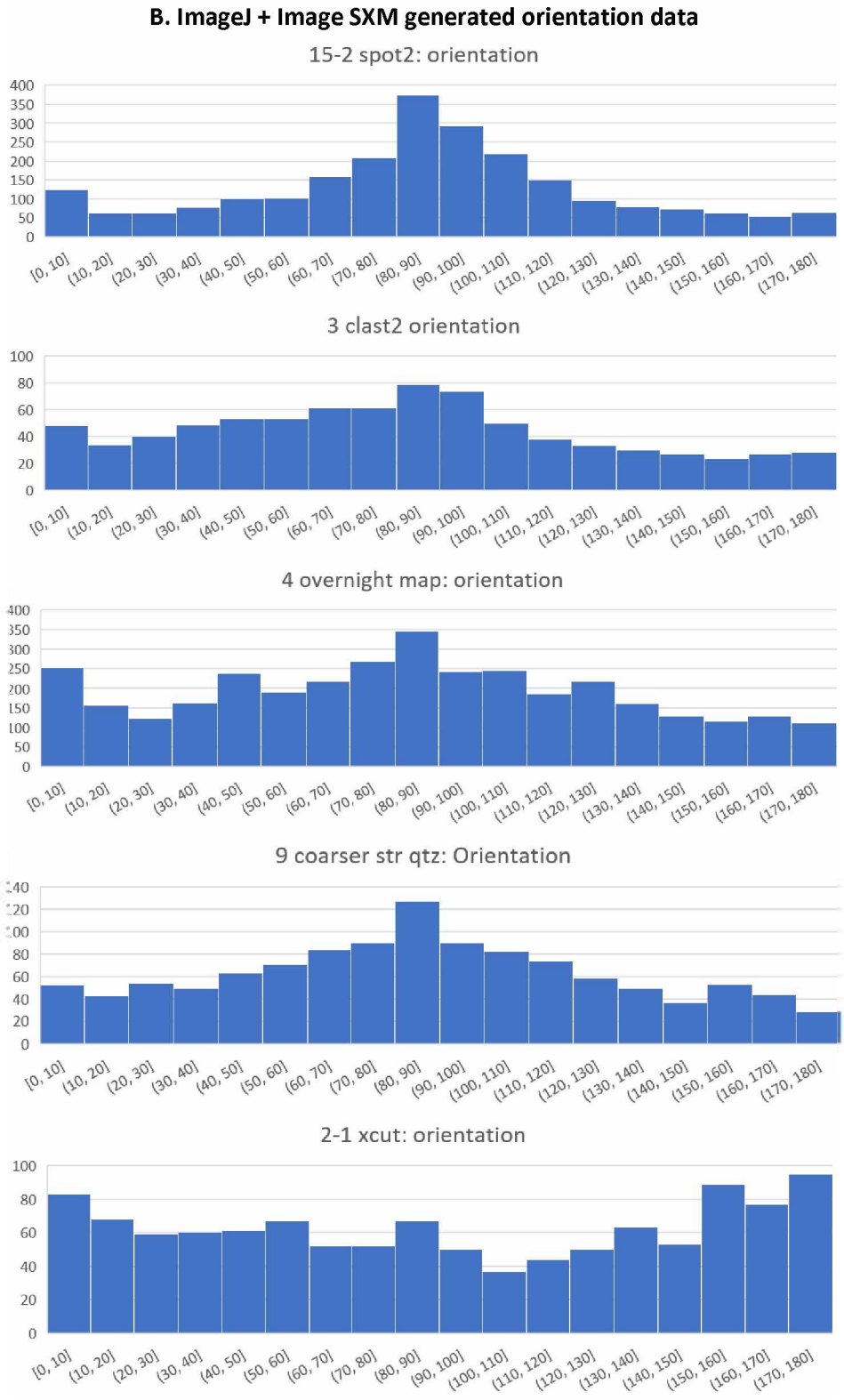

Figure 16 (continued): *(B) Histograms generated in Excel; orientation in degrees on x-axis, number of orientations on y-axis.*

4.6 Crystallographic orientation of clay minerals

The quantitative crystallographic preferred orientation analysis of phyllosilicates was performed on two samples: 170801-5w and 170801-5b, representing the lighter and black fault-rocks respectively. Orientation patterns for the phyllosilicate minerals in both rocks are different from each other. The pole figure for the most abundant phyllosilicate in 170801-5w (kaolinite, Figure 15A) shows a very strong fabric with maxima of up to 7 m.u.d. In sample 170801-5b, where illite is most dominant, clay fabric orientation is more isotropic than in 170801-5w (with maxima up to 3 m.u.d.; Figure 17B).

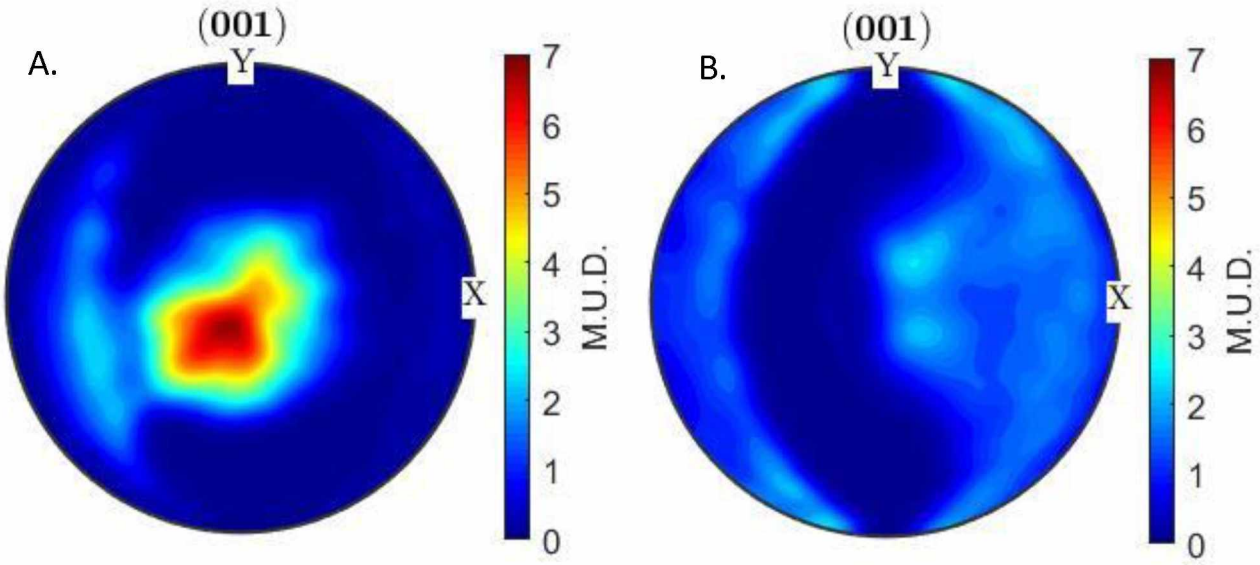

Figure 17: *Contoured pole figures of phyllosilicates. (A) Light fault-rock kaolinite orientations; sample 170801-5. (B) Black fault-rock illite orientations; sample 170801-4.*

4.7 Geochemistry and mineralogy

The whole-rock geochemical composition differs between the black and light variations of the fault rock (Figure 18 and Table 2 for XRF analysis results). For major elements, I observe a significant increase in CaO, which is 2 to 4 times higher in black than in light fault-rocks. K_2O content is remarkably higher in black fault-rocks, with an increase from 300% up to over 1,500%. TiO_2 and Na_2O are systematically lower in the black than in the light fault-rocks, with a decrease ranging from 30% to 85% and 60% to 100%, respectively. LOI is generally lower in the black fault rocks. The black fault-rock samples have a less homogeneous composition compared to the light fault rock. Sample 170801-5B is especially peculiar, with an SiO_2 content of 28.6 wt%, which is 40% lower than the other black fault-rock sample. The other notable differences are in the CaO content and LOI, with 40% increase in CaO and 36% increase in weight lost during ignition.

Black fault rocks and light fault-rocks have similar mineralogy. According to the X-ray diffraction patterns, light fault-rock mineralogy across the damage zone is more uniform than that of black fault-rock. The most common minerals are quartz, plagioclase (albite), carbonate (dolomite), illite and kaolinite. Sample, 170801-5B differs from the rest with its absence of plagioclase and kaolinite. Pyrite is present only in the black-fault rock, making up ~4% of its mineralogy. Less than 3% of smectite is detected only in the light-fault rock. The proportion of each mineral persent is reported in Table 3.

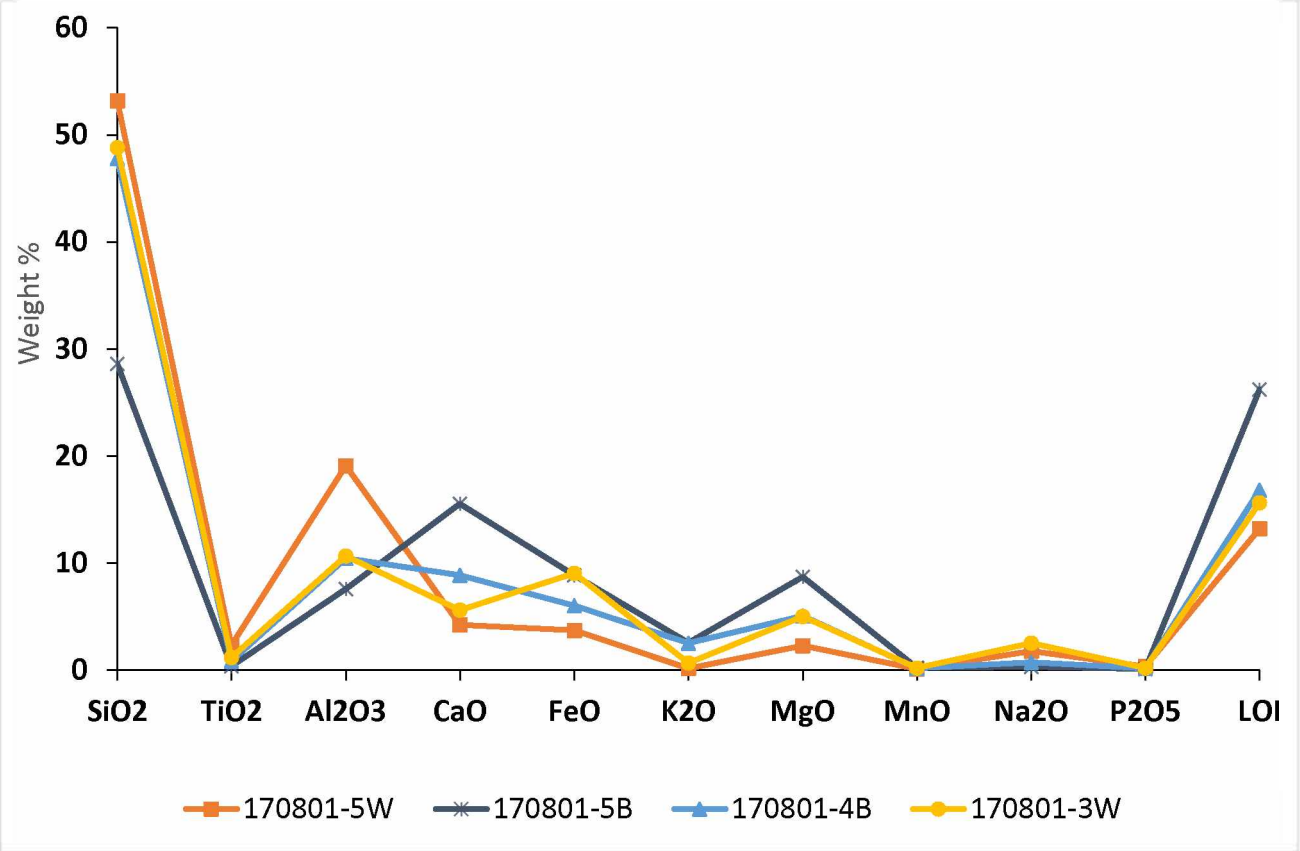

Figure 18: *X-ray fluorescence analytical data: major oxide weight percent in black and light fault rock. Different samples are indicated with a different color of the graph.*

Table 2*: Major oxide compositions of black and light fault rocks*

	170801-5W	170801-5B	170801-4B	170801-3W
SiO2	53.2	28.6	47.8	48.8
TiO2	2.3	0.3	0.8	1.2
Al2O3	19.1	7.6	10.4	10.6
CaO	4.2	15.5	8.9	5.6
FeO	3.7	8.8	6	9
K2O	0.2	2.5	2.5	0.6
MgO	2.3	8.7	5.1	5
MnO	0.1	0.2	0.2	0.2
Na2O	1.8	0.3	0.7	2.5
P2O5	0.3	0.1	0.2	0.2
LOI	13.2	26.2	16.8	15.6
Total	100.3	98.9	99.3	99.3

Note: Analyses of major elements are expressed in wt%. LOI - Loss On Ignition. Black fault-rocks have a "B" attached to the sample number (ex: *170801-4B*). Light fault-rocks have a "W" attached to sample number (ex: *170801-5W*).

***Table 3**: Quantitative X-ray diffraction results*

	170801-3W	170801-4B	170801-5B	170801-5W
Quartz	24%	33%	12%	30%
Albite	30%	6%	-	20%
Carbonate	36%	38%	64%	15%
Illite	<3%	16%	20%	<3%
Kaolinite	8%	3%	-	30%
Pyrite	-	3%	4%	-
Smectite	3%	-	-	<3%
Total	100%	100%	100%	100%

4.8 Raman spectra

Spectra from 3 different sites within black fault-rock sample 170801-4 show very small variations between sites (Figure 19). Table 4 summarizes the results of peak deconvolution for all sites. For each parameter - G band position, G band width, D1/G peak intensity ratio (R1) and D1/(G + D1 + D2) peak area ratio (R2 ratio) - the mean value obtained for several spot analyses within a given site is reported. Their respective low standard deviation values suggest the sample is structurally heterogeneous. All R2 ratios fall between 0.68 and 0.72 which correspond to a peak metamorphic temperature of ~300 – 350 °C (Figure 20).

Table 4: *Raman spectra peak deconvolution results*

Site	G position	G width	R1 ratio	R2 ratio
EN_170814_CC_site1	1572.05	28.52	7.89	0.72
EN_170814_CC_site1	1575.95	34.45	6.78	0.69
EN_170814_CC_site1	1577.20	32.07	6.72	0.71
EN_170814_CC_site1	1575.02	34.85	6.81	0.72
EN_170814_CC_site1	1574.26	27.60	7.72	0.71
EN_170814_CC_site1	1574.79	30.17	8.42	0.72
EN_170814_CC_site2	1575.64	34.09	6.38	0.71
EN_170814_CC_site2	1576.80	38.36	7.85	0.72
EN_170814_CC_site2	1574.23	38.55	7.06	0.72
EN_170814_CC_site2	1573.22	34.91	6.37	0.71
EN_170814_CC_site2	1572.68	27.51	9.41	0.72
EN_170814_CC_site3	1575.50	39.29	6.00	0.69
EN_170814_CC_site3	1574.40	30.24	6.74	0.72
EN_170814_CC_site3	1575.45	32.55	7.18	0.70
EN_170814_CC_site3	1577.97	45.38	5.05	0.68
EN_170814_CC_site3	1574.92	35.76	7.14	0.70
EN_170814_CC_site3	1575.67	31.40	6.83	0.71
EN_170814_CC_site3	1575.84	33.46	6.09	0.70
Standard deviation	1.46	4.45	0.96	0.01

Note: G position – peak 5 position, G FWHM – peak 5 full width at half maximum, R1 = D1/G ratio of peak heights, R2 = D1/(G + D1 + D2) ratio of peak areas. D1 – peak 1, D2 – peak 2.

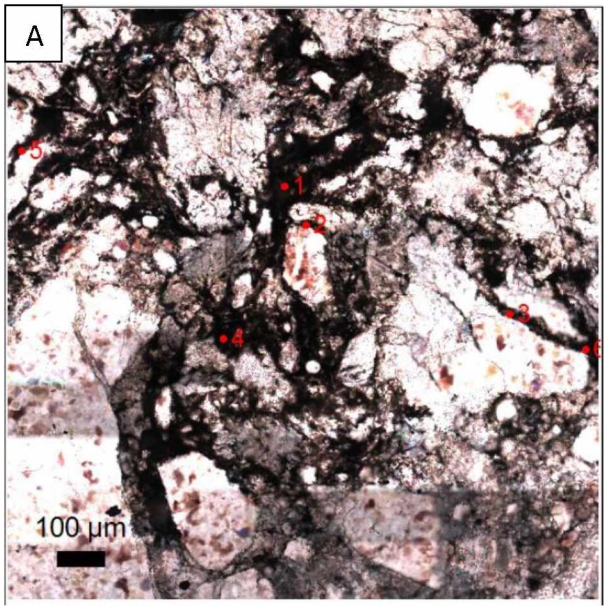

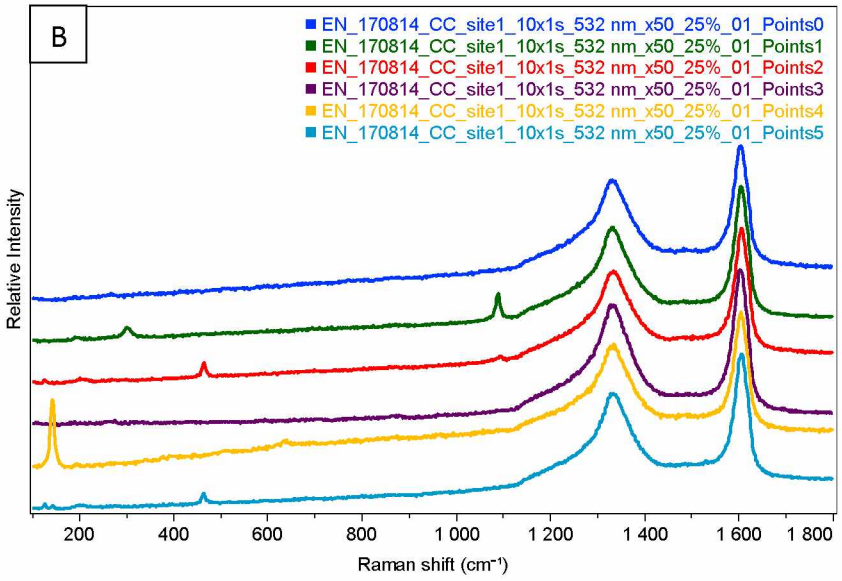

Figure 19: *Raman microscopy site images and spectra. (A) Points analyzed with Raman spectroscopy at Site 1, Sample 170801-4. (B) Corresponding Raman spectra.*

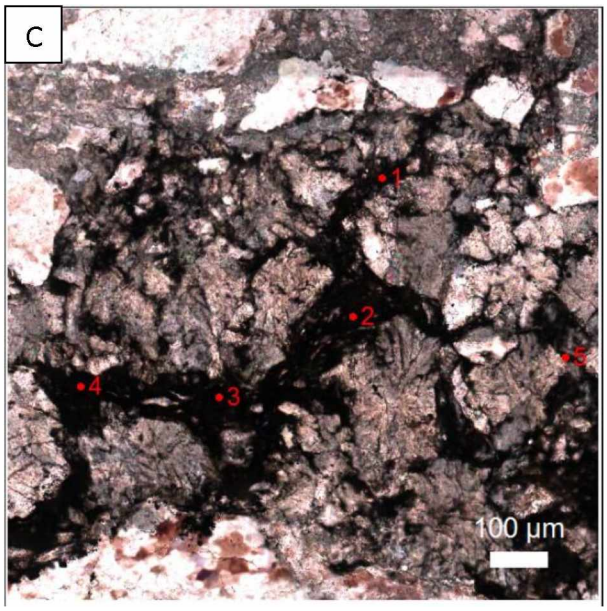

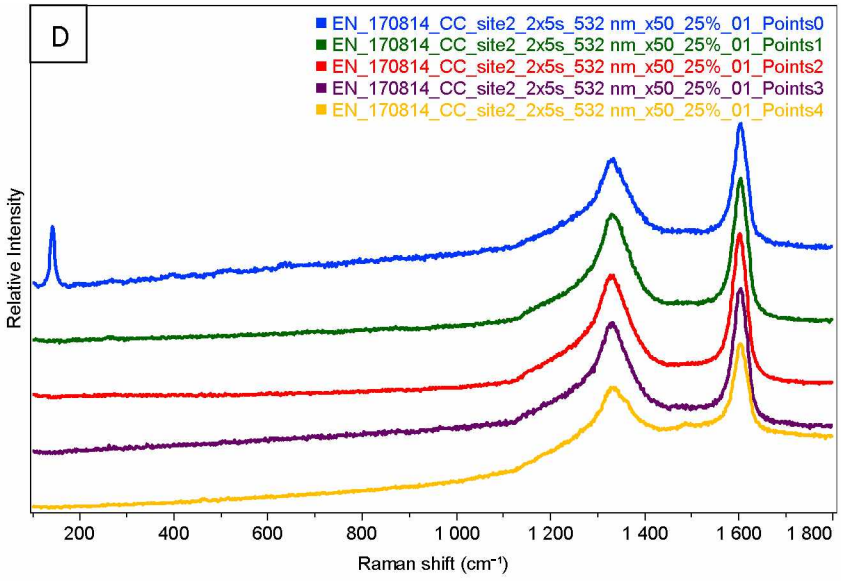

Figure 19 (continued): *(C) Points analyzed with Raman spectroscopy at Site 2, Sample 170801-4. (D) Corresponding Raman spectra.*

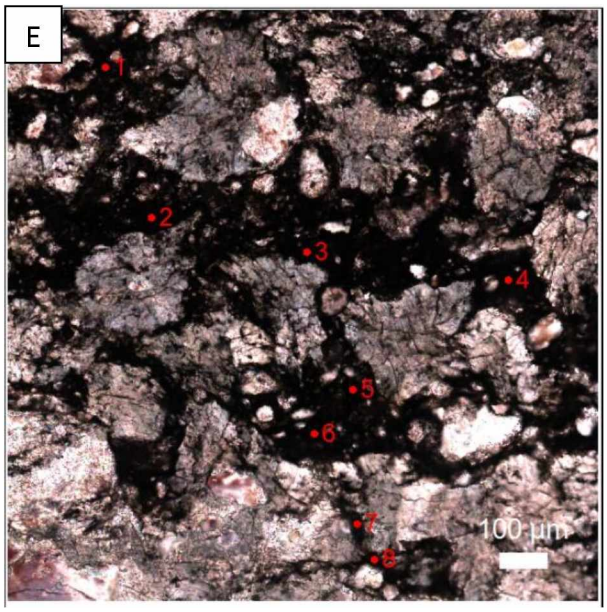

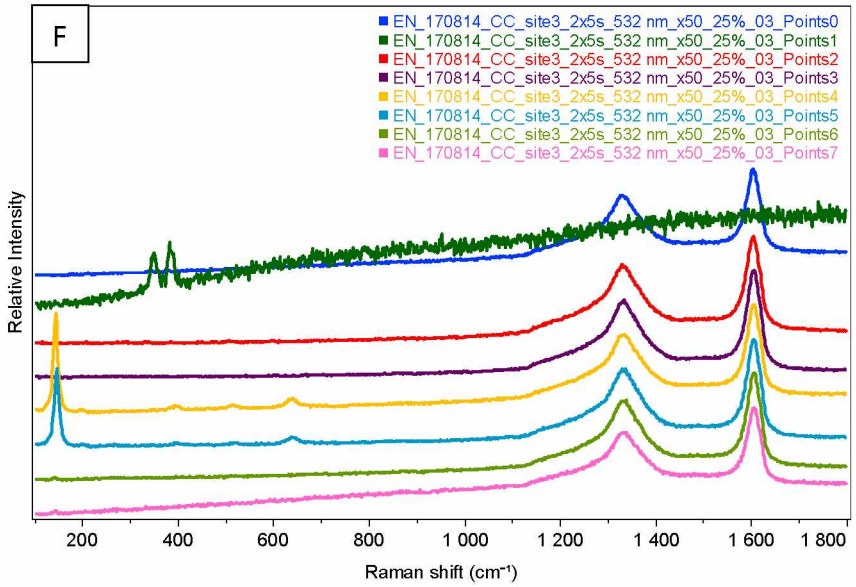

Figure 19 (continued): *(E) Points analyzed with Raman spectroscopy at Site 3, Sample 170801-4. (F) Corresponding Raman spectra.*

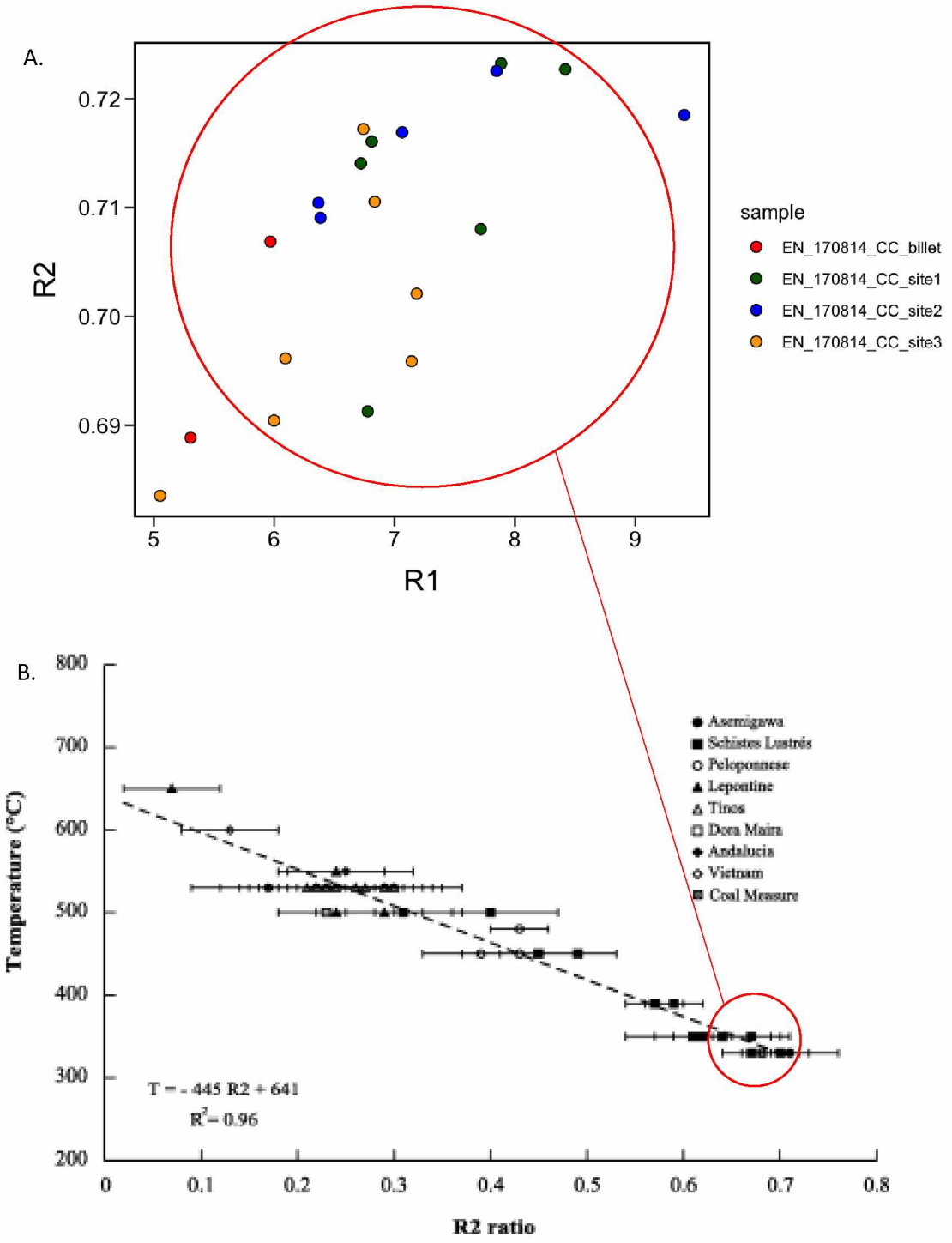

Figure 20: *Raman spectra relationship to temperature. (A) Plot of D1/G peak intensity ratio (R1) vs. D1/ (G + D1 + D2) peak area ratio (R2 ratio). (B) R2 ratio relationship to maximum metamorphic temperature (from Beyssac et al., 2002).*

4.9 $^{40}Ar/^{39}Ar$ step-heating

Sample 170801-4 is a black fault-rock made up of quartz and potassium feldspar clasts surrounded by fine carbonate-quartz matrix (Figure 21C). Illite defines a weak fabric and forms pressure shadows (tails) around quartz and feldspar clasts. The K-feldspar stretched and fractured, with no intracrystalline deformation observed. The initial whole-rock argon analysis (WR1) yielded a complex spectrum with a plateau age of 160.9 ± 1.2 Ma (Figure 21A). The second whole-rock analysis (WR2) yielded a pattern of ages that increased from a minimum of ~60Ma, jumping to ~110 Ma, ~145Ma and ~170Ma consecutively, at higher temperature steps. The illite yielded a pattern of ages that increased from a minimum of ~40Ma to a flatter segment with maximum apparent ages at ~155Ma (Figure 21B). Potassium feldspar yielded a spectrum dominated by a plateau age at 23.2 ± 1.4 Ma over the initial 75% of cumulative ^{39}Ar released.

Sample 170801-2 is a black fault rock and whole-rock $^{40}Ar/^{39}Ar$ step-heating analysis was performed on the fine dark matrix (Figure 21E) made up of Fe-rich dolomite, quartz, plagioclase, kaolinite and illite. The argon spectrum has a pattern of ages that serially increase from a minimum of ~60 Ma to a plateau age of 114.2 ± 2.2 Ma over the final 40% of cumulative ^{39}Ar released (Figure 21D).

Sample 170801-3 is a light fault rock consisting of fine quartz, carbonate, plagioclase (albite), illite and clays. The illite and clays define a foliation consistent with the general fault zone fabric (Figure 21G). Illite yielded a spectrum dominated by Eocene apparent ages, from a minimum of ~19Ma jumping to ~25Ma in the highest temperature step (Figure 21F).

Sample 170801-8 is a black fault rock with stretched and fractured quartz clasts surrounded by fine dark matrix (Figure 21I) made up of Fe-rich dolomite, quartz, plagioclase, kaolinite and illite. Two whole-rock $^{40}Ar/^{39}Ar$ step-heating analyses were performed (Figure 21H). The first one yielded a complex argon spectrum with a minimum age of ~40 Ma at the

initial low temperature step followed by increasing step segments with maximum apparent ages of ~160 Ma. The second whole-rock analysis yielded a pattern of ages that increased from a minimum of ~20 Ma to a plateau segment at 121.7 ± 2.4 Ma over 55% of the cumulative ^{39}Ar released.

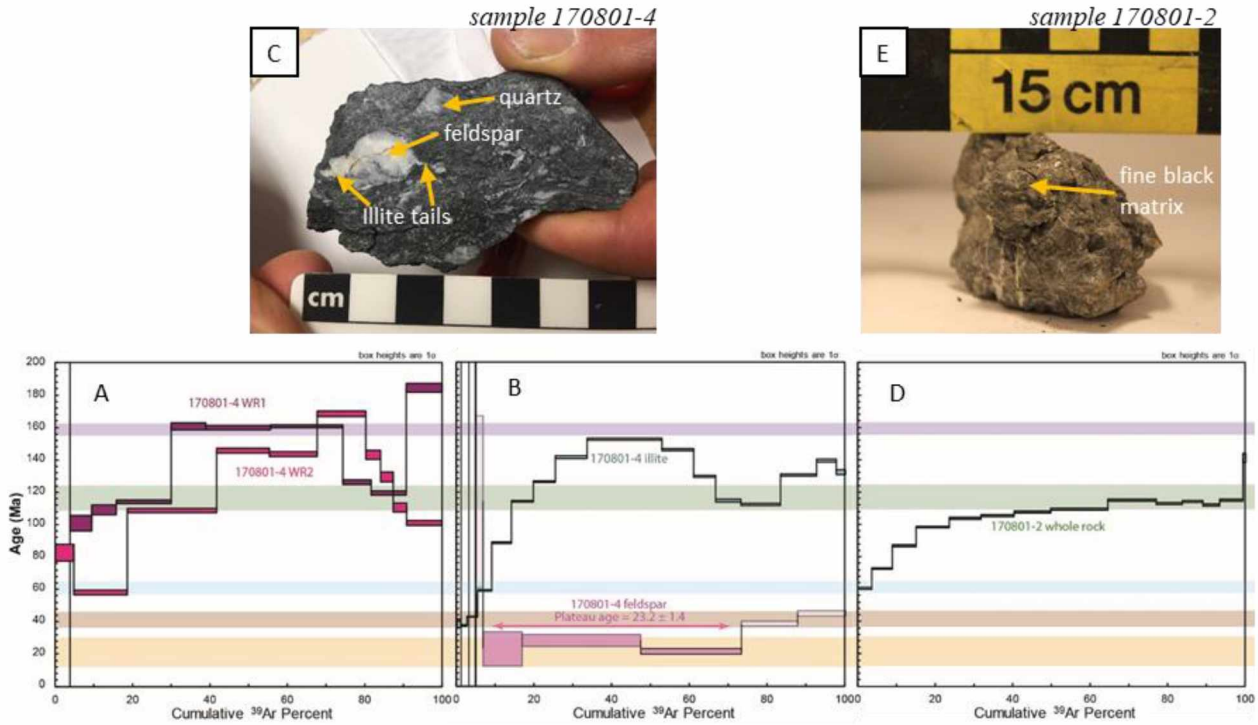

Figure 21: *Argon dating samples and spectra. (A) Whole rock argon spectra for sample 170801-4. (B) Illite and feldspar spectra for sample 170801-4. (C) Hand sample photo of 170801-4. (D) Whole rock spectrum for sample 170801-2. (E) Hand sample photo of 170801-2.*

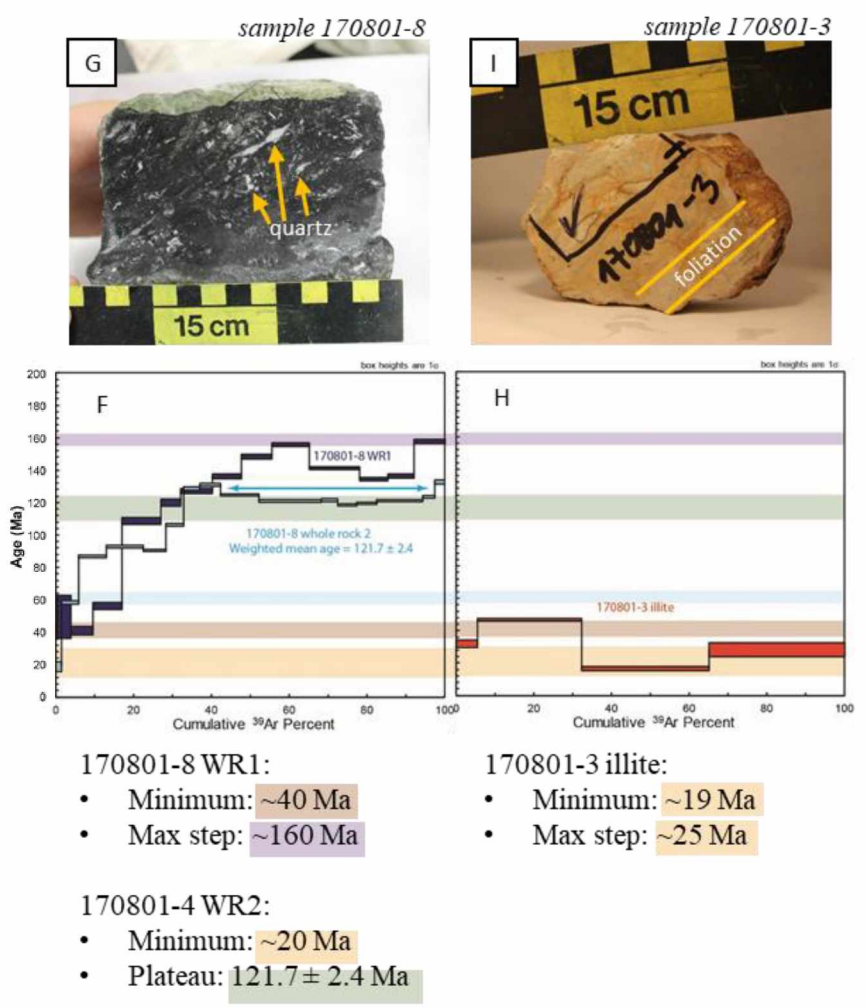

170801-8 WR1:

- Minimum: ~40 Ma
- Max step: ~160 Ma

170801-3 illite:

- Minimum: ~19 Ma
- Max step: ~25 Ma

170801-4 WR2:

- Minimum: ~20 Ma
- Plateau: 121.7 ± 2.4 Ma

Figure 21 (continued): *(F) Illite spectrum for sample 170801-3. (G) Hand sample photo of 170801-3. (H) Whole rock spectra for sample 170801-8. (I) Hand sample photo of 170801-8.*

Chapter 5: Discussion

5.1 McHugh Complex and Valdez Group deposition and deformation

The McHugh Complex in southern Alaska is a discontinuous strip of exposures that narrow from 40 km on the Kenai Peninsula to 1.2 km in my field area. Detrital-zircon studies suggest 2–3 episodes of subduction erosion and 2 episodes of subduction accretion, which could explain the limited extent of this section of the Chugach Accretionary Complex compared to the vastness of the adjacent Valdez Group to the south, whose detrital-zircon record indicates a long stretch of subduction accretion (Figure 1; Amato and Pavlis, 2010; Amato et al. 2013).

In the study area, this section of the McHugh Complex was assigned by Barefoot et al. (2020) to the Potter Creek assemblage of Amato et al. (2013). Across a stretch of ~1.5 km, this assemblage comprises metavolcanics, metasediments, and mesomélange that is described in detail by Barefoot et al. (2020). Of relevance to this study is the incoherent nature of the mélange: Meters-wide blocks of mudstone and chert, sometimes interlayered, lack any coherence or uniformity of bedding or structural orientations. They are likely part of the trench/accretionary wedge stratigraphy that was scraped off the subducting plate and transferred to the overriding upper plate during subduction. Green tuff intermingled with the chert and mudstone likely erupted from the adjacent Talkeetna arc, which is the main component of the Peninsular Terrane (Figure 1) and was deposited with the mélange sediments during accretion (Amato et al., 2013; Barefoot et al., 2020). A 200–250m wide metavolcanics block, which includes a body of pillow lava, is interpreted as a seamount which entered the subduction channel and was incorporated in the accretionary prism of the upper plate (Barefoot et al., 2020). This further enhanced disruption of the blocks in the mélange. Shear planes commonly present at the block boundaries indicate

localized strain, but there is no preferred orientation of either foliation or lineation within the blocks or within the mélange as a whole, regardless of block size or composition (Figure 3B).

In contrast, the adjacent Valdez Group, the most voluminous assemblage in the Chugach Accretionary Complex, is remarkably uniform. While the whole sequence has been metamorphosed, in the study area it is still easy to make out original alternating layers of thin beds of shale with coarser sandstone (Figure 3H). Previous studies agree that the coherence and apparent bedding is indicative of thick, deep-water ocean-plate sediments which were incorporated into the accretionary prism during subduction (e.g. Sample and Reid, 2003; Kochelek et al., 2011; Amato et al., 2013). The assemblage is so vastly uniform that folding and crenulation throughout the meta-shale in its whole extent parallels the strike of the subduction zone mega-thrust, which is the BRF (Figure 3I and 3J; Pavlis and Roeske, 2007). My measurements of foliation in the Valdez flysch in my field site are consistent with measurements in exposures to the south, and west (Kusky et al. 1997).

The age arrays of detrital zircons from the McHugh Complex (180-85 Ma) and the Valdez Group (85-68 Ma) indicate either a very short or absent period of tectonic erosion between deposition of the two (Amato and Pavlis, 2010; Kochelek et al., 2011). However, compositional and structural contrasts imply different depositional environments for the two units. My measurements are consistent with previous studies that interpret McHugh Complex deposition as olistostrome-style, with submarine gravity sliding and slumping deposited the eroded arc sediments directly into the subduction trench (van der Heyden, 1992; Kochelek et al., 2011). The sediment flux likely increased from the Jurassic-Lower Cretaceous to the Upper Cretaceous, which led to filling the trench and allowed for deposition of sediment outboard of the trench (Kochelek et al., 2011). These deep ocean outboard sediments formed the coherently bedded turbidites of the Valdez Group.

The most abundant rock type of the mélange just north of the fault zone is metamorphosed, very fine-grained layered mudstone with quartz-rich clasts and visible pyrite (Figure 3E). At places, the mudstone is interlayered with chert and green tuff (Figure 3A). These rock types of the McHugh Complex are present in the damage zone of the fault (Figure 6). In contrast to the chaotic fabric in the mélange, throughout the fault zone there is a pervasive east-west striking fabric, which parallels the local trace of the BRF. The fabric is defined by numerous slip planes concentrated in the fault core (Figure 3F). In the damage zone, there is a higher concentration of flattened relict quartz clasts surrounded by the same fine-grained mud-rich matrix as in the undeformed mélange to the north. The platy minerals define a fabric wrapping around the quartz clasts and feldspar porphyroclasts (Figure 7C and 10C). Within the fault core, there is a similar pattern of flattened quartz clasts which are oriented preferentially, with their long axes parallel to the strike of the fault and its slip planes. Image analysis of the EBSD maps also shows a shape preferred orientation (SPO; Figure 16) of the quartz crystals in the clasts. Rotation, flattening, and boudinage of the clasts are likely to have occurred during faulting.

Both the Valdez flysch and McHugh mélange in this location have been metamorphosed to low-grade greenschist facies (this study; Barefoot et al., 2020). Metamorphism could have occurred as both were subducted to similar depths. Alternatively, it a later episode of high-temperature metamorphism, such as may have been caused during ridge subduction (Amato et al., 2013), could have overprinted both assemblages. An Eocene intrusive event is associated with the passage of a spreading ridge at this location ca. 55 Ma (Bradley et al. 1993; Bradley et al. 2000; Barefoot et al, 2020). However, the associated substantial hydrothermal flow through the area indicates non-uniform stress, with quartz and calcite fracture fill of no preferred orientation. Valdez Group deformation, as indicated by folds and crenulations, was quite

uniform. Furthermore, ca. 55 Ma dikes that cross-cut the area (Barefoot et al., 2020) are also pervasively altered but have no aligned fabric or any offset. The 60–54 Ma Chickaloon conglomerate (White et al., 2006; Trop et al., 2012) which unconformably overlies both McHugh and Valdez (Little and Naeser, 1989) shows deformation features (Figure 4) in its oldest deposits but has no mappable offset in the area. Both the age of the felsic intrusion and the age of the Chickaloon conglomerate serve as time constraints for ca. 60 Ma cessation of faulting and deformation in the area.

Garver and Davidson (2015) suggested that the Chugach terrane flysch (Valdez Group and adjacent Prince William terrane) was deposited in a trench adjacent to the Sierra Nevada-Southern California-Peninsular Arc and was subsequently translated more than 3000 km northward along the continental margin to its current position. They argue the Hf isotope signatures in zircons found in the flysch have signatures indicating a juvenile source rock, which is a unique and distinctive aspect of SW Laurentia. My study of the fault zone and juxtaposed McHugh–Valdez in the Nelchina area indicates that the mélange and flysch sections of the Chugach terrane had to be adjacent by ca. 55 Ma. This agrees with previous studies that place McHugh Complex and Valdez Group in the same structural/geographic setting during deposition (Amato and Pavlis, 2010; Barefoot et al., 2020). Valdez Group deposition took place between 85 and 68 Ma (Kochelek et al., 2011; Amato et al. 2013) and based on the translation hypothesis it started migrating northward ca. 75 Ma (Garver and Davidson, 2015). The flysch section took about 15-20 Myrs to be translated ≥3000 km and placed alongside the older parts of the Chugach terrane. This would imply a motion of ≥15 cm/yr, which is equivalent to the fastest modern plate motion rates and 3 times the rate of the fastest strikes-slip fault displacements. The other faults which connect semi-continuously along the strike of the fault in my area are all moderately to steeply dipping, with thrust-fault indicators uplifting the Valdez Group against the McHugh

Complex (Figure 1). Based on the compressional deformation microstructures as well as the oblique slickenlines on the slip planes, I classify the fault in my area as thrust or transpressional as well. I do not find indication that it has accommodated 3000 km of strike-slip motion. Consequently, I support the hypothesis that the McHugh Complex and Valdez Group were deposited in proximity and remained adjacent.

5.2 Fault rock composition and texture evolution

While I don't think the fault in my area is terrane-bounding, it allows me to investigate compositional and mechanical evolution of slip within a subduction-zone complex.

5.2.1 Composition of the fault core

Consistent with observations from the Alpine fault zone in New Zealand (Sutherland et al., 2012), I found that the core of the fault in my study area is where alteration is concentrated. One of the most evident changes in the fault core area is the color of the tuff layers, which is caused by compositional changes. Carbonaceous material is widespread, which I attribute to alteration of abundant chlorite in the metasediments of the McHugh section. In the presence of calcium-rich fluids and temperature, this process breaks down the chlorite to carbonate (Nakamura and Kato, 2004) and alters the rock from green to pale yellow. Because of the pale shade, I refer to this section as light fault rock (Figure 3E and 3G). The color of the black fault rock is inherited from its parent rock, the black mud metasediments, as well as the additional development of opaque carbonaceous material in the form of injections into clasts and other interlayered units. The black fault-rock samples have high LOI values, with most of the material being lost during heating higher than 1000°C. This suggests high graphite concentrations, which cannot be detected by XRD analyses. SEM imaging of the black patches reveals amorphous texture, and Raman spectroscopy and thermometry classifies it as carbonaceous material, not yet

developed to graphite. It has been suggested that amorphous carbon in fault gouge can develop from frictional melting during fast seismic slip events (Oohashi et al., 2011). SEM images (Figure 10) show no melt textures such as vesicles or amygdales, consequently I assume the amorphous carbonaceous material was not produced by frictional melting. Alternatively, it could remain from original high concentration of carbonaceous material or dissolution precipitation. Regardless of the origin of the amorphous material, it has been shown that CM significantly contributes to fault weakening and conditions that promote slow-slip fault behavior (e.g. Goldsby and Tullis, 2002; Di Toro et al., 2004; Janssen et al., 2010).

5.2.2 Formation of fault gouge

The fault zone is a well-developed zone of crushed rock ~200m wide. Its core, as mentioned above, is a 120m-wide zone of banded light and black fault rock (Figure 2). I classify both the light and black fault rock as gouge. At a typical geothermal gradient of ~25°C/km, gouge which forms at about 10 km depth along a fault displacing metasediments consists of brittlely deformed quartz and feldspar, and clay minerals from hydrothermal alteration of feldspar and micas (Rowe and Griffith, 2015). Feldspar is more susceptible to weathering and grain size reduction than quartz is, due to its cleavage planes and chemistry (Evans, 1988; Rawling and Goodwin, 2003). Hydrothermal alteration in the Nelchina field site is pervasive, and has led to the almost complete replacement of feldspars by low-temperature phyllosilicates. The fault rocks are now primarily composed of quartz, muscovite, clay, metallic oxides or sulphides, and carbonate, which was abundant both in the original metasediment mineralogy and in precipitates of the hydrothermal fluids. The fault gouge is less cohesive and hence weaker than the mélange. Its formation enhanced accommodation and localization of slip along the fault. Recent studies show that fault gouge formation is associated with growth of fine sheet silicate

minerals with no particular crystallographic orientation due to fault-related kinking and rotation (e.g. Warr and Cox 2001; Solum and van der Pluijm 2004; Solum et al., 2005; Wenk et al., 2010; Janssen et al., 2014). The black fault rock, which has weakly oriented clays, fits this classification. In contrast, in the light fault rock I observe aligned phyllosilicates that are concentrated along fractures. This observation is similar to clay microstructures described in fault gouge samples from SAFOD, which is at a creeping section of the San Andreas fault (Holdsworth et al., 2011). Janssen et al. (2016) finds equivalent patches of oriented clay particles in the damage zone of the Aigion fault (Gulf of Corinth) and suggests they are tectonically emplaced into the fault. The combination of weak and moderate preferred orientation in the various sheet silicates in the Nelchina gouge is indicative of a continuous tectonic influence after the initial formation of the gouge in the seismogenic zone. I interpret that the domains of clays with a fabric have formed during a period of aseismic creep, as seismic slip typically leads to fracturing, shearing, and kinking of the sheet silicates (Janssen et al., 2016).

5.2.3 Quartz deformation

Quartz-rich clasts in all three fault-rock samples analyzed with EBSD experienced limited crystal-plastic deformation and pervasive brittle deformation (Figures 12-14). There is widespread development of subgrain boundaries and local development of very fine, subrounded grains along the rims of larger quartz porphyroclasts (Figures 12-14). Even though most quartz grains in our samples have been fractured, there is little to no displacement and limited grain size reduction (Figure 8). Undulose extinction and deformation lamellae are common and indicate intracrystalline distortion, but not recrystallization (Figure 8). One sample (170801-9) from the quartz-rich band of fault rock preserves crystal-plastic deformation and recrystallization, indicated by crystallographic orientation analysis (Figure 14). The quartz CPO development is

consistent with basal <a> and rhomb <a> slip systems (e.g., Toy et al., 2008; Langille et al., 2010, 2014; Singleton & Mosher, 2012). The grains scattered away from the maximum are either the very fine quartz grains from the parent sediment, or they have been recrystallized. The quartz c-axis patterns in this sample are consistent with bulging recrystallization and deformation temperatures from ~200 to 400° C. (e.g., Stipp et al., 2002; Passchier & Trouw, 2005). This temperature range is an estimate, as studies have indicated that quartz c axis patterns are not strictly a function of temperature (e.g., Toy et al., 2008).

5.3 Thermal evolution of the fault zone, based on microstructures

I associate the specific mineralogy and complex network of deformation microstructures formed during multiple slip events and a consequent progressive down-temperature deformation during fault exhumation. At subduction zones, the rocks closest to the plate-boundary margin are actively deformed and metamorphosed at the same time. The McHugh mélange at this location was metamorphosed to lower greenschist facies (temperatures not exceeding 400°C) during subduction (Barefoot et al., 2020), which is typical for metasediments in the seismogenic zone (Moore et al., 2007). Within the fault zone, quartz-rich clasts preserve ductile deformation microstructures—deformation lamellae, grain bulges, sweeping undulose extinction, pressure solution, and brittle fractures that are characteristic of low metamorphic grade (300–400°C) at the brittle–ductile transition (Passchier and Trouw, 2005). CPO is weak in most quartz clasts, except for one population of quartz in a narrow band of mylonitized metasediment, which exhibits a moderate CPO (Figure 14). The localization of CPO is likely due to the lower phyllosilicate-to-quartz ratio in the mylonitized band. Experiments have shown that higher mica-to-quartz ratios limit the ability of rocks to develop CPO in the quartz during deformation (Song and Ree, 2007). Deformation in the rest of the fault rocks is influenced by the high ratio of fine-

grained matrix to clasts, where strain is accommodated by soft-sediment deformation, rotation of sheet silicates and quartz clasts, as well as pervasive fracturing and less abundant shearing. Brittle overprinting is expressed by the black fault rock and fractures cross-cutting the stretched quartz phacoids. Raman spectra peak ratio calculations suggest maximum metamorphic temperatures during the development of the graphitic carbon of 300-350°C (refer to section 4.7 and Figure 19 and 20). The mobilization into injection veins of the carbonaceous material, however, doesn't require temperatures higher than 200°C. Replacement of feldspars by low-temperature phyllosilicates and simultaneous formation of gouge occurred at a similar low thermal maturity. Most of the fractures developed into veins that are evidence for extensive hydrothermal alteration related to the increased presence of fluids mobilized during intrusive events in the region. I associate the fault-rock compositions and fabric development with progressive down-temperature deformation as the fault was exhumed.

5.4 Deformation mechanisms and fault-slip style

Fault-rock fabrics along the continuation of the Eagle River fault in the Nelchina area indicate both seismic slip and aseismic creep. Isometrically oriented clays in the black fault-rock gouge can be related to fracturing, shearing, and kinking during seismic slip (Janssen et. al, 2016). The lighter fault rocks preserve sheet silicates that possibly became preferentially oriented during aseismic creep. However, relative timing of these different slip behaviors is hard to determine. They could have even been active at the same time. As faults get wider with depth, their slip behavior also becomes more complex. Multiple modes of failure are shown to be active simultaneously (Figure 22; Kahn et. al, 2017).

Another complication is that primarily the latest stage of slip is preserved in the rock record. It is possible that the fault zone in my study area has generated earthquakes at any point

in its history. However, fault rocks rarely preserve pseudotachylites/frictional melts, because these rock types are highly susceptible to alteration. Additionally, faults are great conduits of water. Hence, it is likely that any post-seismic deformation and fluids may have destroyed structures generated during seismic slip (Rowe and Griffith, 2015).

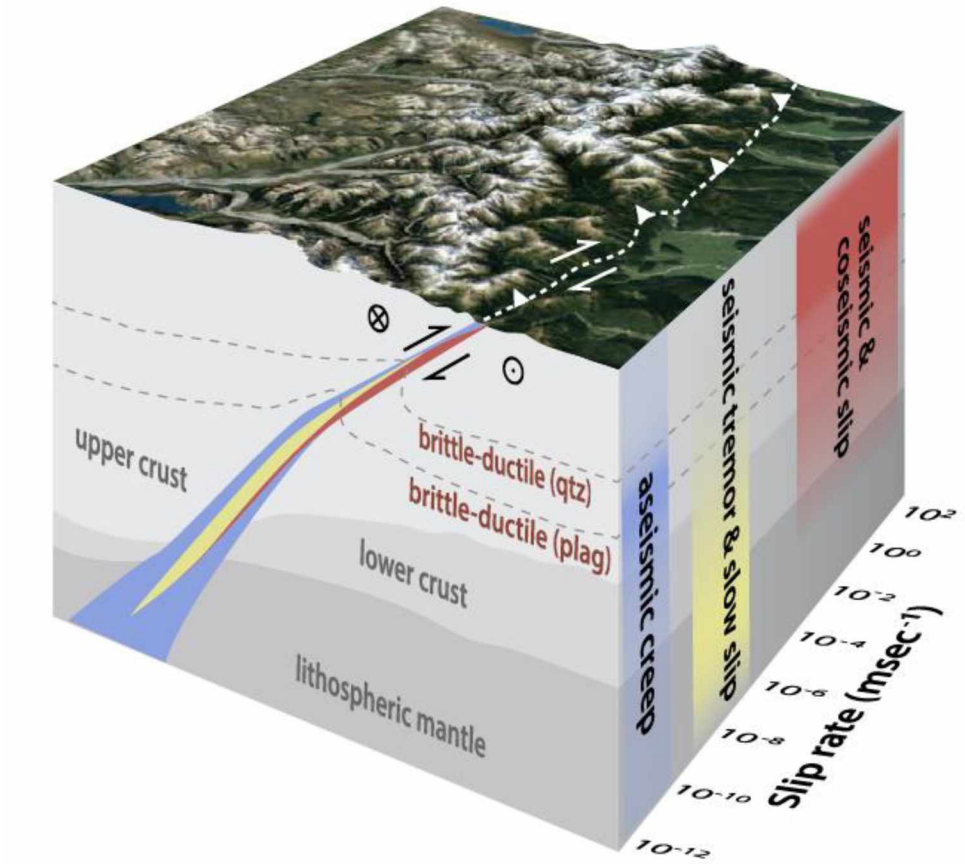

Figure 22: *Schematic block model linking the rock record of fault mechanics across the lithosphere to the different slip modes of the seismic cycle (from Kahn et al., 2017).*

5.5 Age constraints from fault-rock samples

Interpreting the age(s) of slip along this fault turned out to be the most challenging aspect. Mineral separates that had measurable concentrations of K in hand sample were sent for Ar/Ar dating that turned out to be inconclusive. However, using the thermochronometry alongside regional and local age constraints, I can provide some interpretations of fault-zone and local tectonic activity. I interpret that fault activity lasted from ca. 120 Ma to ca. 60 Ma. This was followed by uplift and cooling in two stages: ca. 40 Ma and ca. 20 Ma. Figure 23 summarizes new and existing age data that align with major tectonic events, including interpretations of intervals of subduction accretion and erosion as suggested by Amato et al. (2013) for the Chugach accretionary complex.

5.5.1 Ca. 160 Ma Talkeetna Arc age signature, and accretion of the McHugh Complex

The McHugh Complex is generally interpreted as a record of continuous subduction from Jurassic through latest Cretaceous time. Talkeetna arc magmatism ranged from 202 to 153 Ma (e.g., Amato et al., 2007; Rioux et al., 2007). The Chitina arc, also part of the of the Wrangellia composite terrane, was active from 171-140 Ma (Plafker et al., 1989; Roeske et al., 2003). The ca. 160 Ma $^{40}Ar/^{39}Ar$ age signal in black fault rock sample 170801-4 (whole-rock and metamorphic muscovite; Figure 21) from the study area overlaps in age with volcanism in both the Talkeetna and Chitina arcs, which were the main sediment sources for the mélange (Amato and Pavlis, 2010). Amato et al. (2013) used detrital-zircon data to show that there are at least two parts of the McHugh Complex with distinct accretion ages: the 169–156 Ma Potter Creek assemblage, and the 101–91 Ma McHugh Creek metaclastic assemblage. In our study area, the mélange lithologically matches the Potter Creek assemblage (Barefoot et al., 2020). Periods of subduction erosion in the Middle and Late Cretaceous (e.g., Haeussler et al. 2006; Bradley et al.

2007; Amato and Pavlis 2010) account for any missing Potter Creek material north of the Eagle River fault, as well as the entire missing Late Cretaceous McHugh Creek assemblage in our area.

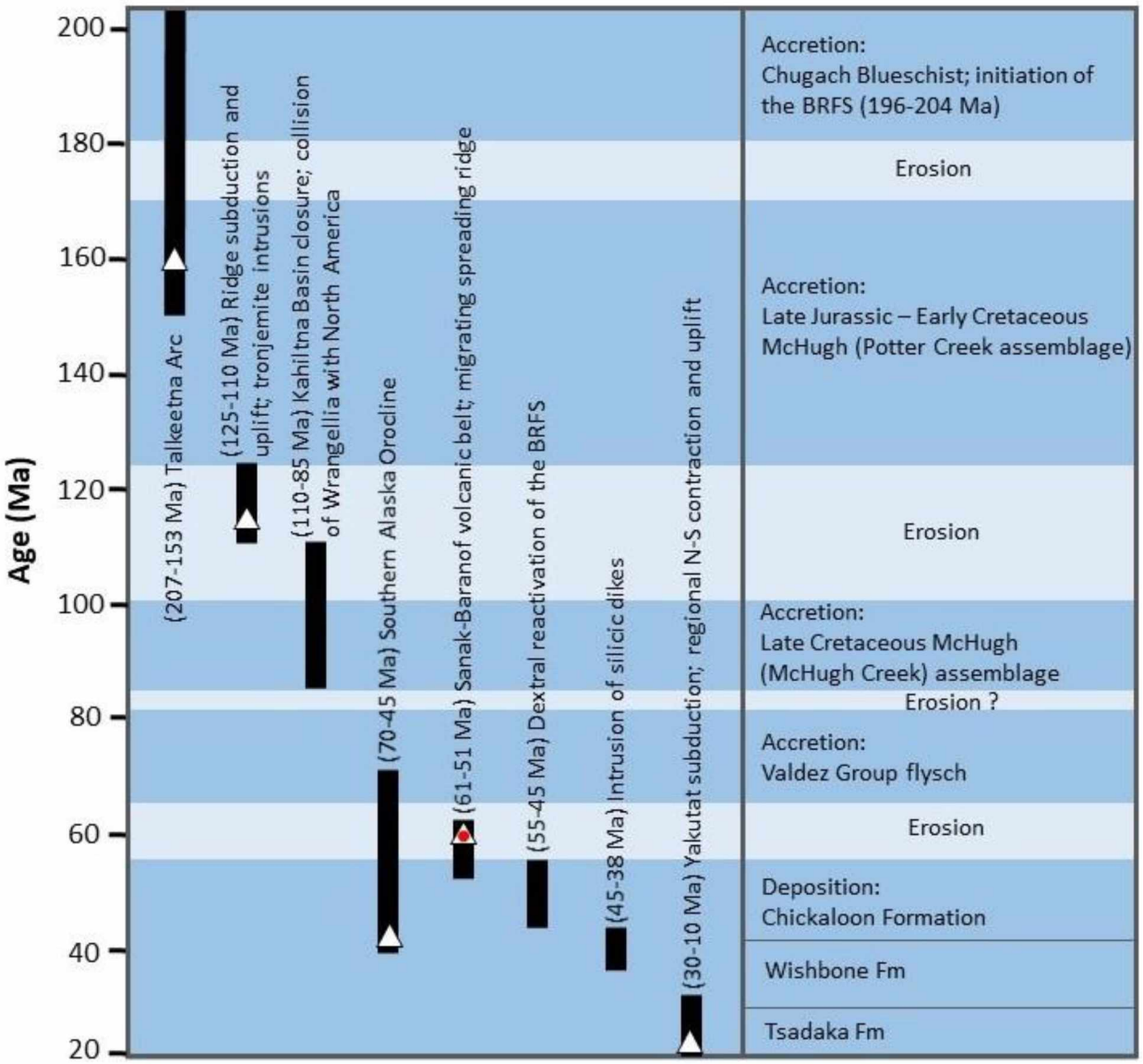

Figure 23: *Schematic summary of tectonic and accretionary events in southern Alaska from 200 Ma to 20 Ma. Triangles represent 40Ar/39Ar ages of the fault-rocks dated in this study. Red dot marks the 40Ar/39Ar age of a silicic dike along the northern edge of the fault zone (Barefoot et al., 2020). Modified after Amato and Pavlis (2010).*

5.5.2 Ca. 120 Ma signal—possible Early Cretaceous ridge subduction and uplift

During Late Jurassic to earliest Cretaceous time, the Potter Creek assemblage was actively accreting along a subduction channel south of the Border Ranges Fault (Amato et al., 2013). In the Early Cretaceous, parts of this mélange assemblage underwent amphibolite-facies metamorphism, ductile deformation within the subduction zone, and intrusion by a suite of leucotonalite-trondhjemite plutons (Pavlis, 1982; Pavlis et al., 1988; Burns 1991; Barnett et al.,1994; Labrado et al., 2015). Early studies attributed the distinct geochemical and isotopic character of the plutons to two different hypotheses: (1) ridge subduction (e.g., Pavlis, 1982), or (2) melting along a juvenile subduction-zone interface recording reestablishment of subduction (Barnett et al., 1994). Recent studies have favored the ridge-subduction hypothesis (e.g., Amato and Pavlis, 2010; Amato et al., 2013; Labrado et al., 2015, Mahar et al., 2018). These zircon U-Pb geochronology studies of the plutons yielded ages ranging from 142 Ma to 121 Ma, with ~90% of the ages falling between 126 and 121 Ma. This supports previous age determinations—for example, Barnett et al. (1994) reported 122–119 Ma $^{40}Ar/^{39}Ar$ biotite dates from the tonalite-trondhjemite suite. Two whole-rock $^{40}Ar/^{39}Ar$ analyses of black fault rock, samples 170801-8 and 170801-2, yield age plateaus of 121.7 Ma and 114.2 Ma, respectively (Figure 21). These ages fall at the tail end of the ages of the tonalite-trondhjemite suite that has been associated with ridge subduction. The early-release steps of these samples' spectra fall at much younger ages, and may indicate incomplete resetting of the ages from a high-temperature pulse ca. 120 Ma. Ages of rocks within the fault zone could have reset during the proposed ridge-subduction event. Another possibility is that these samples record onset of faulting. It would be difficult to distinguish between re-heating due to high heat flow associated with a subducting ridge, and heating due to fault slip at near-greenschist facies conditions.

5.5.3 Ca. 60 Ma rapid uplift and near-trench magmatism

No Ar plateaus are recorded in fault-rock samples between ca. 115 and 60 Ma. This is consistent with the Amato et al. (2013, and references therein) interpretation of southern margin subduction erosion from ca. 125 to 100 Ma, after which the McHugh Creek (conglomerate-rich) assemblage was deposited during collision of the Wrangellia composite terrane with North America.

A single-step Ar release plateau of ca. 60 Ma is present in nearly all samples, is the first-release step in sample -2 whole-rock, and is a prominent step in samples -4 whole-rock 2 and -8 whole-rock 1 (Figure 21). Additionally, this 60 Ma signal appears in whole-rock Ar ages determined for altered pillow-lava blocks within the McHugh in this study area (Barefoot et al., 2020). While individually uncompelling, the ubiquity of this 60 Ma signal in all samples from the region suggests some thermal event of that age. I ascribe it to a thermal pulse that may have accompanied widespread hydrothermal circulation triggered by the well-documented Paleocene–Eocene subduction and migration of an ocean spreading ridge along the southern Alaska margin.

The Sanak-Baranof belt is a chain of granitic to tonalitic intrusions spanning from Sanak Island in the west to Baranof Island in the east (Figure 1). Intrusions of this age and of similar composition are found in both the McHugh Complex and the Valdez Group, both parallel to and cross-cutting the regional fabric (e.g. Hudson et al., 1979; Little 1988; Little and Naeser, 1989; Bradley et al. 1993; Bradley et al., 2000; Barefoot et al., 2020). In the Nelchina area, one felsic dike was dated by U-Pb zircon geochronology to 54 Ma, and its trace-element geochemistry aligned it with dikes of similar age throughout the region (Barefoot et al., 2020). There are several such dikes in the study area (unit Ti on the field area map; Figure 2), the widest of which is ~150 m wide and is exposed close to the north edge of the fault zone.

5.5.4 Ca. 40 Ma compression and the southern Alaska orocline

The metamorphic muscovite $^{40}Ar/^{39}Ar$ age spectra in samples 170801-4 and 170801-3 have a minimum step ca. 35 Ma. Sample 170801-8 whole-rock analysis has a minimum age release step ca. 40 Ma and sample 170801-4 feldspar has a segment ca. 40 Ma over the final 25% of cumulative ^{39}Ar released. While the spectra of these samples are complex individually, the overlapping ca. 35-40 Ma segments suggest an actual event. Studies documenting reverse faulting reactivation and folding of Eocene strata indicate Late Eocene shortening of the forearc basin (Little and Naeser, 1989). These have been interpreted as a result of uplift caused by oroclinal bending in southern Alaska (e.g. Pavlis, 1982; Little and Naeser, 1989). Little and Naeser (1989) traced high-angle faults part of the BRFS which displace the Chickaloon Formation. Both east and west of the oroclinal deflection, subvertical faults are characterized by dextral-slip separations, associated Riedel shears, and horizontal slicken lines (Little and Naeser, 1989). Deposition of the Chickaloon Formation also marks a period of uplift and consequent cooling over a period from ~60-40 Ma. There is no significant offset of any part of the Chickaloon in my field area.

5.5.5 Ca. 20 Ma regional uplift and Yakutat flat-slab subduction

The most recent period of regional uplift accompanied by widespread and rapid cooling along the BRFS has been recorded by early Miocene apatite fission-track ages of ca. 22-17 Ma (Little and Naeser, 1989). This regional uplift of the central Chugach Mountains has been associated with collision and flat-slab subduction of the Yakutat block under the eastern Gulf of Alaska and with rapid Miocene and younger exhumation of the eastern Chugach/St. Elias mountains (Davis and Plafker, 1986). The Cretaceous subduction complex is the suggested provenance of upper Miocene rocks in Cook Inlet, which serves as further evidence for escalated

uplift and erosion at the time (e.g., Kirschner and Lyon, 1973). In the Nelchina area, early Miocene uplift and exhumation is likely recorded by the robust ca. 20 Ma feldspar $^{40}Ar/^{39}Ar$ age from black fault rock sample 170801-4. This age is also seen in large plateaus of the same age in metamorphic muscovite from fault gouge sample 170801-3.

Chapter 6: Conclusion

My mapping, structural analysis, geochemical analysis and dating of fault-related rocks near the Nelchina Glacier lends insight into the compositional and mechanical evolution of slip within a major subduction-zone complex in Southern Alaska. Based on the composition and microstructures observed using optical microscopy, XRF, XRD, Raman spectroscopy, SEM and EBSD quantification of fabric, I suggest deformation within the accretionary prism initiated in brittle-ductile conditions. The fault records evidence for both seismic slip and aseismic creep. Constraining the relative timing of the two different slip behaviors is hard to determine. It is even possible they were active at the same time, especially with the increase of width and complexity at the deeper part of the fault. What is preferentially preserved in the rock record however, is the latest stage of slip. The consequent exhumation and cooling lead to progressive down-temperature brittle deformation and often strong hydrothermal alteration, as seen in my area. Frictional melt structures generated during earthquakes are rarely preserved due to their susceptibility to alteration.

Using $^{40}Ar/^{39}Ar$ thermochronometry alongside regional and local age constraints, I was able to provide some insight on timing of fault-zone and local tectonic activity. I interpret that fault activity lasted from ca. 120 Ma to ca. 60 Ma., and was followed by two stages of accelerated uplift and cooling during ca. 40 Ma and ca. 20 Ma. The cessation of major fault activity after ca. 60 Ma, the lack of pervasive strike-slip motion indicators, and the presence of undeformed Eocene dikes as well as Eocene sediments deposited on top of both the McHugh Complex and Valdez Group, suggest these two main components of the Chugach accretionary prism were deposited in proximity and were in place in Southern Alaska at the start of the Eocene epoch.

References

Amato, J.M., and Pavlis, T.L. 2010. Detrital zircon ages from the Chugach terrane, southern Alaska, reveal multiple episodes of accretion and erosion in a subduction complex. Geology, 38: 459–462.

Amato, J. M., Rioux, M. E., Kelemen, P. B., Gehrels, G. E., Clift, P. D., Pavlis, T. L., and Draut, A. E., 2007, U-Pb geochronology of volcanic rocks from the Jurassic Talkeetna Formation and detrital zircons from prearc and postarc sequences: Implications for the age of magmatism and inheritance in the Talkeetna arc, in Tectonic Growth of a Collisional Continental Margin: Crustal Evolution of Southern Alaska, edited by K. D. Ridgway et al., Special Paper Geological Society of America, 431, 253– 271.

Amato, J.M., Pavlis, T.L., Clift, P.D., Kochelek, E.J., Hecker, J.P., Worthman, C.M., and Day, E.M. 2013. Architecture of the Chugach accretionary complex as revealed by detrital zircon ages and lithologic variations: Evidence for Mesozoic subduction erosion in south-central Alaska. Bulletin of the Geological Society of America, 125: 1891–1911.

Bachmann, F., Hielscher, R., Schaeben, H., 2010. Texture analysis with MTEX - free and open source software toolbox. Solid State Phenom. 160, 63-68.

Bakun, W. H., King, G. C. P. and Cockerham, R. S., 1986. Seismic slip, aseismic slip, and the mechanics of repeating earthquakes on the Calaveras fault, California. In Earthquake Source Mechanics (American Geophysical Union), pp. 195–207. (Geophysical Monograph 37).

Barefoot, J., Nadin, E. S., Newberry, R. J., and Camacho, A., 2020. Rock and age relationships within the Talkeetna forearc subduction complex in the Nelchina area, southern Alaska. Canadian Journal of Earth Science, 999, 1-16.

Barnett, D. E., J. R. Bowman, T. L. Pavlis, J. R., Rubenstone, L. W. Snee, and T. C. Onstott, 1994. Metamorphism and near-trench plutonism during initial accretion of the Cretaceous Alaskan forearc, Journal of Geophysical Research, 99, 24, 7–24.

Beyssac, O., Goffé, B., Chopin, C., & Rouzaud, J. N. (2002). Raman spectra of carbonaceous material in metasediments: A new geothermometer. Journal of Metamorphic Geology, 20, 859–871.

Bradley, D.C., and Kusky, T.M., 1992, Deformation history of the McHugh Complex, Seldovia quadrangle, southcentral Alaska, in Bradley, D.C., and Ford, A., eds., Geologic Studies in Alaska: U.S. Geological Survey Bulletin 1999, p. 17–32.

Bradley, D.C., Haeussler, P.J., and Kusky, T.M. 1993. Timing of early Tertiary ridge subduction in southern Alaska. U.S. Geological Survey Bulletin 2068: 163-177.

Bradley, D.C., Kusky, T.M., Haeussler, P.J., Karl, S.M., and Donley, D.T. 1999. Geologic map of the Seldovia quadrangle, south-central Alaska, U.S. Geological Survey Open-File Report OFR 88-18B. 1 sheet, 1:250,000.

Bradley, D.C., Parrish, R., Clendenen, W., Lux, D., Layer, P., Heizler, M., and Donley, D.T. 2000. New geochronological evidence for the timing of early Tertiary ridge subduction in southern Alaska. US Geological Survey Professional Paper 1615: 5–21.

Bradley, D.C., Kusky, T.M., Haeussler, P., Goldfarb, R., Miller, M., Dumoulin, J., Nelson, S.W., and Karl, S. 2003. Geologic signature of early Tertiary ridge subduction in Alaska. Geological Society of America Special Paper 371: 19-49.

Bradley, D.C., Haeussler, P., O'Sullivan, P., Friedman, R., Till, A., Bradley, J. D., and Trop, J. 2007. Detrital Zircon Geochronology of Cretaceous and Paleogene Strata Across the South-Central Alaskan Convergent Margin. U.S. Geological Survey Professional Paper 1760–F: 36.

Burns, L.E., Pessel, G.H., Little, T.A., Pavlis, T.L., Newberry, R.J., Winkler, G.R., and Decker, J. 1991. Geology of the northern Chugach Mountains, southcentral Alaska. Alaska Division of Geological and Geophysical Surveys Professional Report 94.

Clark, S.H.B. 1973. The McHugh Complex of south-central Alaska. U.S. Geological Survey Bulletin 1372-D.

Connelly, W., 1978. Uyak Complex, Kodiak Is- land, Alaska: A Cretaceous subduction zone: Geological Society of America Bulletin, v.89, no. 5, p. 755-769.

Cowan, D. S., and R. F. Boss, 1978. Tectonic framework of the southwestern Kenai Peninsula, Alaska, Geological Society of America Bulletin, 89, 155-158.

Cowan, D.S., 1999. Do faults preserve a record of seismic slip? A field geologist's opinion. Journal of Structural Geology, 21, 995-1001.

Cowan, D.S. 2003. Revisiting the Baranof-Leech River hypothesis for early Tertiary coastwise transport of the Chugach-Prince William terrane. Earth and Planetary Science Letters, 213: 463-475.

Davis, A. and Plafker, G., 1986. Eocene basalts from the Yakutat terrane: Evidence for the origin of an accreting terrane in southern Alaska. Geology, v. 14.

Di Toro, G., Goldsby, D.L., Tullis, T.E., 2004. Friction falls toward zero in quartz rock as slip velocity approaches seismic rates. Nature 427, 436-439.

Evans, J.P., 1988. Deformation mechanisms in granitic rocks at shallow crustal levels, Journal of Structural Geology, 10, 437-443.

Garver, J.I., and Davidson, C.M. 2015. Southwestern Laurentian zircons in Upper Cretaceous flysch of the Chugach-Prince William terrane in Alaska. American Journal of Science, 315: 537-556.

Goldsby, D.L., and Tullis, T.E., 2002, Low frictional strength of quartz rocks at subseismic slip rates: Geophysical Research Letters, v. 29.

Haeussler, P.J., Gehrels, G.E., and Karl, S.M. 2006. Constraints on the age and provenance of the Chugach accretionary complex from detrital zircons in the Sitka Graywacke near Sitka, Alaska. U.S. Geological Survey Professional Paper 1709-F.

Halfpenny, A., Prior, D. J., & Wheeler, J. (2012). Electron backscatter diffraction analysis to determine the mechanisms that operated during dynamic recrystallisation of quartz-rich rocks. Journal of Structural Geology, 36, 2–15.

Holdsworth, R.E., van Diggelen, E.W., Spiers, C.J., de Bresser, H., Walker, R.J., Bowen, L., 2011. Fault rocks from the SAFOD core samples: implications for weakening at shallow depths along the San Andreas Fault. California. Journal of Structural Geology, 33, 132-144.

Hudson, Travis, Plafker, George, and Peterman, Z.E., 1979, Paleogene anatexis along the Gulf of Alaska margin: Geology, v. 7, no. 12, p. 573-577.

Janssen, C., Wirth, R., Rybacki, E., Naumann, R., Kemnitz, H., Wenk, H., Dresen, G., 2010. Amorphous material in SAFOD core samples (San Andreas Fault): evidence for crush-origin pseudotachylytes? Geophysical Research Letters, 37 (1), L01303.

Janssen, C., Kanitpanyacharoen, W., Wenk, H.-R., Wirth, R., Morales, L., Rybacki, E., Kienast, M., Dresen, G., 2012. Clay fabrics in SAFOD core samples. Journal of Structural Geology, 43, 118-127.

Janssen, C., Wirth, R., Wenk, H.-R., Morales, L., Naumann, R., Kienast, M., Song, S.-R., Dresen, G., 2014. Faulting processes in active faults e evidences from TCDP and SAFOD drill core samples. Journal of Structural Geology, 65, 100-116.

Janssen, C., Wenk, H.-R., Wirth, R., Morales, L., Kemnitz, H., Sulem, M., Dresen, G., 2016. Microstructures and their implications for faulting processes - Insights from DGLab core samples from the Gulf of Corinth. Journal of Structural Geology, 86, 62-74.

Jones, D.L., Silberling, N.J., Coney, P.J., and Plafker, G., 1987, Lithotectonic terrane map of Alaska (west of the 41st meridian): U.S. Geological Survey Miscellaneous Field Studies Map MF-874, scale 1:2,500,000.

Kahn, D., Roberts, J., and Rich, J., 2017. Integrating microseismic and geomechanics to interpret hydraulic fracture growth. Proceedings of the 5th Unconventional Resources Technology Conference (2016).

Karl, S.M., Oswald, P.J., and Hults, C.P. 2015. Field guide to the Mesozoic arc and accretionary complex of South-Central Alaska, Indian to Hatcher Pass. Geological Society of America Cordilleran Section Guidebook, Anchorage, Alaska.

Kirschner, C.E., and Lyon, C.A., 1973. Stratigraphic and tectonic development of Cook Inlet petroleum province, in Pitcher, M.G., ed., Arctic geology: American Association of Petroleum Geologists Memoir 19, p. 396–407.

Kochelek, E.J., Amato, J.M., Pavlis, T.L., and Clift, P.D. 2011. Flysch deposition and preservation of coherent bedding in an accretionary complex: Detrital zircon ages from the Upper Cretaceous Valdez Group, Chugach terrane, Alaska. Lithosphere, 3: 265–274.

Kusky, T.M., and D.C. Bradley. 1999. Kinematics of melange fabrics: Examples and applications from the McHugh Complex, Kenai Peninsula, Alaska, J. Struct. Geol., 21, 1773-1796.

Kusky, T. M., Bradley, D. C., Haeussler, P. H., Karl, S. K. and Donley, D. T., 1993, The Chugach Bay thrust, a major tectonic boundary in the Seldovia Quadrangle, south-central Alaska. Geological Society America, Abstracts with Programs 25,282.

Kusky, T.M., Bradley, D.C., Haeussler, P.J., and Karl, S. 1997. Controls on accretion of flysch and mélange belts at convergent margins: Evidence from the Chugach Bay thrust and Iceworm mélange, Chugach accretionary wedge, Alaska. Tectonics, 16: 855-878.

Labaume, P., Carrio-Schaffhauser, E., Gamond, J.-F., Renard, F., 2004. Deformation mechanisms and fluid-driven mass transfers in the recent fault zones of the Corinth Rift (Greece). Comptes Rendus Geoscience, 336, 375-383.

Labrado A., Pavlis, T., Amato, J.M., and Day, E.M., 2015. The tectonic significance of the Early Cretaceous forearc metamorphic assemblage in south-central Alaska based on detrital zircon U-Pb dating of sedimentary protoliths. Canadian Journal of Earth Sciences, 52: 1182–1190.

Langille, J. M., Jessup, M. J., Cottle, J. M., Newell, D., & Seward, G., 2010. Kinematic evolution of the Ama Drime detachment: Insights into orogen-parallel extension and exhumation of the Ama Drime Massif, Tibet-Nepal. Journal of Structural Geology, 32, 900–919.

Langille, J. M., Jessup, M. J., Cottle, J., & Ahmad, T., 2014. Kinematic and thermal studies of the Leo Pargil Dome: Implications for synconvergent extension in the NW Indian Himalaya. Tectonics, 33, 1766–1786.

Little, T.A. 1988. Tertiary tectonics of the Border Ranges fault system, north-central Chugach Mountains, Alaska: Sedimentation, deformation and uplift along the inboard edge of a subduction complex. Ph.D. dissertation, Department of Geology, Stanford University, Stanford, CA.

Little, T.A., and Naeser, C.W. 1989. Tertiary tectonics of the Border Ranges Fault System, Chugach Mountains, Alaska: Deformation and uplift in a forearc setting. Journal of Geophysical Research: Solid Earth, 94: 4333–4359.

Little, T.A., 1992. Development of wrench folds along the Border Ranges fault system, southern Alaska, U.S.A. Journal of Structural Geology, v. 105, no. 3, p. 343–359.

Mackevett, E., and Plafker, G. 1974. The Border Ranges fault of south-central Alaska. Journal of Research of the U.S. Geological Survey, 2: 323-329.

Magoon, L. B., W. L. Adkison, and R. M. Egbert, 1976. Map showing geol-ogy, wildcat wells, Tertiary plant fossil localities, K-Ar age dates, andpetroleum operations, Cook Inlet area, Alaska, U.S. Geological SurveyMap I-1019, scale 1:250,000, 3 sheets.

Mahar, M.A., Pavlis, T.L., Bowman, J.R., Goodell, P., Conrad, W.K., 2018. Early Cretaceous ridge subduction beneath southern Alaska: Insights from zircon U-Pb geochronology, hafnium and oxygen isotopic composition of the Western Chugach Tonalite-Trondhjemite Suite. AGU Fall Meeting Abstracts 2018, V31D-0151.

Nakamura K., and Kato Y., 2004. Carbonatization of oceanic crust by the seafloor hydrothermal activity and its significance as a CO2 sink in the Early Archean. Geochim Cosmochim Acta 68:4595–4618

Nakamura, Y., Oohashi, K., Toyoshima, T., Satish-Kumar, M., Akai, J., 2015. Strainінduced amorphization of graphite in fault zones of the Hidaka metamorphic belt, Hokkaido, Japan. Journal of Structural Geology, 72, 142-161.

Nokleberg,W.J., Plafker, G., Lull, J.S.,Wallace,W.K., andWinkler, G.R., 1989, Structural analysis of the southern Peninsular, southern Wrangellia, and northern Chugach terranes along the Trans-Alaska Crustal transect, Northern Chugach mountains, Alaska: Journal of Geophysical Research, v. 94, p. 4297–4320.

Nokleberg, W.J., Plafker, G., and Wilson, F.H., 1994, Geology of south-central Alaska, in Plafker, G., and Berg, H.C., eds., The Geology of Alaska: Boulder, Colorado, Geological Society of America, Geology of North America, v. G-1, p. 311–366.

Oohashi, K., Hirose, T., Shimamoto, T., 2011. Shear-induced graphitization of carbonaceous materials during seismic fault motion: experiments and possible implications for fault mechanics. J. Struct. Geol. 33, 1122-1134.

Passchier, C. W., and Trouw, R. A. J., 2005, Microtectonics: Berlin ; New York, Springer, xvi, 366 p. p.

Pavlis, T.L. 1982. Origin and age of the Border Ranges Fault of southern Alaska and its bearing on the Late Mesozoic tectonic evolution of Alaska. Tectonics, 1: 343–368.

Pavlis, T.L., Monteverde, D.H., Bowman, J.R., Rubenstone, J.L., and Reason, M.D., 1988, Early Cretaceous near-trench plutonism in southern Alaska: A tonalite-trondhjemite intrusive complex injected during ductile thrusting along the Border Ranges fault system: Tectonics, v. 7, p. 1179–1199.

Pavlis, T.L., and Roeske, S.M. 2007. The Border Ranges fault system, southern Alaska. Geological Society of America Special Paper 431: 95–127.

Pessel, G.H., Henning, M.W., and Burns, L.E. 1981. Preliminary geologic map of parts of the Anchorage C-1, C-2, D-1, and D-2 quadrangles, Alaska. Alaska Division of Geological and Geophysical Surveys, Open-file Report AOF-121. 1 sheet, scale 1:63,360.

Plafker, G., and Berg, H.C. 1994. Overview of the geology and tectonic evolution of Alaska. The Geology of Alaska: Geological Society of America. pp. 989–1021.

Plafker, G., Nokleberg, W.J., and Lull, J.S. 1989. Bedrock geology and tectonic evolution of the Wrangellia, Peninsular, and Chugach terranes along the Trans-Alaska Crustal Transect in the Chugach Mountains and southern Copper River basin, Alaska. Journal of Geophysical Research, 94: 4255–4295.

Plafker, G., Moore, J.C., and Winkler, G.R. 1994. Geology of the southern Alaska margin. The Geology of Alaska: Geological Society of America. pp. 389–449.

Rawling G.C., and Goodwin L.B., 2003. Cataclasis and particulate flow in faulted, poorly lithified sediments. Journal of Structural Geology, 25, 317–331.

Rioux, M., Hacker, B., Mattinson, J., Kelemen, P., Blusztajn, J., and Gehrels, G. 2007. Magmatic development of an intra-oceanic arc: High-precision U-Pb zircon and whole-rock isotopic analyses from the accreted Talkeetna arc, south-central Alaska. Geological Society of America Bulletin, 119: 1168–1184.

Roeske, S.M., Snee, L.W., and Pavlis, T.L., 2003, Dextral-slip reactivation of an arc-forearc boundary during Late Cretaceous-Early Eocene oblique convergence in the northern Cordillera, in Sisson, V.B., Roeske, S.M., and Pavlis, T.L., eds., Geology of a Transpressional Orogen Developed during Ridge-Trench Interaction along the North Pacific Margin: Geological Society of America Special Paper 371, p. 141–169.

Roeske, S.M., Mattinson, J.M., Armstrong, R.L. 1989. Isotopic ages of glaucophane schists on the Kodiak Islands, southern Alaska, and their implications for the Mesozoic tectonic history of the Border Ranges fault system. Geological Society of America Bulletin, 101: 1021-1037.

Rowe, C.D. and Griffith, A.W., 2015, Do faults preserve a record of seismic slip: a second opinion, J. Struct. Geol., 78 (2015), pp. 1-26

Rutter, E.H., Hackston, A.J., Yeatman, E., Brodie, K.H., Mecklenburgh, J., and May, S.E, 2013. Reduction of friction on geological faults by weak-phase smearing. Journal of Structural Geology, 51, 52-60.

Sample, J., and D. M. Fisher, 1986. Duplexes and underplating in an ancient accretionary complex, Kodiak Islands, Alaska, Geology, 14, 160-163.

Sample, J. C., and J. C. Moore, 1987. Structural style and kinematics of an underplated slate belt, Kodiak and adjacent islands, Alaska, Geol. Soc. Am. Bull., 99, 7-20.

Sample J.C., and Reid M., 2003. Large-scale, latest Cretaceous uplift along the northeast Pacific Rim: evidence from sediment volume, sandstone petrography and Nd isotope signatures of the Kodiak Formation, Kodiak Islands, Alaska. In Geology of a Transpressional Orogen Developed during Ridge-Trench Interaction along the North Pacific Margin, Sisson VB, Roeske SM, Pavlis TL (eds). Geological Society of America: Boulder, CO; Special Paper 371: 51–70.

Schleicher, A.M., Tourscher, S.N., van der Pluijm, Ben A., Warr, L.N., 2009. Constraints on mineralization, fluid-rock interaction, and mass transfer during faulting at 2e3 km depth from the SAFOD drill hole. Geophysical Research Letters 114, B04202.

Singleton, J. S., and Mosher, S., 2012. Mylonitization in the lower plate of the Buckskin-Rawhide detachment fault, west-central Arizona: Implications for the geometric evolution of metamorphic core complexes. Journal of Structural Geology, 39, 180–198.

Skemer, P., Katayama, I., Jiang, Z., Karato, S.I., 2005. The misorientation index: development of a new method for calculating the strength of lattice-preferred orientation. Tectonophysics 411, 157-167.

Solum, J.G., and van der Pluijm, B.A., 2004. Phyllosilicate mineral assemblages of the SAFOD pilot hole and comparison with an exhumed segment of the San Andreas Fault system. Geophysical Research Letters 31, L15S19.

Solum, J., van der Pluijm, B. and Peacor, D., 2005, Neocrystallization, fabrics and age of clay minerals from an exposure of the Moab Fault, Utah, Journal of Structural Geology, 27, 1563 – 1576.

Song, W.J., and Ree, J.H., 2007. Effect of mica on the grain size of dynamically recrystallized quartz in a quartz-muscovite mylonite. Journal of Structural Geology, 29, 1872-1881

Stipp, M., H. Stünitz, R. Heilbronner, and S. M. Schmid, 2002. The eastern Tonale fault zone: A "natural laboratory" for crystal plastic deformation of quartz over a temperature range from 250°C to 700°C, Journal of Structural Geology, 24, 1861–1884.

Sutherland R., Toy V.G., Townend J., Cox S.C., Eccles J.D., Faulkner D.R., Prior D.J., Norris R.J., Mariani E., Boulton C., Carpenter B.M., Menzies C.D., Little T.A., Hasting M., De Pascale G.P., Langridge R.M., Scott H.R., Reid Lindroos Z., Fleming B., Kopf A.J., 2012. Drilling reveals fluid control on architecture and rupture of the Alpine fault, New Zealand: Geology, v. 40, p. 1143–1146.

Toy V.G., Prior D.J., Norris R.J., 2008. Quartz fabrics in the Alpine fault mylonites: Influence of pre-existing preferred orientations on fabric development during progressive uplift: Journal of Structural Geology, v. 30, p. 602–621.

Trimby, P.W., Prior, D. J., & Wheeler, J., 1998. Grain boundary hierarchy development in a quartz mylonite. Journal of Structural Geology, 20(7), 917–935.

Trop, J.M., Kissock, K., Donaghy, E., Coleman, B., and Ridgway, K.D., 2012. Sedimentary record of exhumation along a forearc basin–accretionary prism boundary during ridge subduction: Paleogene Chickaloon Formation, northern Chugach Mountains, southern Alaska. Geological Society of America abstracts with programs, v. 44, no. 7, p. 175.

van der Heyden P., 1992, A Middle Jurassic to Early Tertiary Andean-Sierran arc model for the Coast Mountain belt of British Columbia: Tectonics, v. 11, p. 82–97.

Warr, L. N., and S. Cox, 2001, Clay mineral transformations and weakening mechanisms along the Alpine Fault, New Zealand, in The Nature and Tectonic Significance of Fault Zone Weakening, Special Publication, vol. 186, edited by R. E. Holdsworth et al., pp. 85–101, Geological Society of London, London.

Wenk, H., Kanitpanyacharoen, W., and Voltolini, M., 2010, Preferred orientation of phyllosilicates: comparison of fault gouge, shale and schist, Journal of Structural Geology, 32, pp. 478-489.

White, T.S., 2006. Stratigraphic and geochronological evidence for a time-transgressive unconformity and subsequent basalt extrusion event associated with ridge subduction, Paleogene Alaska. Geological Society of America abstracts with programs, Specialty Meeting no. 2, p. 92.

Wilson, F.H., Hults, C.P., Mull, C.G., and Karl, S.M., comps. 2015. Geologic map of Alaska. U.S. Geological Survey Scientific Investigations Map 3340, 197 p., 2 sheets, scale 1:584,000.

Winkler, G.R., 1992, Geologic map and summary geochronology of the Anchorage 1° x 3° quadrangle, southern Alaska: U.S. Geological Survey Map I-2283, 1 sheet, scale 1:250,000.

Winkler, G.R., Silberman, M.L., Grantz, A., Miller, R.J., and Mackevett, E.M., Jr., 1981. Geologic map and summary geochronology of the Valdez quadrangle, southern Alaska: U.S. Geological Survey Open-File Report 80-892A, 2 sheets, scale 1:250,000.